Microfluidic assays for assessing oligonucleotide catalyst abundance and monitoring biomolecule concentration in real time

A DISSERTATION

SUBMITTED TO THE FACULTY OF THE

UNIVERSITY OF MINNESOTA

BY

Cecilia Christine Douma

IN PARTIAL FULFILMENT OF THE REQUIREMENTS

FOR THE DEGREE OF

DOCTOR OF PHILOSOPHY

Michael T. Bowser, Advisor

October 2023

Acknowledgements

Science is a long and collaborative process, and I'm grateful for all of the people who have made my journey possible. To the scientists who have mentored and inspired me at Mark Twain, Memorial, Roosevelt, Luther College, the University of South Dakota, and IDT, thank you for showing me puzzles worth solving and questions worth answering.

I was supported by the Bowser Group at every stage of my graduate career. Sarah Nelson and Sean Dembowski gave me many of my first tutorials in the lab and helped me get my footing. Ryan Hunt and Nic Brinza provided steady advice, including feedback on writing and presentations going back to my first years. Matt LeMon taught me micro free-flow electrophoresis and laid the groundwork for μFFE in COC devices. Gretchen Burke has been with me from my first day to my last day, working in parallel with me on both droplets and μFFE. She's my go-to lunch buddy and sanity checker.

I'm especially grateful to my advisor, Mike Bowser. From the start, his pragmatic optimism has balanced my skepticism, encouraging me to think bigger and tackle harder questions. Thank you for your patience and excitement, and for introducing me to my favorite scientific challenges to date.

I found a good home in the University of Minnesota Department of Chemistry, and I'm grateful for the faculty, staff, and students who made my experience a positive one. In particular, I'm thankful for my community of grad students, especially my lunch bunch (Gretchen, Ellen, Eliza, and Tana) for their support and advice. Thank you for doing grad school with me.

There are many other individuals and facilities at the University of Minnesota that made my work possible. Thank you to the Minnesota Nano Center for the training, support, and equipment that allowed me to fabricate PDMS molds and profile μFFE devices. Thank you to the Earl E. Bakken Medical Device Center for fabricating μFFE master molds. Thank you to members of Prof. David Wood's lab for fabrication expertise and equipment access.

I'm thankful for all the people in my life who have supported my ambitions, past and present. I also could not have held it together for the last five years without a fantastic network of friends. We've enjoyed hikes, trips, meals, Zoom hangouts, long phone calls, and puppy cuddles. Thank you for sharing them all with me. Specific thanks to Ellen: It's unusual to find a roommate with compatible living habits, a shared taste in Netflix shows, *and* extensive chemistry expertise, but I hit the jackpot. Thank you for debriefing daily about all things good, bad, and just plain weird.

Finally, my deepest gratitude goes to my family, who not only support me but also "get me" on just about every level. To my entire family, but especially Mom, Dad, and Elliot, thank you for fostering my independence, sharing my passions (no matter how technical or trivial), and always making me feel loved.

Abstract

Microfluidic platforms control and manipulate very small volumes of liquid, typically at the microliter or nanoliter scale. By replacing pipettes and flasks with microfluidic channels and chambers, routine laboratory processes can be scaled down and sped up. Microfluidic platforms can mix, react, incubate, separate, extract, and detect solutions with high throughput and reproducibility, measuring the natural world at physical scales and timescales that would be inaccessible using traditional laboratory techniques.

This thesis describes the development of microfluidic assays to address two bioanalytical challenges. First, a droplet microfluidic platform was developed to quantify the abundance of catalytic molecules in pools of random-sequence DNA. Although catalytic oligonucleotides are attractive as sensors and therapeutic agents, the full scope of their catalytic activity is largely unknown. The microfluidic platform described here encapsulates a library of DNA sequences in droplets with a fluorogenic substrate. Droplets that contain a catalytic sequence will become fluorescent after a period of incubation, while droplets without a catalyst will remain dark. The frequency of catalysts in the original library can be calculated from the ratio of fluorescent and non-fluorescent droplets. This thesis describes the technical design of a droplet microfluidic platform, its performance in library screening experiments, and its application for the detection of a known DNA catalyst. A versatile microfluidic platform for oligonucleotide library screening could assess catalyst abundance across a wide variety of reactions and conditions, creating a new framework for understanding the catalytic potential of oligonucleotides.

Second, an aptamer affinity assay was developed for continuous cytokine quantification using micro free-flow electrophoresis (μFFE). Affinity assays are a prominent tool for biomolecule quantification because of their excellent sensitivity and specificity. However, traditional affinity assays use discrete samples and are poorly suited for measuring dynamic changes in an analyte's concentration. The ultimate aim of the aptamer assay is to continuously quantify cellular cytokine secretion in real time using μFFE, a continuous separation technique that can detect free aptamer and bound aptamer complexes in a flowing sample stream. This thesis describes the characterization of μFFE devices fabricated in cyclic olefin copolymer as well as initial development of a μFFE aptamer assay for continuous quantification of tumor necrosis factor α (TNFα).

Table of Contents

List of Tables

List of Figures

List of Abbreviations

µFFE	Micro free-flow electrophoresis
3D	Three-dimensional
90N	DNA oligonucleotide, length 90, with a fully randomized sequence
ABS	Acrylonitrile butadiene styrene
ACN	Acetonitrile
AFM	Atomic force microscopy
ANA	arabino nucleic acid
BSA	Bovine serum albumin
CE	Capillary electrophoresis
CeNA	Cyclohexene nucleic acid
COC	Cyclic olefin copolymer
COP	Cycloolefin polymer
ddPCR	Droplet digital PCR
DMSO	Dimethyl sulfoxide
DNA	Deoxyribonucleid acid
DNAzyme	DNA catalyst
ELISA	Enzyme-linked immunosorbent assay
EOF	Electroosmotic flow
FACS	Fluorescence-activated cell sorting
FADS	Fluorescence-activated droplet sorting
FAM	Fluorescein amidite
FANA	29-Fluoroarabino nucleic acid
FDG	Fluorescein di-β-D-galactopyranoside
FFE	Free-flow electrophoresis
FMG	Fluorescein mono-β-D-galactopyranoside
FRET	Fluorescence resonance energy transfer
HDV	Hepatitis delta virus
HEPES	N-2-hydroxyethylpiperazine-N'-2-ethanesulfonic acid
HIV	Human immunodeficiency virus
HNA	Hexitol nucleic acid
HPLC	High-performance liquid chromatography
I.D.	Inner diameter
k_{cat}	Turnover number

LC	Liquid chromatography
LIF	Laser-induced fluorescence
LOD	Limit of detection
LPS	Lipopolysaccharide
mRNA	Messenger RNA
N_{40}	40-nucleotide, random sequence DNA
nLC	Nano liquid chromatography
NMR	Nuclear magnetic resonance
O.D.	Outer diameter
PAGE	Polyacrylamide gel electrophoresis
PBS	Phosphate-buffered saline
PCR	Polymerase chain reaction
PDMS	Polydimethylsiloaxne
PEEK	Polyether ether ketone
PEG	Polyethylene glycol
PEO	Polyethylene oxide
PFPE	Perfluoropolyether
PMMA	Poly(methyl methacrylate)
PMT	Photomultiplier tube
PS	Polystyrene
PTFE	Polytetrafluoroethylene
RNA	Ribonucleic acid
rRNA	Ribosomal RNA
scRNA-seq	Single-cell RNA sequencing
SELEX	Systematic evolution of ligands by exponential enrichment
TFA	Trifluoroacetic acid
TNA	Threose nucleic acid
TNFα	Tumor necrosis factor α
tRNA	Transfer RNA
UV	Ultraviolet
UV-vis	Ultraviolet-visible spectroscopy
VS	Varkud satellite
XNA	Xeno nucleic acid

Chapter 1: Introduction

1.1 Overview

DNA and RNA oligonucleotides have numerous functions beyond encoding genetic information. Single-stranded molecules can fold into three-dimensional shapes that bind specific biological targets and may even catalyze their transformation. Like protein antibodies and enzymes, these nucleic acid tools are extremely valuable in diagnostics, biosensing, and detection. This thesis describes the development of custom microfluidic platforms for the study and application of nucleic acid technologies.

Chapters 2 and 3 explore the abundance of catalytic oligonucleotides. RNA, DNA, and XNA (xeno nucleic acid) oligonucleotides have been selected through laboratory evolution to catalyze a variety of biochemical reactions.[1,2] These nucleic acid catalysts are an attractive tool for biosensing[3] and therapeutics.[4] RNA catalysts have also been implicated in the origins of life.[5] However, the full scope of nucleic acid catalysis, including their abundance among all possible sequences, is currently unknown. To address these unknowns, a droplet microfluidic platform was developed for single-molecule DNA catalyst detection. The aim of the platform is to quantify the abundance of DNA catalysts by partitioning a library of random-sequence oligonucleotides into droplets with a fluorogenic substrate. After incubation, droplets that contain a catalyst will be fluorescent, and droplets without a catalyst will be non-fluorescent. Catalyst frequency can therefore be determined by counting fluorescent droplets.

Chapters 4 and 5 of this thesis describe progress toward a continuous, aptamer-based affinity assay. Existing affinity assays are a sensitive and widely-used tool for protein quantification. However, they use discrete samples and can only measure a single

concentration at a time. Significant technical improvements are needed to create affinity assays that continuously measure changes in a dynamic sample. Micro free-flow electrophoresis (μFFE) is a continuous separation technique that can be used to monitor changes in a dynamic sample. By combining the high specificity of affinity reagents with the continuous separation and detection of μFFE, we aim to build a versatile and unique platform for temporal monitoring of protein abundance.

1.2 Catalytic Nucleic Acids

1.2.1 Ribozymes: RNA Catalysts in Nature

Until the early 1980s, it was generally assumed that proteins and nucleic acids had distinct and mutually exclusive roles. Proteins were responsible for catalyzing biological reactions, while nucleic acids were responsible for carrying and transmitting genetic information. That assumption was disrupted by the discovery of nucleic acid catalysts. In 1982, two independent groups reported examples of naturally-occurring RNA molecules that could catalyze reactions without any protein involvement.[6,7] These RNA sequences, initially identified in bacteria, cleave and splice their own sugar-phosphate backbones to produce biologically active RNA molecules from longer precursor sequences.[6–11] These RNA catalysts were termed “ribozymes”, and a number of other examples were identified in nature, including hammerhead,[12] hairpin,[13] hepatitis delta virus (HDV),[14] Varkud satellite (VS),[15] and twister[16] ribozymes.

Ribozymes catalyze nucleolytic reactions with high efficiency and site specificity. Although the first known ribozymes (group I introns[8] and ribonuclease P[9–11]) were 200 to 500 nucleotides long, many self-cleaving ribozymes are much shorter. For example,

hammerhead ribozymes are around 40 nucleotides long, and HDV ribozymes are around 90 nucleotides long.[17] These lengths are pertinent to the selection of new RNA and DNA catalysts because they are practical for high-quality oligonucleotide synthesis.

1.2.2 The RNA World Hypothesis

Naturally-occurring examples of protein-free RNA catalysts spurred interest in the "RNA world hypothesis" about the biochemical organization of early life. The hypothesis proposes that RNA catalysts predate the protein catalysts found in nature today.[5] Unlike double-stranded DNA or proteins, RNA is uniquely suited to act as a self-replicating catalyst. It both catalyzes essential biological reactions and carries the genetic information required for persistence over time.[18,19] Modern life, with its complex network of DNA, RNA, and protein functionalities, could have originated from a much simpler RNA world where nucleic acids not only carried genetic information but also catalyzed their own splicing and propagation.

To sustain life in an RNA world, ribozymes would need to perform a set of basic metabolic reactions at rates fast enough to grow – not merely replace – their population. Many reactions necessary for RNA replication do not exist in the modern repertoire of naturally-occurring ribozymes, perhaps because ancestral ribozymes disappeared as high-efficiency protein ligases and polymerases evolved.[18] To strengthen the argument for an RNA world, researchers have designed *in vitro* selection protocols that isolate new ribozymes from pools of random RNA sequences. Laboratory evolution exerts selective pressures that favor the amplification of certain library members, in this case catalytically active ones, over the general population (see section 1.2.3). Selection experiments have

yielded RNA molecules that catalyze reactions including RNA polymerization,[20,21] RNA ligation,[22,23] phosphorylation,[24] acyl transfer,[25] aldol reactions,[26] and Michael addition[27]. These evolved functions have been presented as support for the RNA world hypothesis.

Criticisms of the RNA world hypothesis often emphasize the scarcity of *in vitro* selected ribozymes relative to the immense sequence space of random RNA libraries. Critics argue that efficient ribozymes could not have arisen by chance from the short, low-diversity RNA molecules likely present in a prebiotic world.[28,29] Other opinions on the origins of life propose that RNA catalysts evolved alongside prebiotic peptides[19] or that catalytic proteins predate catalytic nucleic acids[30]. The viability of the RNA world hypothesis ultimately hinges on the efficiency of early RNA catalysts and abundance of catalytic molecules among randomly-assembled RNA sequences, two unknowns that have yet to be addressed quantitatively.

1.2.3 DNA Catalysts: *In Vitro* Selection

The success of *in vitro* selection for RNA catalysts (or "ribozymes") motivated a wave of interest in DNA catalysts ("deoxyribozymes" or "DNAzymes"). Unlike ribozymes, DNAzymes do not occur in nature. While RNA is often found in small, single-stranded units, DNA is found almost exclusively in long, double-stranded helices, which would restrict any catalytic activity. However, DNA contains nearly the same functional units as RNA. Like RNA, single-stranded DNA is capable of folding into complex three-dimensional structures and binding with high specificity to a variety of targets.[31] It follows that synthetic, single-stranded DNA should also be capable of catalysis.[2]

The first DNAzyme, a Pb^{2+}-dependent RNA phosphoesterase, was isolated in 1994.[32] Breaker and Joyce selected catalytic sequences from random sequences by immobilizing biotinylated DNA libraries on a streptavidin matrix (Figure 1.1). Sequences that catalyzed their own self-cleavage were washed off the matrix, collected, and amplified by polymerase chain reaction (PCR) for subsequent rounds of selection. The selected catalytic sequence cleaved its substrate, a single-stranded DNA molecule with a single ribonucleotide, at rates as high as 1 min^{-1}. Similar selection protocols have isolated slower DNA catalysts for RNA cleavage in the presence of magnesium and calcium.[33] These DNAzymes are attractive topics of study and development because they can be engineered to cleave RNA substrates with high sequence specificity.[34]

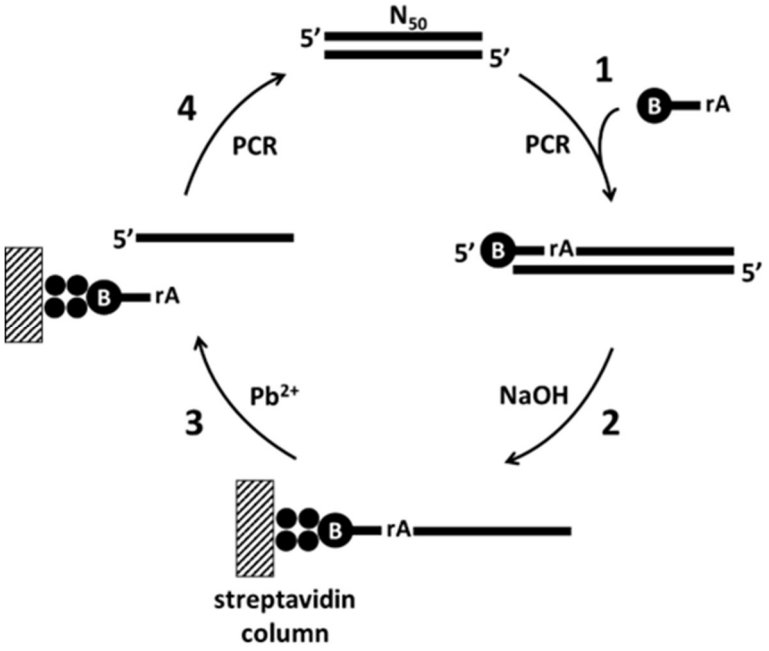

Figure 1.1*: Selection process for the first published example of a DNA catalyst, a Pb^{2+}-dependent RNA phosphoesterase. 1) A library of 50-nucleotide randomized sequences was amplified by PCR with a biotinylated primer terminated by a single RNA base. 2) The library was immobilized, and the un-biotinylated strand was removed by a NaOH wash. 3) Self-cleaving sequences were released from the matrix. 4) Cleaved sequences were PCR amplified for subsequent rounds of selection. Adapted from Breaker and Joyce.*[32]

DNA catalysts can also cleave DNA substrates. Early selections with immobilized libraries yielded several self-cleaving DNAzymes.[35,36] These DNAzymes perform oxidative reactions with high off-target cleavage.[37] The Silverman group was the first to describe a hydrolytic DNA-cleaving DNAzyme.[38] Their selection process, which was intended to produce a DNA catalyst for peptide bond hydrolysis, began with a hairpin-shaped oligonucleotide with a 40-nucleotide randomized region (N_{40}) on one arm and a tripeptide on the other (Figure 1.2). The cleavage products, each containing a catalytic sequence within the N_{40} region, were separated from un-cleaved molecules by polyacrylamide gel electrophoresis (PAGE), amplified by PCR, and subjected to subsequent rounds of selection.

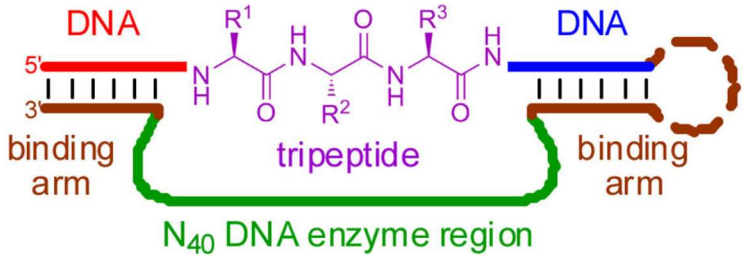

***Figure 1.2**: Design of a hairpin substrate for DNA catalyst selection. Binding arms position an N_{40} randomized region near an embedded tripeptide. A hairpin loop connects the substrate arm to the catalyst arm so that cleavage products (isolated by PAGE) contain the catalytic sequence. Adapted from Chandra, Sachdeva, and Silverman, Nature Chemical Biology, 5(10).[38] Reproduced with permission from Springer Nature. Copyright 2009.*

The Silverman group used similar hairpin libraries in combination with chemical capture techniques to impose selection specificity for more challenging reactions. For example, Figure 1.3 shows a capture oligonucleotide modified with an amine group that specifically binds the desired carboxyl product of ester/amide bond hydrolysis. It will not react with potential side products of off-target cleavage events such as general phosphoester hydrolysis.[39] Attachment of the capture oligonucleotide decreases the

mobility of the correct cleavage product during PAGE, so the resulting gel will have distinct bands for the intact substrate, the shorter non-specific cleavage product, and the longer specific cleavage product. This selection scheme yielded DNA catalysts for ester and aromatic amide hydrolysis.[39] Similar selection schemes have successfully isolated DNA catalysts for aliphatic amide hydrolysis,[40] tyrosine and serine dephosphorylation,[41] and formation of dehydroalanine from phosphoserine[42].

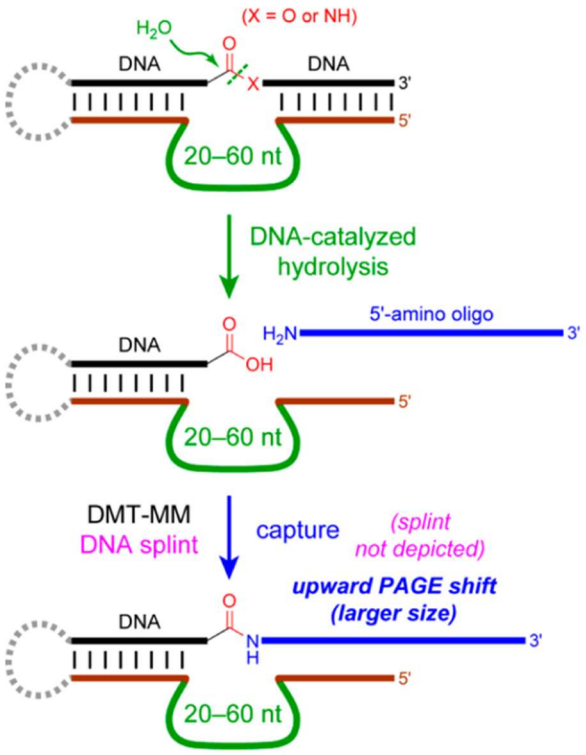

Figure 1.3*: Selection process for an ester- or aromatic amide-cleaving DNA catalyst. Self-cleaving hairpin molecules are captured by chemical conjugation to an amino-modified oligonucleotide. The resulting PAGE shift differentiates the desired product from both the intact substrate and off-site cleavage products. Reprinted with permission from Brandsen et al., Journal of the American Chemical Society, 135(43). Copyright 2013 American Chemical Society.*[39]

DNAzymes have also been selected to catalyze various types of bond formation. One bond-forming reaction of particular interest is RNA or DNA ligation. The first DNAzyme isolated for DNA ligation was selected using a biotinylated DNA substrate.[43]

Molecules that successfully catalyzed their own ligation to the substrate were isolated by immobilization on a streptavidin affinity column. Alternative ligase selection strategies use PAGE to separate self-ligating molecules from non-catalytic molecules. These protocols have produced catalysts for 3'-5' DNA linkages,[44] 3'-5' RNA linkages,[45] and 2'-5' RNA linkages[46]. Other bond-forming reactions of interest involve protein modification. DNAzymes have been selected to attach nucleotide chains to the hydroxyl groups of tyrosine[47,48] and serine[49] residues. Protein-modifying DNAzymes have also been selected to phosphorylate tyrosine,[50] adenylate tyrosine,[51] and conjugate oligonucleotides to lysine through a reactive phosphorimidazolide group[52].

Altogether, *in vitro* selection has produced an impressive catalog of DNA catalysts. Selection protocols typically begin with a library of 10^{13}-10^{16} unique sequences (typically 20-60 nucleotides long) and are able to isolate one or more sequences that demonstrate catalytic activity in subsequent intermolecular assays.[1] However, nearly all existing protocols rely on selection of intramolecular catalysts. Library molecules contain both a randomized region and a substrate moiety so that the product of a successful reaction is tagged with the catalytic sequence that acted on it. This enables separation of catalytic sequences from non-catalytic sequences, but it also imposes steric requirements and limits catalysts to a single turnover during selection. A drawback of intramolecular selection is that the structural diversity of catalysts is limited, and it is challenging to select for faster catalysts. The fastest *in vitro* selected DNAzymes perform around 2 reactions per minute, and other DNAzymes are much slower.[53] Intermolecular selection reactions could identify

new structural classes of nucleic acid catalysts, potentially expanding their scope and effectiveness.

1.2.4 XNA Catalysts

Catalysts have also been selected from libraries of synthetic genetic polymers. These molecules, sometimes collectively referred to as xeno nucleic acids or XNAs, have modified bases or chemical backbones that do not occur in nature. XNA catalysts are of particular interest in therapeutic fields. Not only do they expand the chemical space of potential catalysts, but many chemical modifications make nucleic acids more resistant to nuclease activity and therefore more compatible with *in vivo* use. The evolution of XNA catalysts also poses interesting questions about the origins of life: What if modern genetic polymers (RNA and DNA) were preceded by other genetic materials?[54] Are there catalytic XNA polymers that never evolved into terrestrial life?

The first XNA catalysts were RNA-cleaving sequences selected from pools of arabino nucleic acids (ANA), 29-fluoroarabino nucleic acids (FANA), hexitol nucleic acids (HNA), and cyclohexene nucleic acids (CeNA).[55] Subsequently, additional FANA[56,57] and threose nucleic acid (TNA)[58] catalysts were identified. At least one FANA catalyst exceeded the kinetic performance of the well-studied 10-23 DNAzyme.[59] Because the PCR amplification required for *in vitro* selection is challenging or impossible for some XNA polymers, some XNA catalysts have been rationally designed. Instead of starting with an XNA library, researchers have strategically added synthetic groups to existing RNA or DNA catalysts to decrease their cofactor dependence and improve their stability for therapeutic applications.[60]

1.2.5 Applications of catalytic oligonucleotides

Oligonucleotides can catalyze a wide range of reactions, and their inexpensive synthesis makes them ideal catalysts for a wide range of applications. Currently, the most significant applications of catalytic oligonucleotides are in the fields of gene silencing and biosensing. DNA and XNA catalysts readily act on nucleic acid substrates and are therefore appealing candidates for therapeutic applications targeting messenger RNA (mRNA) transcripts. Gene silencing, a therapeutic approach that suppresses the expression of one or more genes, was among the first proposed applications of RNA-cleaving DNAzymes.[34] The active motif of a previously-selected DNAzyme can be incorporated between custom binding arms to target specific mRNA transcripts for cleavage, thereby reducing translation of the protein of interest. Gene-silencing DNAzymes have successfully targeted mRNA transcripts involved in wound repair,[61,62] tumor growth,[63,64] and asthmatic response[65]. Other DNAzymes target transcripts from pathogenic viruses and bacteria.[66–68]

DNAzymes also have extensive potential in biosensing applications. One class of RNA-cleaving DNAzyme assays uses a fluorogenic oligonucleotide substrate in combination with a metal- or macromolecule-dependent DNAzyme (Figure 1.4).[2] The substrate is only cleaved (and signal is only produced) when the target cofactor is present. DNAzymes selected for metal ions including cadmium,[69] uranyl,[70] lead,[71] and mercury[72] have been incorporated into high-sensitivity, fluorescence-based detection assays. Some selection protocols for pathogen-specific DNAzymes expose a DNA library to the crude extracellular matrix of a bacterial pathogen of interest without identifying or purifying a

specific target. This method has produced DNAzymes for the detection of *E. coli*[73] and *C. difficile.*[74]

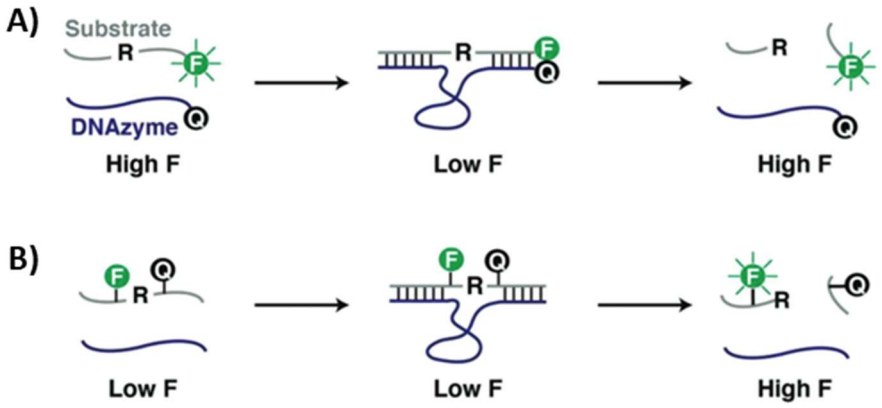

Figure 1.4*: Two DNAzyme-based FRET detection methods for biosensing applications. Fluorescence increases when the fluorophore (F) is spatially freed from a quencher (Q). Although the fluorophore is typically incorporated on the substrate strand, the quencher may be incorporated either on the substrate (A) or catalyst (B) strand. Adapted from Morrison, Rothenbroker, and Li, Small Methods, 2(3).*[3] *Reprinted with permission from John Wiley & Sons, copyright 2018.*

Increasingly, there is interest in potential applications of DNAzymes in chemical and biochemical synthesis. For example, a DNAzyme was selected to catalyze the challenging final cyclization of a short peptide through a thioester bond.[42] Other DNAzymes catalyze carbon-carbon bond formation through Michael addition,[27] aldol reactions,[26] Diels-Alder cycloaddition,[75] or Friedel Crafts alkylation[76]. The expanding repertoire of DNA catalysis presents opportunities to simplify the synthesis, modification, and conjugation of macromolecules.

1.2.6 Limitations of in vitro selected nucleic acid catalysts

An often-cited limitation of nucleic acid catalysts compared to protein enzymes is their catalytic efficiency. Some argue that DNAzymes are too slow to be considered plausible alternatives to the enzymes used in most protein-based methods.[1] A meta-analysis

of kinetic constants found in major enzyme data repositories revealed that the median rate constant for naturally-occurring protein enzymes is k_{cat} = 13.7 reactions per second, and many enzymes used in common biochemical assays are orders of magnitude faster.[77] This serves as a general reference point for contextualizing the reported rates of ribozymes and DNAzymes. Naturally-occurring hammerhead and twister ribozymes are among the fastest known nucleic acid catalysts, with rate constants of up to 14.5 sec^{-1} and 16.7 sec^{-1}, respectively, under optimal conditions.[12,16] Meanwhile, the RNA-hydrolyzing 10-23 and 8-17 DNAzymes, two *in vitro* selected catalysts often used in detection assays, work at rates of roughly 0.06 sec^{-1} under optimal conditions.[34,78]

Nucleic acid catalysts, like their protein counterparts, have diverse structures and mechanisms. Their catalytic activity depends strongly on the conditions of the reaction, and optimal conditions vary depending on the mechanism of the catalyst. For example, a detailed kinetic characterization of the well-characterized, RNA-cleaving 8-17 DNAzyme demonstrated the dependence of the catalyst's cleavage rate on salt concentration, pH, and temperature.[78] When *in vitro* selected DNAzymes are characterized, their dominant mechanistic trends and collective preferences in reaction conditions have been shaped by the conditions imposed during selection.

A comprehensive analysis by Breaker *et al.* that examined kinetic characteristics of 14 classes of RNA-cleaving RNA and DNA catalysts underscores the consequences the of selection environment on the rates and mechanisms of engineered nucleic acid catalysts.[53] Although a number possible catalytic strategies exist for the reaction, half of the catalysts studied used the same combination of two catalytic strategies (in-line nucleophilic attack

and 2'-hydroxyl deprotonation). These catalysts all approach a rate constant of approximately 2 reactions per minute, which is consistent with the theoretical maximum rate enhancement for the combined mechanisms.[79–81] However, this "speed limit" was not universal among RNA-cleaving catalysts. Natural ribozymes and a handful of engineered RNA and DNA catalysts exceeded 2 reactions per minute by employing different combinations of catalytic strategies.[53] This suggests that it may be possible to isolate faster catalysts by changing or expanding the reaction conditions under which catalysts are selected.

1.3 Droplet Microfluidics

Emulsions are useful tools for low-volume experiments where nanoliter, picoliter, or femtoliter droplets serve as reactors that isolate reagents and compartmentalize products.[82,83] Early emulsion generators produced an array of droplets by spraying a fine mist of water into mineral oil. This technique was used to isolate single microbes,[84] cells,[85] and enzyme molecules.[86] Although these experiments contributed many novel insights, they were limited by their low throughput and non-uniform droplet volumes. Modern droplet emulsions use microfluidic channels and segmented flows of immiscible liquids to generate small, isolated reactors with extremely uniform volumes.[87–89] Advances in the design, fabrication, and operation of droplet microfluidic platforms have enabled a wide range of bioanalytical applications that generate, manipulate, and detect droplets with increasing sophistication.

1.3.1 Droplet generation, stability, and handing

When streams of immiscible liquids (like water and oil) meet at a single junction, they proceed in alternating, single-phase plugs (Figure 1.5).[88,89] In a hydrophobic channel, such as a Teflon capillary or an Aquapel-treated PDMS device, the oil preferentially wets the channel surface. The aqueous phase forms discrete droplets in the oil to minimize channel-water contact and oil-water surface area, and the oil phase carries these droplets through the channel.[90]

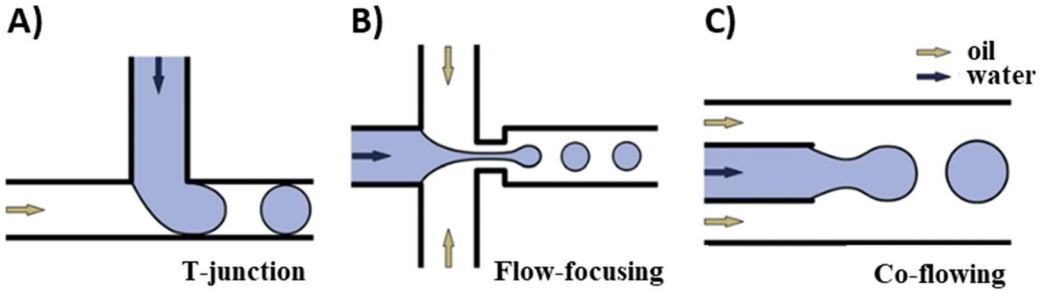

Figure 1.5*: T-junction (A), flow-focusing (B), and co-flowing (C) geometries for the generation of aqueous droplets in oil. Adapted from Collins et al.*[94] *Used with permission of the Royal Society of Chemistry, from Lab on a Chip, 15(17), copyright 2015; permission conveyed through Copyright Clearance Center, Inc.*

The incoming aqueous and oil phases can meet at a variety of intersection geometries. A T-intersection with two incoming channels and one outlet channel generates droplets due to the competing influences of surface tension and shear force (Figure 1.5A).[91] An alternative flow-focusing geometry typically includes a single incoming aqueous channel intersected by perpendicular streams of incoming oil (Figure 1.5B). The oil-encompassed aqueous stream is pushed through a narrow opening, exerting stream-narrowing pressure that breaks the aqueous phase into discrete droplets as it exits the oriface.[92] Somewhat similarly, a co-flowing device in which the aqueous stream is surrounded by the incoming oil phase can be constructed by nesting an aqueous phase-

flowing capillary inside a larger oil-flowing capillary (Figure 1.5C).[93] All three methods are capable of generating highly uniform droplets. Droplet volume can range from femtoliters to microliters, depending on the flow rates of the two phases and the diameter of the generation channel.[90]

1.3.2 Oil phases

Long-term droplet stability is controlled by the oil-surfactant system chosen for the continuous phase. Perfluorocarbons are effective agents for water-in-oil emulsions because they are exceptionally hydrophobic.[95] The limited solubility of fluorophores and other small, organic molecules in perfluorocarbon oils also reduces cross-talk between droplets.[96] Surfactants are added to the oil to stabilize the water-oil interface. An effective surfactant has a polar "head" and a nonpolar "tail" and is readily adsorbed at the oil-water interface, reducing interfacial tension.[97]

HFE-7500 (Novec 7500, 3M, Maplewood, MN) and FC-40 (Fluorinert 40, 3M) are among the most popular fluorinated oils for droplet applications. Surfactants span a wide range of chemical characteristics, including ionic (e.g., poly(hexafluoropropylene oxide) with terminal carboxylate, sold as Krytox 157 FSH from Miller-Stephenson), nonionic (e.g., PEG-$PFPE_2$, sold as EA surfactant from RAN Biotechnologies), and dendronized[98] polymers. Nanoparticles (e.g., Fluoro-phase from Dolomite) can also stabilize the water-oil interface.[99]Additionally, a number of proprietary surfactants and droplet oil blends have emerged with the rise of commercial platforms for droplet microfluidics. For example, Bio-Rad has optimized a proprietary fluorinated oil/surfactant system for use in its droplet digital PCR (ddPCR) system.[100]

1.3.3 Poisson statistics

Droplet microfluidic applications often encapsulate a single cell or single molecule so that it can be studied in isolation. However, it is important account for the possibility that multiple particles can be encapsulated in a single droplet. If particles are distributed randomly in the original solution, then it is possible that when the solution is partitioned into droplets, some droplets may contain multiple particles and others may contain none. The distribution of particles in droplets can be modeled using Poisson statistics, which describe the probability of an event (cell or molecule encapsulation) occurring in a fixed space (droplet volume). The Poisson model assumes that particles are encapsulated into droplets at a fixed rate and encapsulation events occur independently of each other. When these conditions are met, the probability distribution for finding a given number of particles in a droplet described as:

$$p(k, \lambda) = \frac{\lambda^k e^{-\lambda}}{k!} \tag{1.1}$$

where k is the number of particles in the droplet and λ is the average number of particles per droplet.[94] Figure 1.6 shows the Poisson distribution for λ values of 0.1, 0.5, 1, 2, and 3.

As the concentration of particles in the initial solution decreases, the probability that multiple particles will be encapsulated in a single droplet decreases. Meanwhile, there is an increasing probability that a droplet will contain no particles at all. Passive encapsulation methods for single cell and single molecule experiments control droplet volume and sample concentration ensure that most droplets will contain no more than one copy of particle of interest.

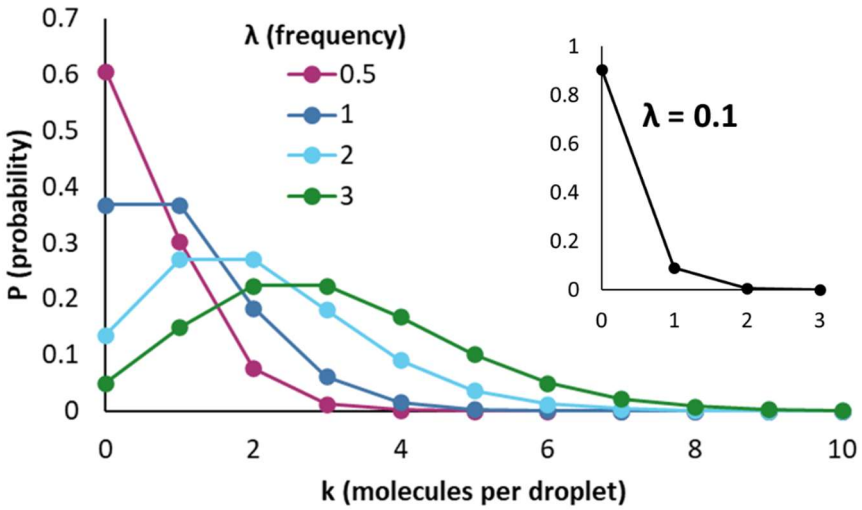

***Figure 1.6**: Poisson distributions describing the probability (P) of finding k molecules in a droplet given an average frequency (λ) of 0.5, 1, 2, or 3 molecules per droplet. At λ = 0.1 (inset), there is less than a 0.5% chance of a droplet containing more than one molecule.*

A disadvantage of passive encapsulation is that many droplets will be empty. To increase efficiency, active encapsulation can be used to improve the proportion of droplets that contain exactly one particle. Collins *et al.* have summarized methods of active encapsulation either by structuring the sample (so that particles aren't randomly distributed) or by sorting droplets (to remove droplets that contain no or multiple particles).[94]

1.3.4 Applications of droplet microfluidics

Droplet microfluidic platforms have been broadly adopted for bioengineering and bioanalysis. A few key applications are outlined below.

Droplet detection: Fluorescence-based methods are the most popular tool for droplet detection. Droplets can be detected on-chip with high sensitivity either by imaging a field of many droplets in a large chamber or by reading single droplets as they flow through a narrow channel.[82] Label-free optical methods, including bright field microscopy,

UV-vis absorbance, and Raman spectroscopy, have also been used for droplet detection.[101] In addition to optical detection, droplet microfluidic devices can be coupled with off-chip separation and detection, including nuclear magnetic resonance (NMR), capillary electrophoresis, liquid chromatography, and mass spectroscopy.[82,102,103] These techniques enable more much more detailed analysis and identification of droplet contents than fluorescent labels or optical methods alone.

Droplet sorting: An important extension of droplet microfluidics is fluorescence-activated droplet sorting (FADS). Similar in principle to fluorescence-activated cell sorting (FACS), FADS couples the fluorescence detection of flowing droplets with dielectrophoresis to direct droplets into collection channels based on their fluorescence intensity. Baret *et al.* developed a droplet sorting device that integrated droplet spacing, droplet detection, and droplet sorting (Figure 1.7).[104] Droplets were injected into the device and flowed single file through a channel, passing one-by-one through a laser-induced fluorescence (LIF) detector. Under rest conditions, droplets flowed through the detection channel and into the waste channel of the sorting fork. When a highly-fluorescent droplet was detected, an alternating current pulse was applied to electrodes embedded in the device, producing a temporary electric field that deflected the droplet into the collection channel.

FADS has been successfully applied in a variety of droplet-based detection applications. Baret's group used their device to assess enzymatic activity, encapsulating *E. coli* cells in droplets with a fluorogenic substrate.[104] Positive droplets contained cells expressing a substrate-cleaving β-galactosidase enzyme, while negative droplets contained

cells expressing an inactive version of the enzyme. Droplet sorting successfully separated the two populations. Similar FADS devices have been applied to directed evolution,[105,106] strain isolation,[107] single cell encapsulation,[108] environmental sample testing,[109] and antibody screening[110,111].

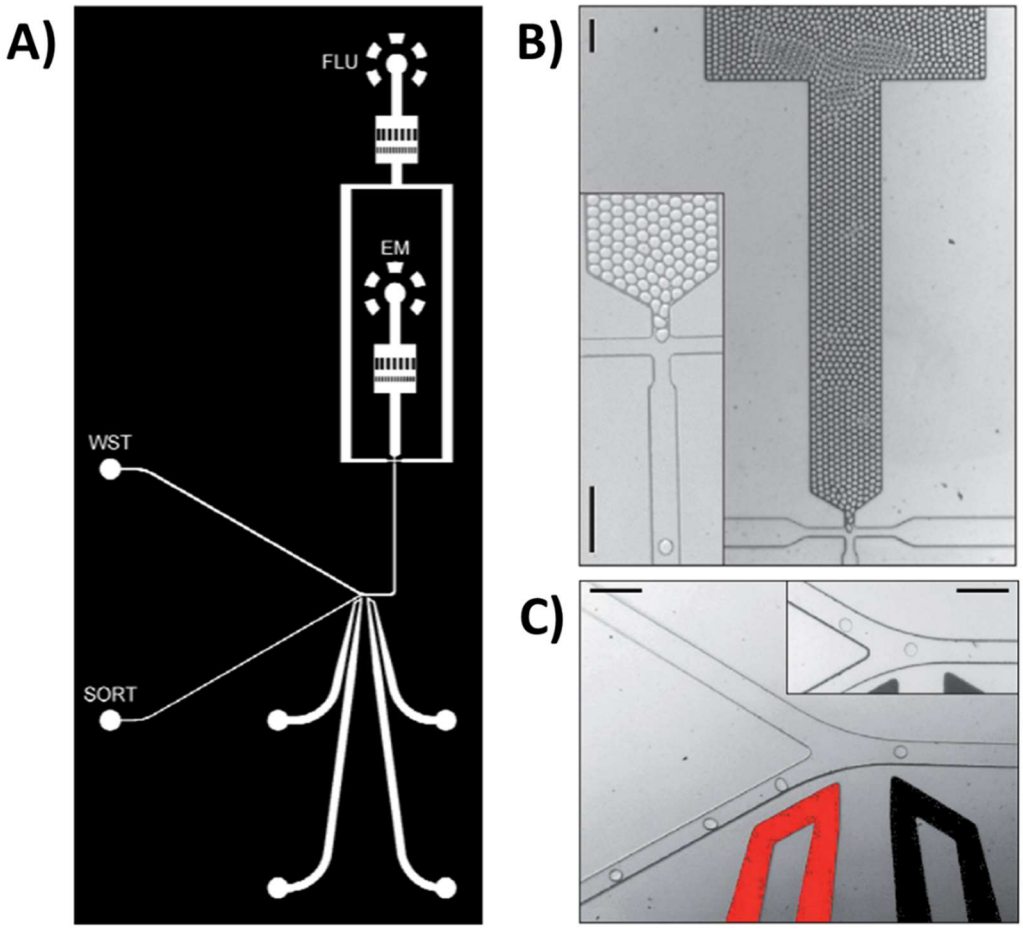

Figure 1.7*: A) Design of a FADS device. Droplets are injected at the EM inlet, and perfluorinated oil is injected at the FLU input. The two liquid inputs meet at a t-junction, shown in B), where droplets are spaced by oil. Positive and negative electrodes, shown in C) with positive electrode shaded red, are used to sort droplets into waste (WST) and collection (SORT) channels. Scale bars represent 100 µm. Adapted from Baret et al.*[104] *Used with permission of the Royal Society of Chemistry, from Lab on a Chip, 9(13), copyright 2009; permission conveyed through Copyright Clearance Center, Inc.*

Single cell encapsulation: Microfluidic droplets are a valuable tool for studying biological processes at the single-cell level. Single cell encapsulation is uniquely well-

suited for measuring cell-to-cell heterogeneity that would be overlooked by ensemble measurements. These experiments have measured the secretion of proteins, enzymes, antibodies, cytokines, and metabolites from individual cells.[112,113] Presently, a goal of single-cell droplet technology is to collect multimodal measurements that profile a combination of genomic, transcriptomic, proteomic, and metabolomic markers on a single platform.[112]

Single enzyme encapsulation: Single enzyme molecules can also be encapsulated in droplets for detailed analysis of enzymatic activity, mechanisms, and heterogeneity. Droplet microfluidic studies of single enzymes are described in more detail in section 1.4.2.

Gene expression, genotyping, and genomics: Droplet microfluidic platforms are widely used to analyze nucleic acids, and the technology has made significant impacts in the fields of gene expression, genotyping, diagnostics, and genomics. In droplet digital PCR (ddPCR), DNA or RNA templates are partitioned into droplets and amplified by PCR.[100] After amplification, a fluorogenic probe reports the presence or absence of amplified target as each droplet is individually detected, allowing absolute quantification of the number of target templates in the original sample. Compared to bulk PCR reactions, ddPCR is particularly well-suited for detecting low-abundance targets like biomarkers,[114] rare genetic variants,[115] low-expression targets,[116] and pathogenic viral or bacterial material.[117]

Single-cell encapsulation has also spurred a wave of droplet-based, high-throughput sequencing workflows. To date, the largest example of droplet sequencing is single-cell RNA sequencing (scRNA-seq) for transcriptome analysis.[113,118] Individual cells

are isolated in droplets, where their RNA transcripts are tagged with a unique DNA barcode sequence. After high-throughput sequencing, reads are sorted by barcode, associating all reads from a single cell. scRNA-seq reveals heterogeneity among cells. It has been used to study cellular diversity within a tissue or tumor, patterns of interaction between cells, mechanisms of disease, and cellular responses to drugs or stimulation.[118]

Quantification: Bulk methods for quantitative analysis measure the concentration of molecules per sampled volume. In contrast, the distribution of individual analyte molecules into droplets enables absolute quantification (Figure 1.8). This approach is sometimes referred to as "digital" analysis because analytes are quantified by counting the number of droplets that do and do not contain a particle of interest.[114,119]

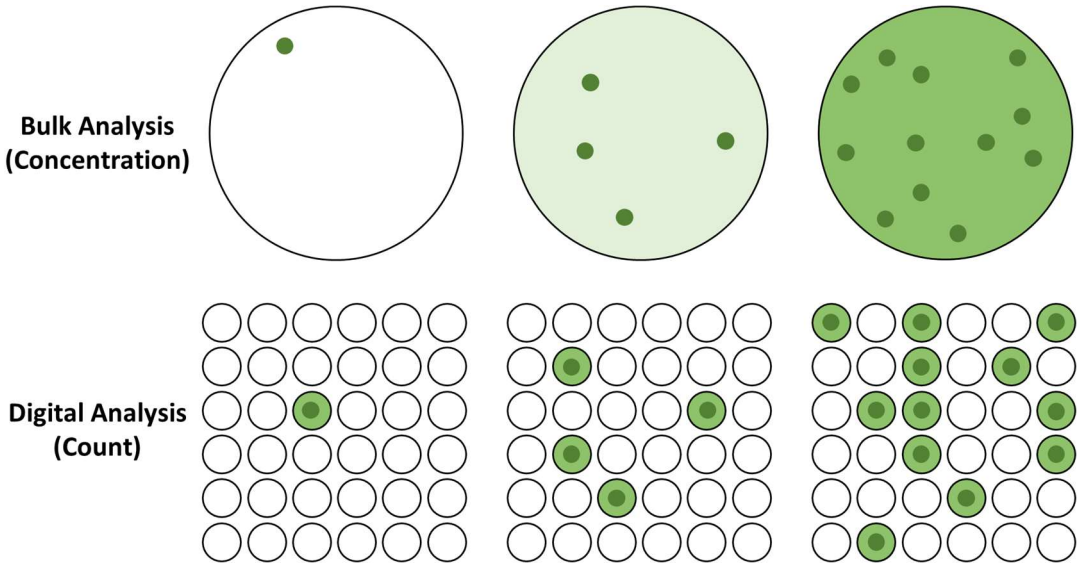

Figure 1.8*: Comparison of bulk and digital methods for analyte quantification.*

Digital analysis can quantify extremely dilute or low-abundance targets because analytes are partitioned into very small containers. Sample dilution increases the number of negative droplets, but it doesn't change the signal of positive droplets. Since individual analyte particles are counted directly, digital analysis does not require standardization with

a calibration curve. In addition to nucleic acid quantification by ddPCR, droplet digital methods have been used to quantify a variety of proteins and enzymes.[114]

Screening, selection and catalyst evolution: Advances in droplet manipulation and sorting techniques have allowed experiments to move from detection and quantification to high-throughput screening and catalyst selection.[120] A notable droplet screening application is in the field of protein engineering, where libraries of protein variants or single cells with gene or plasmid variants can be encapsulated, manipulated, and detected. Droplet platforms have been used to evolve high-activity variants of protein enzymes[121] and ribozymes.[122] In both of these droplet-based catalyst evolution approaches, droplets contained a single copy of a plasmid or gene that encoded for the catalysts, and many copies of the catalysts were transcribed or translated after encapsulation.

DNAzymes in droplets: In a few instances, DNAzymes have been used as probes or reporters in droplet microfluidic technologies. These platforms use DNAzymes for both analyte recognition and signal amplification. Droplets isolate individual pathogens and contain fluorescent products, enabling sensitive detection and quantification at the single-pathogen level. Droplet DNAzyme platforms have used self-cleaving fluorogenic probes,[123] DNAzyme-mediated rolling circle amplification,[124] and multi-oligonucleotide reporter complexes[125] for bacterial and viral detection.

1.4 Single Molecule Catalyst Detection

In biological, chemical, and industrial settings, catalysts usually operate in bulk reactions. However, it is sometimes valuable to study catalysts in a single molecule context. Monitoring a single molecule in isolation gives more nuanced information about the

catalyst's mechanism, kinetics, and activity than observations at the ensemble level, often revealing the heterogeneity of individual catalyst molecules.[126] There is also increasing interest in digital methods for analytical quantification, which focus on counting analyte molecules in isolation rather than measuring their concentration in bulk solution.[119]

There are a variety of techniques for studying catalysts at the single-molecule level, but all share some basic requirements. First, they must be able to isolate individual catalysts, either by partitioning, diluting, or immobilizing molecules. And second, they must incorporate a sensitive method for detecting activity. Microfluidic techniques are well-suited to meet both requirements and are increasingly popular for single molecule catalyst detection.

1.4.1 Approaches to single molecule enzymology

Most applications of single molecule biocatalyst detection involve naturally-occurring protein enzymes. Once isolated, enzymes are monitored to assess the speed, mechanism, and uniformity of their activity.[127] In an early example of single enzyme detection, Boris Rotman encapsulated individual β-D-galactosidase molecules with a fluorogenic substrate in a polydisperse water-in-oil emulsion.[86] The enzyme was introduced at low concentrations so that most droplets contained no more than one copy. As enzymes cleaved the substrate, the fluorescent product accumulated in the droplet. The molecular weight and turnover number of the enzyme were calculated using volume-normalized fluorescence measurements, and active enzyme molecules could be distinguished from thermally inactivated molecules. Molecular weight was calculated by counting the number of droplets with 0, 1, 2, or 3 copies of the enzyme. For a solution with

a known weight concentration, determination of the molar concentration (by droplet counting) reveals the molecular weight of the enzyme. Turnover number was calculated by measuring changes in the fluorescence intensity of individual droplets over time. Droplets with a single copy of β-D-galactosidase were identified based on their fluorescence early in the incubation. As the isolated enzymes cleaved the substrate, the product accumulated in the droplets, so the increase in fluorescence intensity over time revealed the number of reactions performed over time.

Many subsequent experiments have used fluorogenic substrates to amplify the signal produced by a single, confined enzyme molecule. In another example of single molecule isolation, low-concentration lactate dehydrogenase,[126] β-D-galactosidase,[128] and alkaline phosphatase[129] solutions were loaded into capillaries with their respective fluorogenic substrates. Enzyme molecules were distributed sparsely so that each produced a zone of product, which could be manipulated and detected by capillary electrophoresis.

In contrast, microarrays use physical barriers between enzyme molecules. Enzymes can be incubated in microfluidic wells with a fluorogenic or chromogenic substrate and then imaged. Nanoscopic etched silica vials,[130] etched fiber optic bundles,[131,132] cyclic olefin polymer devices,[133] and polydimethylsiloxane (PDMS) devices[134] have all been used to study single enzyme molecules.

Advances in spectroscopy and microscopy have also produced techniques sensitive enough to detect a single enzyme molecule acting on a single substrate molecule. monitoring reactions at the level of a single turnover.[135] Modern microscopy techniques are sensitive enough to detect the burst of fluorescence that appears immediately after

cleavage of a single fluorogenic substrate molecule.[136,137] Fluorescence resonance energy transfer (FRET) experiments can monitor conformational changes in a single enzyme molecule over the course of its catalytic cycle.[138,139]

A number of single-molecule detection approaches, including many single-molecule microscopy techniques, use an immobilized array of proteins, oligonucleotides, or small molecules on a solid surface. This simplifies detection by fixing molecules in place and satisfies the isolation requirement of single molecule detection. However, a disadvantage of immobilization-based techniques is that conjugation and attachment can change the conformation and activity of the molecule, so observations of immobilized molecules doesn't necessarily reflect their behavior in solution.[127]

1.4.2 Single molecule enzymology in droplets

Of particular relevance to this thesis are droplet microfluidic approaches to single molecule detection. Like Rotman's early study of β-D-galactosidase activity, these techniques generally encapsulate a single catalyst molecule in droplets with a fluorogenic substrate, then detect the signal of accumulated, fluorescent product. But unlike the polydisperse emulsions of those early experiments, modern droplet microfluidics can generate droplets with extremely uniform volumes, manipulate them with high throughput, and detect them with high sensitivity.

For example, Song and Ismagilov performed kinetic characterization of ribonuclease A in droplets on a PDMS chip.[87] The enzyme and substrate streams were mixed on-chip and detected at several points across an incubation channel for a rapid alternative to the multi-reaction, multi-timepoint experiments traditionally used to

characterize enzyme kinetics. Bui *et al.* used a similar platform to characterize the kinetics of β-galactosidase, this time with an on-chip concentration gradient to automate dilution.[140] Subsequent droplet microfluidic platforms decreased the enzyme concentration to the single-molecule regime for kinetic characterization and digital quantification of β-galactosidase[141] and β-glucosidase.[142] Compared to other single molecule enzymology approaches, these droplet microfluidic techniques are capable of increased throughput and automation.

1.4.3 Single molecule detection of nucleic acid catalysts

Although most single molecule detection techniques were originally developed for protein enzymes, similar approaches have been used to study nucleic acid catalysts. To date, most efforts focus on mechanistic characterization of *in vitro* selected DNA catalysts at the single-turnover level. FRET studies have revealed the conformational dynamics of the 10-23 DNAzyme,[143] 8-17 DNAzyme[144] and 39E DNAzyme[145] as they fold in the presence of ionic cofactors. Label-free methods have also been used to study nanostructure-bound DNAzymes at the single molecule level with either atomic force microscopy[146] or nanopore[147] detection. Unlike droplet and microarray techniques where protein enzymes were incubated with a fluorogenic substrate, these examples of single-molecule DNAzyme detection do not examine their activity in a multiple turnover context.

1.5 Affinity Assays

Affinity reagents like antibodies and aptamers are important tools in biomolecule detection and analysis. They bind to ligands with high affinity and selectivity and are often used as probes or recognition elements in high-sensitivity assays for proteins, peptides, and

other targets. These affinity assays are used for biomolecule detection in clinical, commercial, research, and analytical laboratories worldwide.[148] Although affinity assays are well established and broadly used, current efforts to improve the technology aim to increase their throughput, sensitivity, and reproducibility.[149,150] There is also interest in incorporating affinity reagents into more complex systems for rapid, multiplexed measurements of biological processes.[151]

1.5.1 ELISA

Enzyme-linked immunosorbent assays (ELISAs) are a ubiquitous tool for protein, peptide, hormone, and antibody quantification.[152–154] They use an antibody for high-specificity antigen recognition and an enzymatic signal amplification reaction for high-sensitivity detection. Reactions are typically performed in well plates, and the surface of the well is coated with either the antigen or the antibody. Because of this immobilization, antibody-bound reagents are tethered to the walls of the well, and unbound reagents can be washed away.

Figure 1.9 shows a simple example of a direct ELISA protocol where an antigen of interest has been immobilized in a well. An enzyme-conjugated antibody binds to the immobilized antigen, and unbound antibody is washed away. Then, a reporter substrate is added to the well. As the enzyme converts the substrate into product, it produces a signal that increase proportionately with the amount of antigen in the sample.

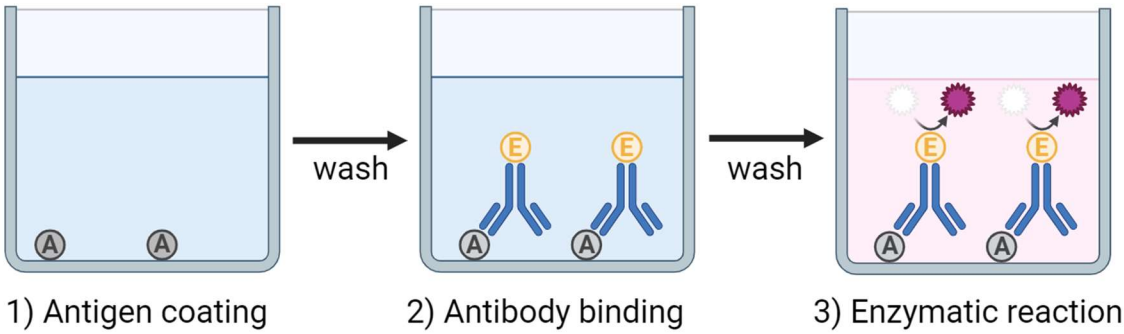

Figure 1.9*: Diagram of a direct ELISA protocol for protein detection. The well is coated with an antigen (A), which is bound by an enzyme (E)-conjugated antibody. Unbound antibody is removed by washing. Antigen concentration is determined through an enzymatic reaction that produces a colored product. Created with Biorender.com.*

Figure 1.10 shows the four main types of ELISA.[153,154] The direct ELISA (also shown in Figure 1.9) is the simplest, with antigen coating the well and a single, enzyme-conjugated antibody used for detection. It is often used to study the affinity and specificity of the antibody-antigen complex. Alternative ELISA approaches can decrease cost, increase sensitivity, and improve specificity. An indirect ELISA also begins with antigen immobilization on the well surface, but it uses two different antibodies. A primary detection antibody binds to the antigen, and an enzyme-conjugated secondary antibody binds to the primary antibody. Indirect ELISAs are popular for quantifying antibodies in biological samples.

Sandwich ELISAs are the most common option for quantifying targets in biological samples. They are performed in wells coated with a capture antibody that is specific to the antigen of interest. A second antigen-specific antibody also binds to the target molecule, forming an antigen sandwich between a pair of antibodies. The sandwich complex can be directly detected by attaching the enzyme to the second antigen-binding antibody. More often, it is indirectly detected by an enzyme-conjugated third antibody. Sandwich ELISAs

are more specific than direct or indirect ELISAs because two antibodies must bind to the target. However, it can be challenging to find compatible antibody pairs because antigen interactions with one antibody may hinder interactions with the second.

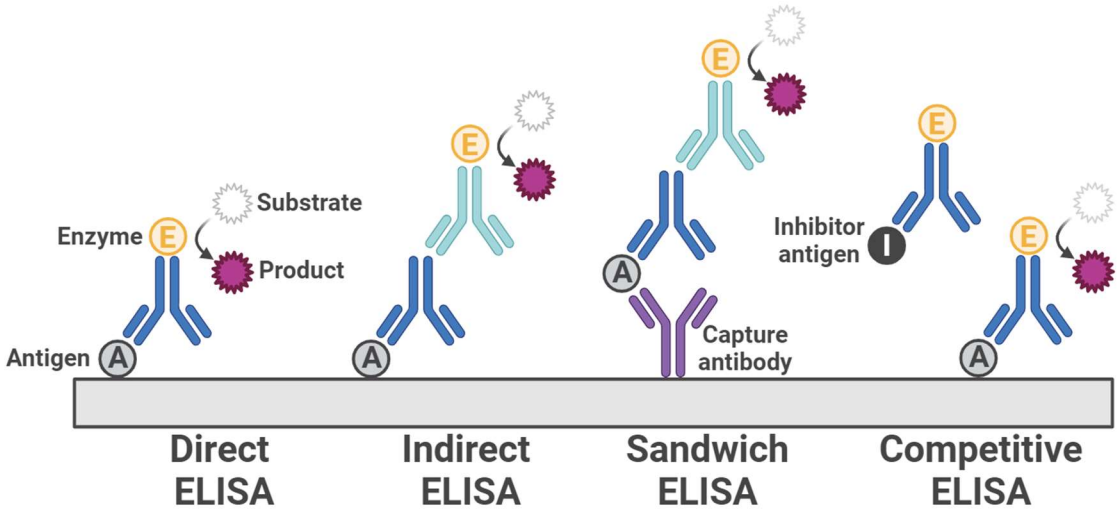

***Figure 1.10**: Summary of common types of ELISA. From left to right: direct, indirect, sandwich, and competitive ELISA formats. Created with Biorender.com.*

The fourth type of ELISA is a competitive ELISA, which is often used to detect small molecules that are difficult to capture in sandwich ELISAs. Competitive ELISAs quantify an antigen in a biological sample using a standardized antigen solution of known concentration. There are many different competitive ELISA formats, but one example begins with wells coated by a known quantity of standardized antigen. Both the detection antibody and the unknown sample are added. Antigen in the sample competes for antibody binding with the immobilized standard, so as the concentration of antigen in the sample increases, less antibody binds to the immobilized antigen, and signal decreases.

Commercial ELISA kits advertise limits of detection on the order of low nanograms to picograms of antigen per mL of sample.[155] More recent ELISA innovations use gold

nanoparticles,[156–158] magnetic beads,[157–159] and droplet microfluidics[160] to increase sensitivity and throughput.

1.5.2 Aptamers

Aptamers are single-stranded oligonucleotides that fold into defined three-dimensional shapes and bind selectively to a target.[31] They can be used as an alternative to antibodies in affinity assays with several advantages. Most notably, aptamers, which are typically only 20-100 nucleotides long, can be chemically synthesized at low cost. Solid-phase synthesis can incorporate fluorescent tags or conjugation sites with high uniformity, so aptamers are immediately ready for detection or pulldown. Aptamers tend to be more stable across long storage periods, warm storage conditions, and multiple freeze-thaw cycles than protein antibodies. Unlike traditional monoclonal antibodies, aptamers are not animal-derived.[149]

Aptamers are selected from random libraries using *in vitro* selection or SELEX (systematic evolution of ligands by exponential enrichment).[161,162] SELEX begins with a library of oligonucleotides that include a 20-80 nucleotide randomized region flanked on both sides by primer-binding regions that allow sequences to be amplified by PCR. Most selections begin with a library of at least 10^{13} unique sequences. The library is incubated with a target of interest, and bound sequences are separated from unbound sequences (Figure 1.11). Bound sequences are then collected, amplified by PCR, and incubated again with the target under increasingly stringent selection conditions. After several rounds of incubation, separation, and amplification, the final pool of binding oligonucleotides is sequenced so that defined aptamer sequences can be synthesized and characterized.

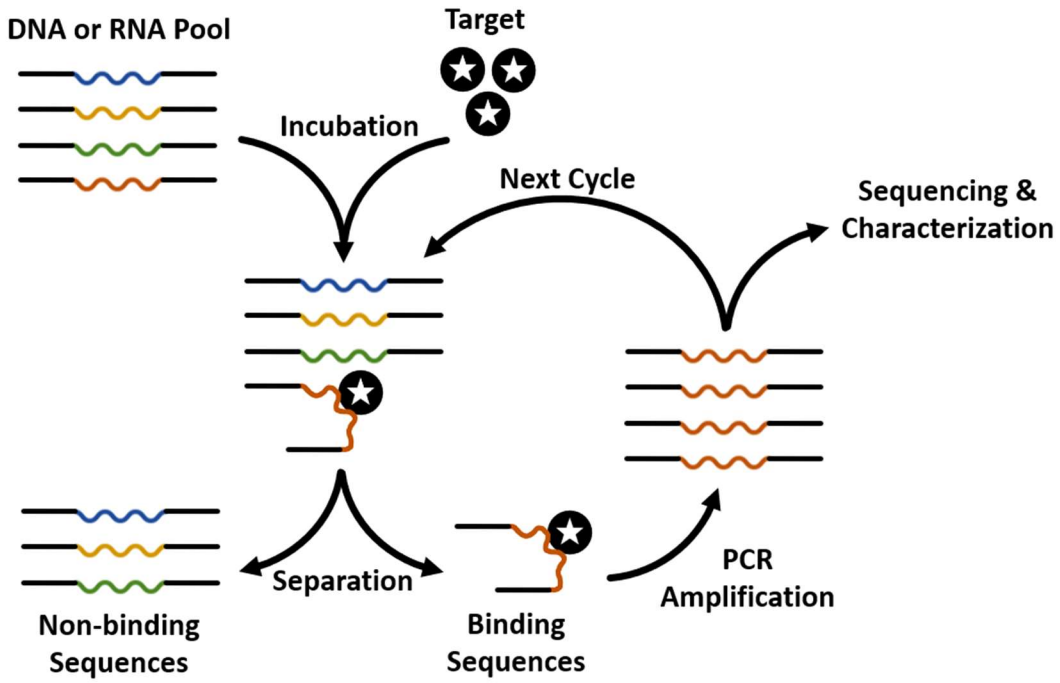

Figure 1.11*: Diagram of aptamer selection using SELEX. A pool of single-stranded DNA or RNA sequences is incubated with a target. Binding sequences are separated from non-binding sequences and amplified by PCR. Amplified sequences can either be sequenced and characterized or incubated again with the target under more stringent selection conditions.*

SELEX protocols vary in their initial library design, incubation conditions, and method for separating binding and nonbinding sequences. Reverse transcription PCR allows for the selection of RNA aptamers,[163] and specialized polymerases can be used with 2'-modified nucleoside triphosphates to amplify DNA aptamers with nuclease-resistant backbones.[164] In conventional SELEX techniques, the target is often immobilized on a solid structure like a column.[162] Sequences that do not bind to the immobilized targets are washed away, and binding sequences are eluted in a subsequent step. Alternatively, the library and ligand can be incubated in solution, and bound complexes are separated from free oligonucleotides using a nitrocellulose membrane.[161] In more recent variations on SELEX, target molecules are immobilized on magnetic beads[165–168] or capillary electrophoresis is used to separate bound and unbound sequences in solution.[166,169,170]

Aptamers are used as molecular recognition agents in affinity assays that are analogous to antibody-based techniques, including lateral flow assays,[171,172] enzyme-linked assays,[173,174] and capillary electrophoresis assays.[175,176] In these assays, the aptamer binds to a target with high affinity and specificity, and binding is measured using fluorescent tags or signal-amplifying enzymes. Unique to aptamers, however, is an additional application in molecular beacon assays. Aptamers often exhibit a conformational change when they bind to their targets. After strategic attachment of reporter moieties like fluorophores, quenchers, and redox indicators, the aptamer can switch from an active (signal generating) form to an inactive form when it binds to the target.[177–180]

Despite widespread interest in aptamer selection and application, aptamers have not experienced the same commercial success as antibodies. One significant barrier to aptamer commercialization is that protocols for aptamer folding and binding are difficult to standardize.[164] Aptamer structure and thermodynamics vary widely from one sequence to the next, even among sequences from the same selection. As a result, affinity assay parameters must be optimized for each new aptamer sequence, and final protocols may vary between assays for different targets. However, advances in the selection, characterization, and fundamental understanding of aptamers, combined with the development of automated analytical instrumentation, may enable future commercialization of aptamer assays.

1.6 Micro Free-Flow Electrophoresis

Free-flow electrophoresis (FFE) is a technique that separates components of a continuously-flowing sample on the basis of their electrophoretic mobility. The separation

occurs in a planar separation channel, where a pressure-driven buffer flow transports the sample from one end to the other. Simultaneously, an electric field is applied perpendicular to the direction of fluid flow, so analytes are deflected laterally based on their electrophoretic mobility, forming distinct analyte streams as the sample travels through the separation channel (Figure 1.12).

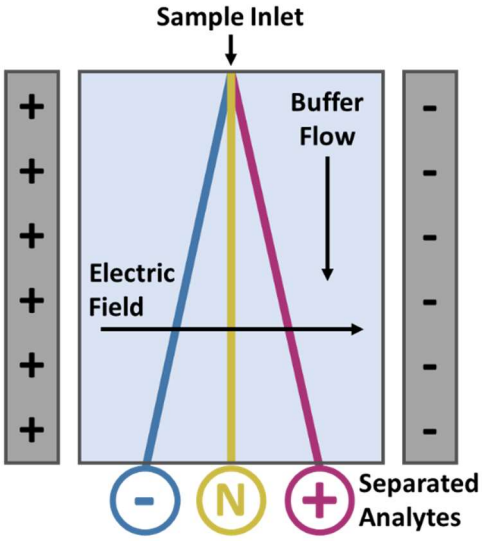

***Figure 1.12**: Diagram of a FFE separation. Sample enters a wide, planar separation channel and is carried by pressure-driven buffer flow. A perpendicular electric field deflects analytes laterally based on their electrophoretic mobility. Here, equally-sized analytes with different net charges (negative, neutral, and positive) are separated into distinct streams as they travel through the channel.*

FFE was first developed over six decades ago, with a shallow separation channel confined between two large (50 cm × 50 cm) glass plates.[181,182] More recently, the separation channel has been miniaturized, with a depth on the order of 50 µm and length × width dimensions on the order of 1 to 2 centimeters or smaller.[183,184] Miniaturization reduces sample volume requirements, decreases flow path variability, and improves sensitivity. µFFE is therefore an attractive technique for sensitive and continuous detection of a wide range of analytes.

1.6.1 µFFE Theory

The basis of a µFFE separation is lateral deflection as analyte molecules move through the electric field applied across the separation channel.[185,186] Deflection distance (d) is determined by the product of the analyte's total mobility (μ_{total}), the electric field strength (E), and the amount of time the analyte spends in the field (t):

$$d = \mu_{total} E t \tag{1.2}$$

Separation power (Et) can be increased by increasing the strength of the electric field or the residence time of an analyte in the channel.[187] Residence time increases with increasing distance from the sample inlet and decreasing linear velocity of the running buffer.

Band broadening in µFFE is governed by the (1) initial width of the sample stream, (2) the diffusion of sample molecules over time, and (3) hydrodynamic broadening that arises from the parabolic profile of sample streams as they travel laterally.[187] The initial stream width is determined by the geometry of the sample inlet. For example, a sample capillary with a small inner diameter will introduce a narrower stream than a sample capillary with a large inner diameter. Dead volume at the sample inlet will contribute to initial stream width, causing spatially broader peaks for all analyte streams. Diffusion increases as a function of the time analytes spend in the separation channel. Hydrodynamic broadening increases as the lateral deflection distance and separation channel depth increase.

Since samples are continuously introduced, separated, and detected in µFFE, it can be a valuable technique for temporal measurements. For example, the signal intensity of a single analyte stream or a single position on the separation channel can be recorded over

time to monitor changes in sample composition. Analyte adsorption to the surface of the separation channel causes peak broadening in the temporal dimension. The extent of temporal broadening for small molecules and protein peaks has been quantified in μFFE devices fabricated in glass,[188] ABS (acrylonitrile butadiene styrene),[189] and COC (see Chapter 5). Critically, plug injection studies have demonstrated that surface adsorption contributes to peak broadening exclusively in the temporal dimension. It does not influence spatial broadening.[188,189] This allows μFFE to separate analytes efficiently regardless of their interactions with the device's surface.

1.6.2 Applications of μFFE

In addition to fluorescent dye separations often used to demonstrate the technical performance of design and fabrication improvements,[190–193] μFFE has been used to separate a wide range of biological analytes, including amino acids,[194,195] nucleic acids,[196,197] proteins,[188,189,197–200] aptamers,[201–204] organelles,[205,206] and whole bacterial cells.[207] There is also versatility in the electrophoretic separation modes available.[208] The majority of μFFE experiments described in this section use zone electrophoresis, but isotachophoresis[209] and isoelectric focusing[197,205,210–212] electrophoresis have also been implemented in μFFE devices.

A specific advantage of μFFE over other separation techniques is its continuous nature. While other separations use a single, discrete sample, μFFE uses a continuously refreshing feed of sample, which is constantly separated and detected. This makes μFFE an appealing technique for monitoring the composition of a sample over time, a feature

that has been demonstrated in applications of μFFE for reaction monitoring,[213–217] gradient separations,[201,218] and multidimensional separations.[194,195,219]

Chemical reactions can be performed, separated, and monitored on a single, integrated μFFE platform.[213–215] Furthermore, these reaction-monitoring μFFE platforms have been integrated with mass spectrometry for unambiguous identification and quantification of non-fluorescent reaction products.[216] A mass spectrometry-coupled μFFE device has been used to monitor the composition of analyte streams at multiple chip positions over the course of a ten minute separation.[217]

μFFE is also well suited for optimization and characterization using flowing gradients to quickly scan a range of reagent or buffer conditions. Rather than preparing and separating a series of samples with varying reagent concentrations, a single, continuous gradient can be injected onto the device, with a parameter of interest changing over time. Rapid acquisition (on the order of several frames per second) allows users to collect hundreds or thousands of data points across the entire gradient over the course of a few minutes. For example, a gradient of increasing ligand concentration was used to construct an aptamer binding curve, with 300 points collected in a total of 5 minutes.[201] Gradients have also been used to optimize separation conditions by gradually changing the composition of the separation buffer.[218]

μFFE can be combined with orthogonal separation techniques to dramatically increase peak capacity. Nano-liquid chromatography (nLC)[194,219] and capillary electrophoresis (CE)[195] have both been coupled to μFFE. In both cases, a sample is injected into the first dimension (nLC or CE), is separated into temporally resolved peaks, and

eluted directly from the column or capillary into the µFFE separation channel. There, analyte peaks are separated on the basis of their electrophoretic mobility, and the progress of the two-dimensional separation is continuously monitored by fluorescence detection. Figure 1.13 shows an example of a nLC × µFFE separation of a Chromeo P503-labeled tryptic digest of bovine serum albumin (BSA). nLC × µFFE and CE × µFFE achieved peak capacities of up to 264 and 1053 peaks per minute, respectively, over the course of 2-10 minute separations.[194,195]

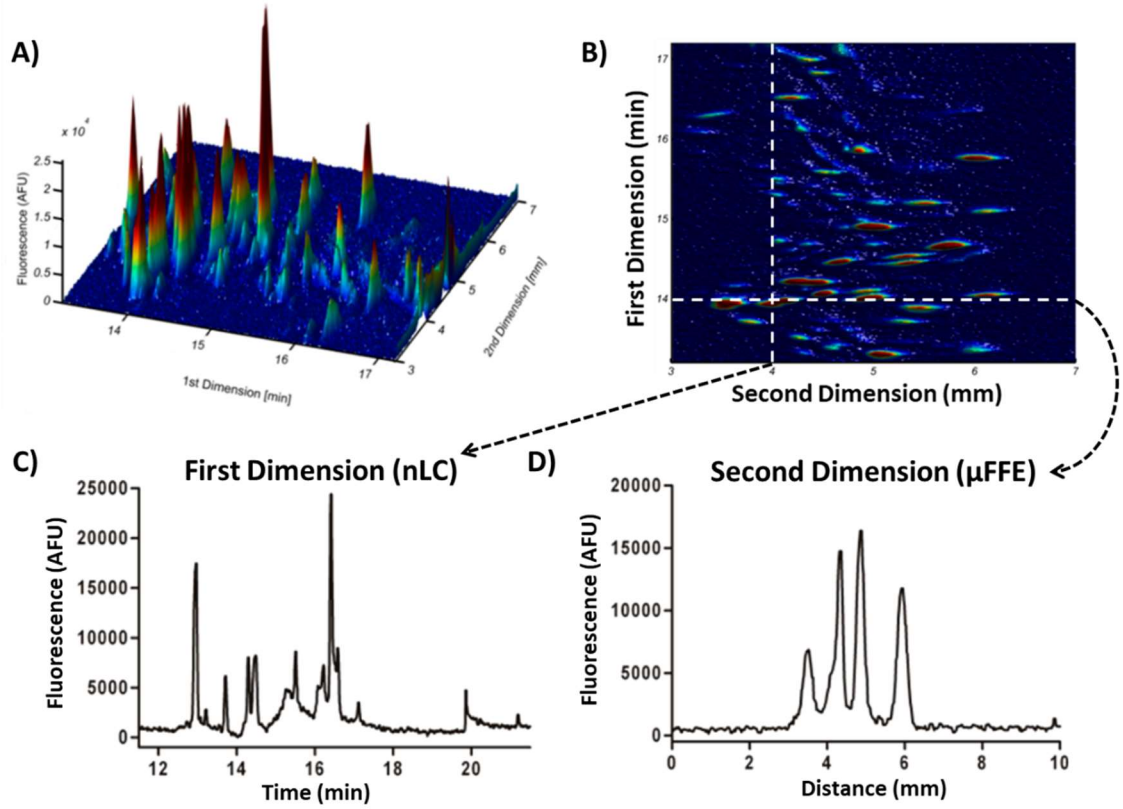

***Figure 1.13**: Two-dimensional nLC × µFFE separation of a Chromeo P503-labeled BSA tryptic digest, shown in A) 3D view and B) top view. C) An extracted chromatogram shows fluorescence intensity over time at a single position (4 mm) on the separation channel. D) An extracted line scan shows fluorescence intensity across the width of the separation channel at a single point in time (14 minutes). Adapted from Geiger, Frost, and Bowser.[219] Reprinted with permission from Analytical Chemistry, 86(10). Copyright 2014 American Chemical Society.*

Another relevant application of μFFE is its use in microfluidic affinity assays. Affinity reagents like aptamers and antibodies bind to biological targets with high affinity and selectivity (see section 1.5), and the electrophoretic mobility of the bound complex differs from the mobility of either the affinity reagent or target alone. When labeled with fluorescent tags, these affinity reagents can act as high-specificity probes for detecting biomolecules of interest, expanding the range of analytes that can be monitored through fluorescence-detection μFFE. Like other microfluidic affinity assays, the continuous flow in μFFE eliminates the multi-wash requirements that dramatically increase the turnaround time of traditional ELISA techniques. The μFFE separation also adds a level of selection orthogonal to binding specificity that can be used to distinguish between complexes with multi-valent, oligomeric, or stoichiometrically distinct species that would be identical in a traditional, single-mixture affinity assay.[220] Aptamer-based affinity assays in μFFE devices have been used to detect antibodies,[201,202,204,220] enzymes,[201] amyloid aggregates,[204,221] and exosomes.[204] These assays have been combined with dynamic sample gradients for rapid kinetic characterization[201] and with high-sensitivity confocal microscopy for single-molecule detection.[204]

1.6.3 Materials: fabrication, durability, and performance

μFFE devices have been fabricated in a variety of materials, each with its own combination of advantages and challenges. Compared to other microfluidic devices, μFFE devices have several features that warrant additional consideration for design and fabrication. First, the aspect ratio of the separation channel, which is typically 10 to 100 μm deep and 1 to 2 cm wide, imposes some restrictions on fabrication methods and

materials. The channel must be uniform and cannot collapse during fabrication or operation. Second, electrolysis at the buffer-submerged electrodes produces gas bubbles that reduce the electric field and disrupt fluid flow. μFFE devices therefore need a strategy for clearing electrolysis products from the device or suppressing their formation in the first place.

Several design strategies have arisen in response to the electrolysis issue.[186] Larger-scale FFE devices have traditionally used membranes to physically separate the electrode and separation channels, and some μFFE devices use a similar approach.[183,184,222] These membranes are permeable to ions, thus transmitting current to the separation channel, but they block electrolysis bubbles, which are continuously flushed out of the device. Alternatively, the depth of the electrode channels can be increased relative to the depth of the separation channel, increasing the linear velocity of buffer in the electrode channels to more rapidly clear electrolysis products.[218] Other devices have positioned off-chip electrodes downstream of fluid flow and used conductive electrolyte solutions to carry an electric field back to the separation channel.[200] Buffer additives can also be used to chemically suppress electrolysis.[192]

The most widely used fabrication techniques for μFFE devices use photolithography, either directly or for master mold production. Photolithography has been used to etch features into silicon[183] and glass[190,192,223–225] substrates. In other glass devices, the channels consist of photopatterned materials spun onto a the substrate.[205] Liquid phase photolithography has been used to eliminate bonding steps from the glass fabrication workflow.[222,226] Femtosecond laser processing can be used as an alternative to

photolithography for pattern transfer onto fused silica substrates.[193] Glass devices have high optical transparency and long functional lifetimes, but their fabrication methods are expensive and low-throughput. They also have a negatively-charged surface that adsorbs positively-charged analytes and therefore require surface treatment to be compatible with many proteins and small molecules.[188]

Another popular device material is PDMS, which is typically cast onto molds produced by photolithography.[199,227,228] PDMS μFFE devices incorporate support pillars in the separation channel, which prevent deformation or collapse. A glass cover slide or window is typically incorporated for improved optical transparency during detection.[227,229] PDMS fabrication is more scalable than glass etching, but the PDMS surface is significantly hydrophobic, leading to protein adsorption and difficulty displacing gas bubbles with aqueous solution.[230]

Recent developments in the fabrication of μFFE devices have increasingly focused on rigid polymer materials. Like glass devices, rigid polymer devices can be designed without support pillars obstructing the separation channel, and they tend to be more durable than soft PDMS devices. Fabrication techniques including 3D printing,[231–233] injection molding,[234,235] and computer numerical control milling[236] tend to offer higher throughput and faster prototyping than traditional lithography and etching workflows. A variety of polymers are available for microfabrication, each with its own chemical characteristics. To date, μFFE devices have been fabricated in ABS,[231] poly(methyl methacrylate) (PMMA),[197] polystyrene (PS),[234] cycloolefin polymer (COP),[235] and COC.[236]

1.7 Scope of Thesis

The scale and complexity of biological systems pose challenges to accurate detection and quantification. Some phenomena are simply too small, too fast, or too rare to be measured by existing technology. This thesis describes the development of microfluidic platforms capable of addressing biological questions at scales and timeframes that would be impossible using traditional methods. Chapters 2 and 3 present a droplet microfluidic platform for the quantification of catalytic oligonucleotides in libraries of random-sequence oligonucleotides. Chapter 2 describes the technical design of the platform in detail, along with its performance in library screening experiments. Chapter 3 examines the activity of a known DNA catalyst incubated in droplets with a fluorogenic substrate. Chapters 4 and 5 present advances toward a μFFE affinity assay for continuous protein quantification. Chapter 4 characterizes surface adsorption in COC μFFE devices using two-dimensional nLC × μFFE separations. These experiments demonstrate that COC devices have low protein adsorption, a requirement for temporal measurements in continuous affinity assays. Chapter 5 presents the initial development of an aptamer-based μFFE affinity assay for tumor necrosis factor α (TNFα). Finally, Chapter 6 summarizes the progress made in the areas of catalyst screening and μFFE affinity assays, as well as future directions for both projects.

Chapter 2: Development of a droplet microfluidic platform for the quantification of catalytic oligonucleotides in random-sequence libraries

2.1 Summary

DNA and RNA catalysts are an exciting alternative to protein enzymes because they are chemically synthesized, have good stability, and can be selected from libraries of entirely random oligonucleotide sequences. However, our knowledge of the overall scope of nucleic acid catalysis is limited. For example, the maximum rates, environmental preferences, and frequency of nucleic acid catalysts in random-sequence libraries are unknown. Here, we describe the development of a droplet microfluidic platform that can screen DNA libraries for catalytic activity in cleavage reactions with a fluorogenic substrate.

Two droplet microfluidic platforms were constructed. On the first platform, droplets were generated in a commercial microfluidic tee and detected in a PTFE capillary. This platform produced uniform, stable droplets and achieved high screening throughput. However, due to the large volume of the droplets, the platform had limited sensitivity to slow-acting or limited-turnover catalysts. A second platform used PDMS devices to generate and detect 6-fold smaller droplets, maintaining high screening rates while significantly increasing the sensitivity of the platform to slow catalysts.

A 90-nucleotide DNA library was screened for catalytic activity after incubation with three fluorogenic substrates: two sugar-substituted fluorescein analogs as well as a fluorescently-labeled RNA oligonucleotide. No evidence of catalysis was observed for any of the three substrates, and the sensitivity of the platform was limited not by droplet size, throughput, or detection sensitivity, but by the noise inherent in the system, which causes false positive events at low frequencies. To overcome this limitation, future experiments

must either investigate reactions with higher catalytic frequencies or reduce the random noise and false positive rate of the platform.

2.2 Introduction

Catalytic nucleic acids were first discovered in nature, where RNA sequences called ribozymes perform self-processing reactions like cleavage and splicing.[6,7,11] The catalytic repertoire of nucleic acids was then expanded to novel reactions and to DNA or modified nucleic acid catalysts through *in vitro* selection. These selection experiments begin with a library of random-sequence oligonucleotides and apply consecutive rounds of selective pressure that favor the collection or amplification of catalytic sequences over non-catalytic sequences.

Typically, *in vitro* selection experiments are designed around intramolecular reactions. For example, Breaker and Joyce isolated the first DNA catalyst by immobilizing a DNA library on a streptavidin matrix, incubating it in the presence of Pb^{2+}, washing cleaved DNA from the matrix, and amplifying the resulting self-cleaving catalytic sequences by PCR.[32] Alternatively, DNA catalysts for many cleavage,[38–40] ligation,[44–46,48] and modification[41,42] reactions have been identified by incorporating the substrate moiety of interest and a random-sequence region into a hairpin-shaped oligonucleotide. In this selection design, catalysts can be isolated by any capture method specific to the desired reaction product.[2] The hairpin ensures that the product of a successful reaction will be tagged with the catalytic sequence that acted on it (Figure 2.1).

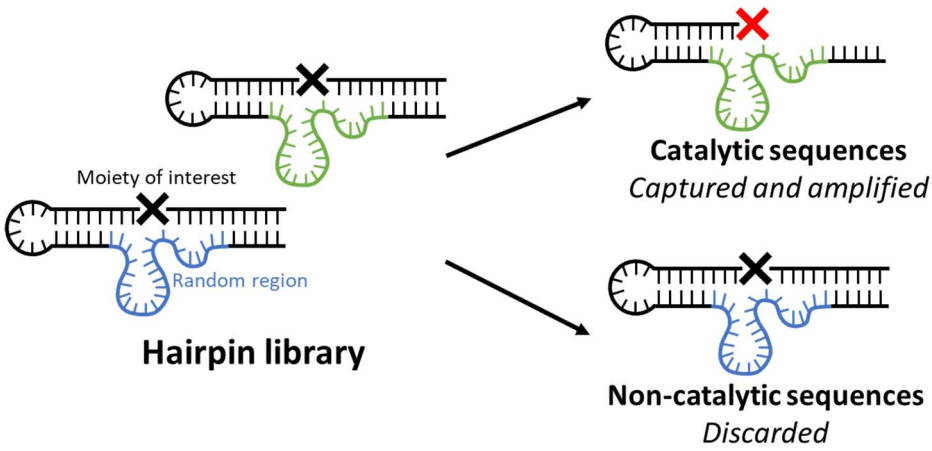

***Figure 2.1**: Hairpin library design for in vitro selection of catalytic oligonucleotides.*

These *in vitro*-selected nucleic acid catalysts are of particular interest in therapeutic, diagnostic, and biochemical applications because they perform many of the same reactions as protein enzymes but are cheaper and more shelf-stable than proteins. However, to compete with the sensitivity and effectiveness of enzyme technologies, oligonucleotide catalysts must be able to operate with high turnover rates, performing many reactions in short periods of time. In a meta-analysis of protein repository data, Bar-Even *et al.* found that the median rate constant of all literature-reported enzymes was k_{cat} = 13.7 reactions per second.[77] Many enzymes popular in biochemical applications are significantly faster. Nucleic acid catalysts, on the other hand, tend to be significantly slower. Although the fastest known naturally-occurring ribozymes have rate constants on the same order of magnitude as an average protein enzyme,[12,16] the best-characterized DNA catalysts from *in vitro* selection are over 100-fold slower.[34]

In vitro selection has produced a wide range of nucleic acid catalysts, but it also imposes a number of limitations. As a consequence of the intramolecular reaction designs in typical *in vitro* selection methods, structural features that promote selection are not

necessarily relevant to the catalytic function of the molecule. Library molecules are often confined in hairpin or loop structures before the selection begins. These shapes simplify selection but are not necessarily required for catalysis. Other catalytic structures may be excluded by the design of the experiment. It is therefore possible that laboratory selection has limited the structural (and therefore functional) diversity of isolated nucleic acid catalysts. Intramolecular reactions are also single turnover events, which makes it difficult to design experiments that select for faster or higher-turnover catalysts.

More broadly, our generalized knowledge and assumptions about nucleic acid catalysts have been shaped by *in vitro* selection. Most nucleic acid catalysts were selected under similar constraints and then characterized. It is difficult to determine whether observed characteristics are fundamental properties of nucleic acids or simply a byproduct of the selection process.

This leaves us with many fundamental questions about the scope of nucleic acid catalysis: How common are nucleic acid catalysts among random DNA or RNA sequences? How fast can they act? What types of conditions do they prefer? What types of reactions can they catalyze? To answer these questions, we need to study nucleic acid catalysts in a different context. First, the intramolecular reaction design traditionally used in catalyst selection should be replaced with an intermolecular reaction design that promotes high turnover rates and structural diversity. Second, nucleic acid catalysis should be investigated at the population level, as opposed to isolating and characterizing individual sequences.

In response to these requirements, we have developed droplet microfluidic platforms to quantify the abundance of catalytic oligonucleotides in libraries of random-sequence DNA or RNA (Figure 2.2). The library is loaded into water-in-oil droplets with a substrate that becomes fluorescent when it is cleaved. The droplets act as picoliter-scale reaction containers. During incubation, a single catalytic molecule can cleave thousands of substrate molecules, and the fluorescent product will accumulate in the droplet. Therefore, any droplet that contains a sufficiently fast catalyst will be fluorescent after incubation (Figure 2.2A). Droplets that do not contain a catalyst will be non-fluorescent. The fluorescence intensity of each droplet is measured as they flow past a detector. From the ratio of fluorescent to non-fluorescent droplets, we can quantify the frequency of catalytic sequences in the original library (Figure 2.2B). This unique approach will allow us to study changes in catalyst frequency across different reactions and reaction conditions, addressing for the first time many interesting and unanswered questions about the scope of nucleic acid catalysis.

The expected scarcity of catalysts places very high technical demands on the microfluidic platform. Existing protocols for nucleic acid catalyst selection isolate a only handful of catalysts from libraries that contain 10^{13} to 10^{16} molecules.[1] The throughput of the microfluidic platform must therefore be high enough to identify rare catalysts among trillions of non-catalytic molecules. To maximize screening throughput, the random-sequence library is loaded into droplets at a very high concentration, and droplets are detected rapidly. Although each droplet contains billions of unique DNA sequences, most droplets will not contain a catalyst. For meaningful quantification of catalyst frequency,

the platform must be able to accurately detect both negative (catalyst-free) and positive (catalyst-containing) droplets.

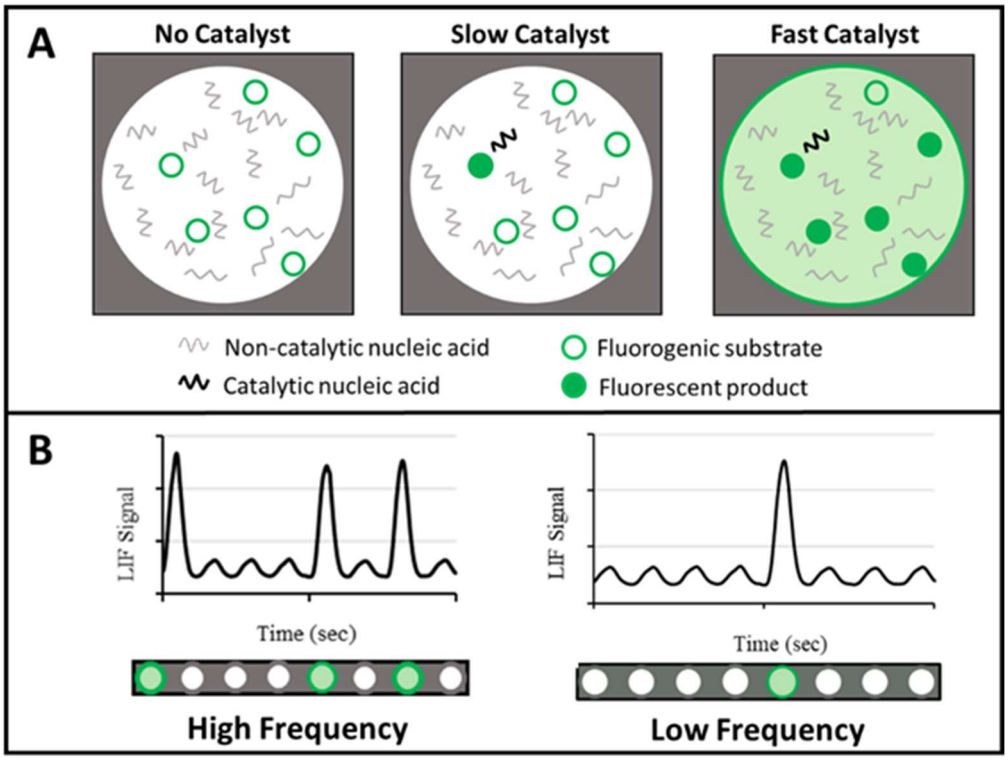

***Figure 2.2**: A) Schematic representation of catalyst activity in droplets. A single catalyst cleaves many fluorogenic substrates to produce a detectable signal. B) Schematic representation of high and low catalyst frequency.*

The few droplets that do contain a catalyst will have only a single copy of that catalytic sequence. The platform must therefore be sensitive enough to detect a single catalytic molecule. Droplets are incubated before detection so that catalysts with sufficient turnover efficiency can produce a detectable amount of fluorescent product, typically on the order of ten thousand to one million fluorophore molecules.

Two droplet microfluidic platforms were constructed for DNA catalyst quantification (Figure 2.3). The first used a commercial microfluidic tee for droplet generation, a long length of capillary for incubation, and a sheath flow cuvette for

detection. The second used custom PDMS devices for both droplet generation and detection. Both platforms were used to screen a library of 90-nucleotide, random-sequence DNA for catalytic cleavage of several fluorogenic substrates. In this chapter, the performance of both platforms is discussed in the context of the technical demands described above.

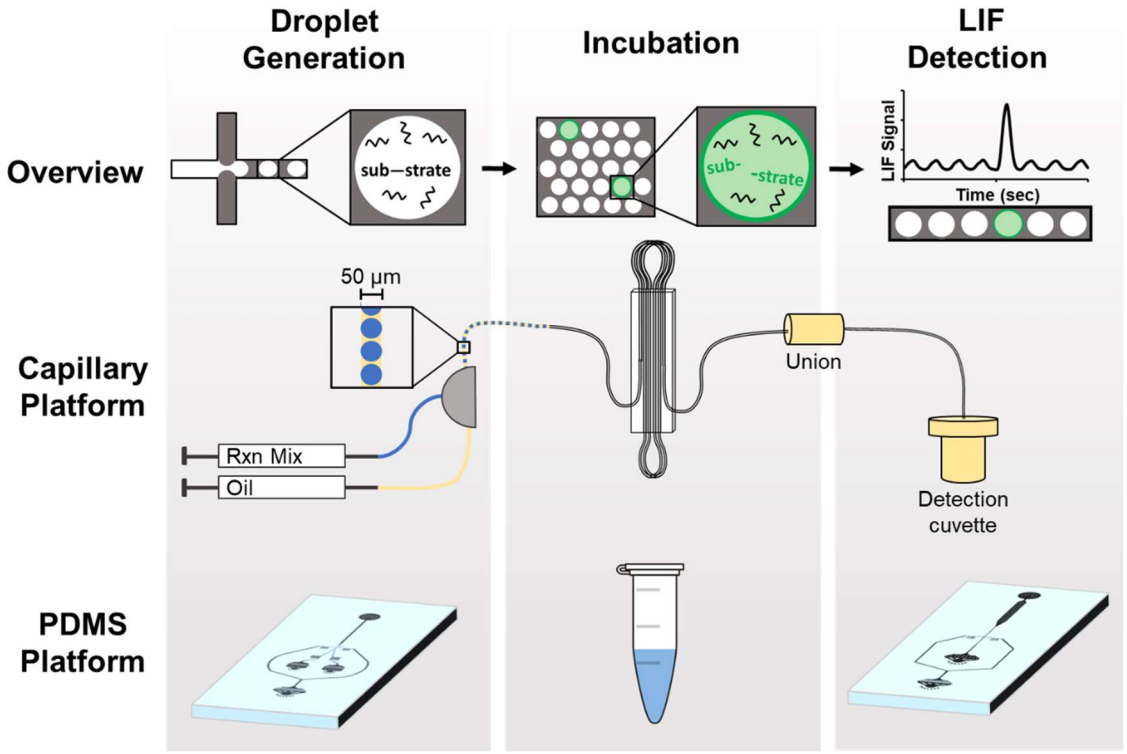

Figure 2.3*: Overview of microfluidic approaches to the quantification of catalytic oligonucleotides. (Top): A library of random DNA sequences is partitioned into droplets with a fluorogenic substrate. Over the course of incubation, droplets that contain a catalytic sequence become fluorescent. The fluorescent intensity of each droplet is read to determine the frequency of catalysts in the original library. (Middle): A capillary-based platform for droplet generation and detection. (Bottom): PDMS devices for droplet generation and detection.*

2.3 Experimental

2.3.1 Chemicals and reagents

All solutions were made using deionized water (18.3 MΩ, Milli-Q; Millipore, Bedford, MA). Chemicals were purchased from Sigma Aldrich (St. Louis, MO) unless

otherwise specified. Droplets were generated and stored in Bio-Rad (Hercules, CA) ddPCR Droplet Generation Oil for Probes (capillary-based platform) or for EvaGreen (PDMS platform). Fluorescein di-β-D galactopyrianoside (FDG) and fluorescein mono-β-D galactopyrianoside (FMG) were purchased from Abcam (Cambridge, UK). A stock fluorescein solution was prepared by dissolving fluorescein disodium salt at a concentration of 10 mM in buffer containing 100 mM Tris (pH 7.5), 100 mM NaCl, 100 mM KCl, 50 mM $MgCl_2$, 2 mM $ZnCl_2$, and 20 mM $MnCl_2$. Oligonucleotides (sequences shown in Table 2.1) were synthesized by Integrated DNA Technologies (IDT, Coralville, IA), resuspended in nuclease-free water (IDT), and stored in aliquots at -20 °C.

***Table 2.1**: Oligonucleotide sequences (N denotes a position with equal probability A, C, G, or T)*

	Sequence (5' → 3')
90N Library	NNN NNN NNN NNN NNN NNN NNN NNN NNN NNN NNN NNN NNN NNN NNN NNN NNN NNN NNN NNN NNN NNN NNN NNN NNN NNN NNN NNN
Poly T	TTT TTT TTT TTT TTT TTT TTT TTT TTT TTT TTT TTT TTT TTT TTT TTT TTT TTT TTT TTT TTT TTT TTT TTT TTT TTT TTT TTT
Seq832 (Negative Control)	TTC CGT CCT CGT CGT AAC TAT CAG GGC ATT CTT GTA AAT CCG CCG GTA CCA CTC AAT TCC TCC CAC TCC CCA TAT TGT CCG CGT GTG ACT
RNA Substrate	/56- FAM/ACA ACC rGrUC ACC A/3IABkFQ/

2.3.2 Tubing, fittings, and connections

Fused silica capillary tubing (O.D. 360 μm, I.D. 50 μm) was purchased from PolyMicro Technologies (Phoenix, AZ). The PTFE capillary (O.D. 360 μm, I.D. 50 μm) used on the capillary-based platform and PTFE tubing (OD 1/32 in., ID 0.022 in.) used with PDMS devices were purchased from McMaster-Carr (Elmhurst, IL). Microfluidic tees, unions, and ferrules were purchased from Vici Valco Instruments (Houston, TX).

2.3.3 Capillary-based platform for droplet generation and detection

A cross-flow droplet generation setup was constructed from commercially available fittings (Figure 2.4). In each experiment, the oil phase and an aqueous phase were loaded into separate gas tight syringes on a syringe pump (Harvard Apparatus, Holliston, MA). Each syringe was connected to a stainless-steel tee with an inner diameter of 50 µm by a short piece of fused silica glass capillary. The tee outlet was connected to a 5-foot segment of PTFE storage capillary.

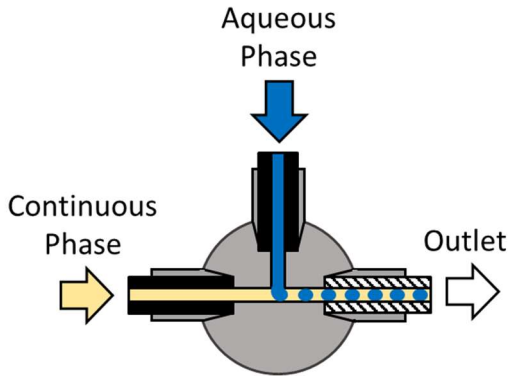

Figure 2.4*: Schematic of cross-flow droplet generation in a microfluidic tee. Aqueous and continuous phases enter the tee in fused silica capillaries (black shading), meet at a cross junction inside the tee (grey shading), and proceed to the outlet in alternating segments. Droplets leave the outlet in Teflon tubing (striped shading), which has a hydrophobic surface that promotes the formation of water-in-oil droplets.*

To prevent interactions between droplets and facilitate droplet reinjection, droplets were stored in PTFE capillary between generation and detection. Approximately 5 continuous feet of PTFE capillary was coiled and secured to a glass slide. This coiled capillary was easily detached from the generation tee for storage, imaging, and incubation. During incubation periods, storage capillary was sealed in an opaque, water-tight container and submerged in a temperature-controlled water bath. To assess droplet quality and

stability, droplets were imaged in their storage capillary using a Nikon (Tokyo, Japan) SMZ1500 microscope.

For detection, droplets were pushed from the storage capillary into a piece of PTFE capillary that was permanently threaded through a sheath flow cuvette. A 100 µm PEEK union connected the two PTFE segments. The PTFE capillary was threaded completely through the cuvette so that droplets were contained in the capillary throughout detection. DI water was flowed between the PTFE capillary and the cuvette walls to minimize light scatter.

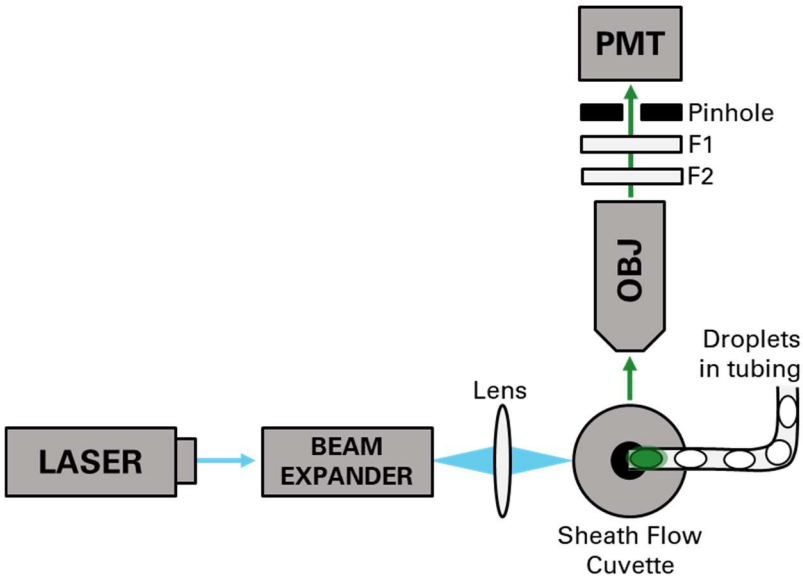

Figure 2.5*: LIF setup for droplet detection in PTFE capillary. The laser bean is expanded and focused on droplets inside a sheath flow cuvette. Emitted light passes through an objective, a 520 nm bandpass filter (F2), a 488 nm notch filter (F1), and a pinhole aperture before detection by a PMT.*

A laser-induced fluorescence (LIF) system was used to detect droplets as they streamed through the sheath flow cuvette (Figure 2.5). A 488 nm laser (Sapphire 488-50, Coherent, Santa Clara, CA) was focused on the cuvette by a beam expander and focusing lens. Emitted light was collected by a 20× A-plan objective (Zeiss, Oberkochen, Germany)

positioned perpendicular to the laser line. After the objective, a 520 nm bandpass filter (Intor, Socorro, NM) blocked extraneous wavelengths, a 488 nm notch filter (Edmund Optics, Barrington, NJ) blocked excitation light, and an adjustable pinhole aperture suppressed scattered light. Photons were then detected by a photomultiplier tube (PMT, from Hamamatsu, Shizuoka, Japan).

2.3.4 PDMS device fabrication

PDMS devices for droplet generation and detection were designed and fabricated based on the masks and protocols described by Mazutis *et al* (Figure 2.6).[237] All photolithography was performed in the Minnesota Nano Center. Briefly, a clean, 4-inch silicon wafer was spin-coated with 3 mL of SU-8 2025 photoresist (Kayaku, Westborough, MA) for 15 seconds at 500 rpm followed immediately by 30 seconds at 3,000 rpm (CEE spinner, Saint James, MO) for an expected thickness of 25 μm. Channels in the final PDMS devices were 30-33 μm deep. The coated wafer was prebaked at 65°C for 1 minute and then 95°C for 3 minutes. After the wafer cooled to room temperature, a patterned photomask (Fineline Imaging, Colorado Springs, CO) was aligned with the wafer, and the pattern was transferred to the photoresist through a 20 second UV exposure at a power of 10 mJ cm^{-2} (MA6 Mask Aligner, Karl Suss, Munich, Germany). The exposed wafer was baked at 65°C for 1 minute and then 95°C for 3 minutes. Unreacted photoresist was developed by immersion for 4 minutes in propylene glycol monomethyl ether acetate (Sigma-Aldrich, St. Louis, MO). The master mold was rinsed with isopropanol, dried, and tempered at 150°C for 30 minutes. To prevent PDMS adhesion, mask features were

silanized in a vacuum desiccator for 1 hour with 50 µL of trichloro-perfluorooctanyl silane (Sigma-Aldrich).

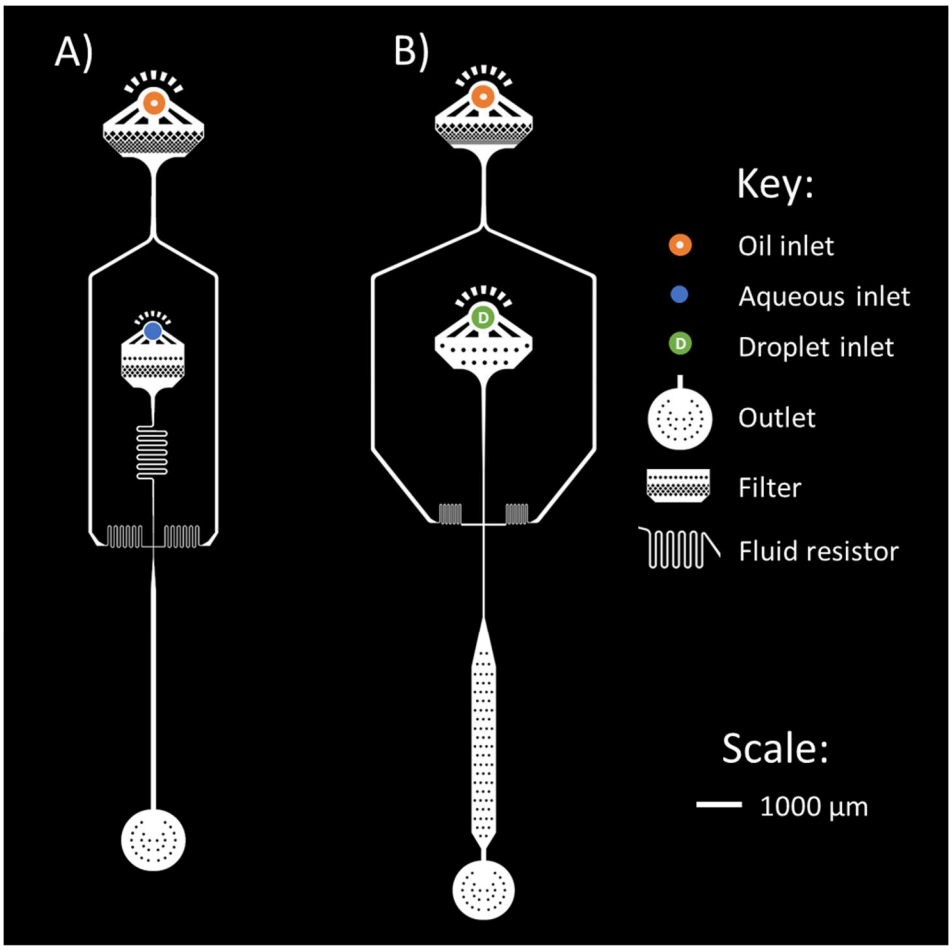

Figure 2.6*: Photomask designs for single aqueous inlet droplet generation device (A) and droplet detection device (B).*

Sylgard 184 and its curing agent (Electron Microscopy Sciences, Hatfield, PA) were mixed in a 10:1 ratio by mass, degassed, and poured over the master mold. The poured PDMS was degassed again to remove small bubbles along device features and cured overnight at 60°C. After curing, devices were cut and peeled from the mold. Inlet and outlet ports were punched using a 0.75 mm biopsy punch (Miltex, York, PA). The PDMS was bonded to a glass microscope slide (McKesson, Richmond, VA) by plasma bonding. The

feature side of the PDMS was exposed to air plasma for 1 minute at 75% intensity, pressed onto a plasma-treated glass slide, and baked on a hotplate at 120°C for 10 minutes. Channels were treated with Aquapel (PGW Auto Glass, Cranberry Township, PA) to create a uniform, hydrophobic surface.

2.3.5 Droplet generation and detection in PDMS devices

To generate droplets in PDMS devices, oil and aqueous phases were loaded into gastight syringes on separate syringe pumps. Syringes were connected to droplet generation device (Figure 2.6A) inlets using PTFE tubing. In a typical experiment, the oil and aqueous flow rates were both 180 μL/hour. Droplets exited the device through a short piece of PTFE tubing and were collected in excess oil in a microcentrifuge tube. Droplets could be incubated in these tubes for several days at 37°C or several weeks at room temperature without significant coalescence or leakage.

Incubated droplets were drawn into a gastight syringe, and the syringe was positioned upright on a syringe pump so that droplets gathered near the needle, and excess oil collected near the plunger. The droplets were re-injected into a detection device (Figure 2.6B) at 10 μL/hour and spaced on the device by HFE-7500 (Oakwood, Estill, SC) flowing from a separate syringe at 100 μL/hour. A custom epifluorescence system was used to detect droplets as they passed single file through a channel on the device (Figure 2.7). A 488 nm laser was focused using a 506 nm longpass dichroic mirror (Edmund Optics) and a 20× A-plan objective (Zeiss, Jena, Germany). Fluorescence from the droplets was detected following the same path as the excitation light. After passing through the dichroic mirror, fluorescent signal was collected by a 1× Zeiss tube lens and filtered through a 520

nm bandpass filter (Intor) and 488 nm notch filter (Edmund Optics) before detection by a PMT (Hammamatsu).

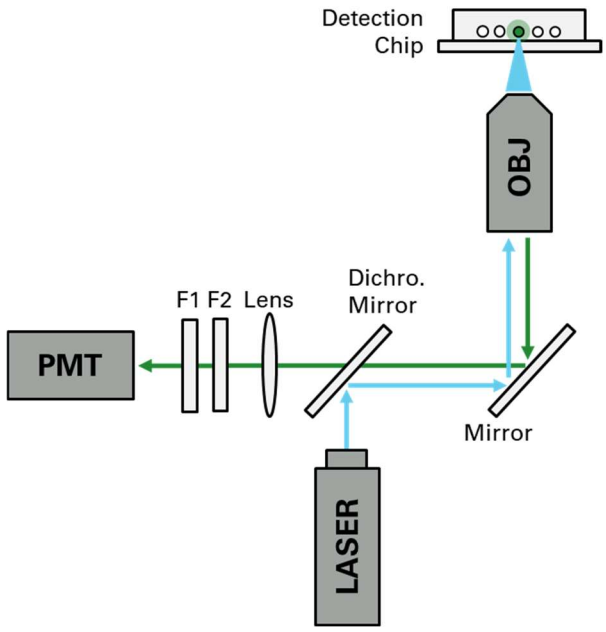

***Figure 2.7**: Epifluorescence optical setup for droplet detection in PDMS devices.*

2.3.6 Data analysis

Fluorescence intensity was detected over time by a PMT and tabulated in LabVIEW. Peaks were identified by a custom Matlab script using the "findpeaks" function and filtered to remove baseline noise and broad peaks representing coalesced droplets. For library screening experiments, custom R scripts were used for visualization and statistical analysis of peak data. These scripts calculated automated thresholds based on the intensity distribution of the peaks, allowing for automated frequency calculations.

2.3.7 Library screening

The 90N DNA library screened in all experiments was 90 nucleotides long and fully random. For library screening experiments on the capillary-based platform, 100 μM 90N library was incubated with 100 nM FDG. Library and substrate were combined

immediately before droplet generation. The final buffer concentrations during incubation were 80 mM Tris (pH 7.5), 40 mM $MgCl_2$, 1.6 mM $ZnCl_2$, 80 mM NaCl, and 80 mM KCl. Negative control droplets contained the same buffer and FDG substrate, but 100 μM seq832 negative control replaced the random-sequence library. Fluorescence was compared to droplets containing 10 nM fluorescein in incubation buffer.

For library screening experiments on the PDMS device platform, 50 μM 90N library was incubated with 100 nM FDG, FMG, or RNA substrate. The final buffer concentrations during incubation were 18 mM Tris (pH 7.5), 4.5 mM $MgCl_2$, 0.9 mM $ZnCl_2$, 4.5 mM NaCl, and 90 mM KCl. Negative control droplets contained the same buffer and substrate with 50 μM seq832 negative control instead of the random-sequence library.

2.4 Results and Discussion

There are two fundamental requirements of a droplet microfluidic platform for DNA catalyst quantification. First, it must have a high throughput, allowing trillions or even quadrillions of library sequences to be screened on reasonable timescales. Low throughput will limit the minimum catalytic abundance the platform can quantify. Initially, we aimed for a minimum throughput on the order of 10^{13} library sequences per screening experiment, consistent with the size of libraries used in some *in vitro* selection experiments.[1]

Second, the platform must be sensitive enough for single molecule detection. Droplets will ultimately contain a single catalytic molecule, so the detection sensitivity of the platform will limit the minimum turnover rate of the catalysts we detect. A less sensitive platform may be able to detect exceptionally fast catalysts but will miss slower catalysts,

which produce less fluorescent product over the course of an incubation. *In vitro* selected DNAzymes tend to have lower turnover rates than protein enzymes, and we expect the DNA catalysts detected on this platform to produce less than one fluorescent molecule per second of incubation. In addition to increasing the optical sensitivity of the platform (i.e., detecting lower fluorophore concentrations), droplet size can be reduced to contain the fluorescent product in a smaller volume.

With these technical objectives in mind, two droplet microfluidic platforms were developed. The first used a commercial microfluidic tee for droplet generation and transparent capillary tubing for detection. The second used custom PDMS devices for droplet generation and on-chip detection. Here, platform performance metrics are compared, and preliminary library screening experiments are discussed.

2.4.1 Technical performance of the capillary-based platform

Figure 2.8A shows the size and uniformity of droplets generated on the capillary-based platform. The average droplet volume, calculated from images of the droplets in storage tubing and assuming an oblate spherocylindrical shape, was 180 pL (±10%). Droplets were stable over multi-day incubations and could be detected at a rate of at least 6 droplets per second.

To assess the sensitivity of the capillary-based platform, a series of fluorescein standard droplets were generated and detected. The fluorescein droplets also contained a negative control DNA oligonucleotide (seq832) at a concentration of 100 μM. The oligonucleotide had a stabilizing effect that improved the uniformity and stability of the droplets. Droplets containing 4 nM fluorescein had a significantly and consistently higher

fluorescence intensity than droplets containing the oligonucleotide alone (Figure 2.9A). Droplet fluorescence increased linearly with increasing fluorescein concentration, and the calculated limit of detection was 0.1 nM fluorescein (Figure 2.9B). To account for noise and variability, a fluorescence threshold of 10 nM was chosen for library screening experiments. Droplets above this threshold were considered positive (catalyst-containing), and droplets below the threshold were considered negative.

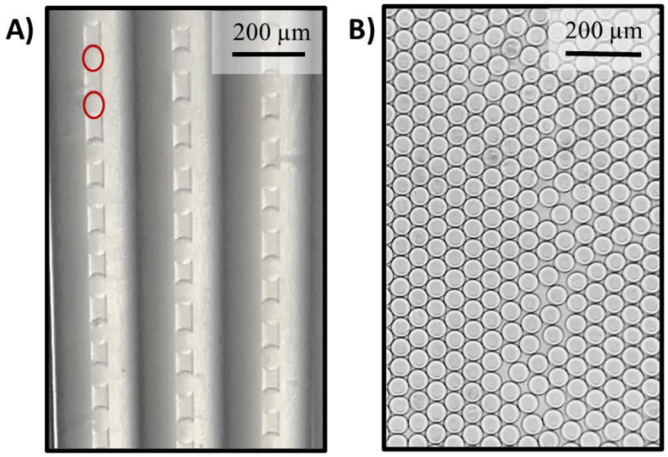

Figure 2.8*: Uniform droplets in A) incubation capillary used on the capillary-based platform (average volume 180 pL, representative drops highlighted in red) and B) a PDMS device (average volume 30 pL)*

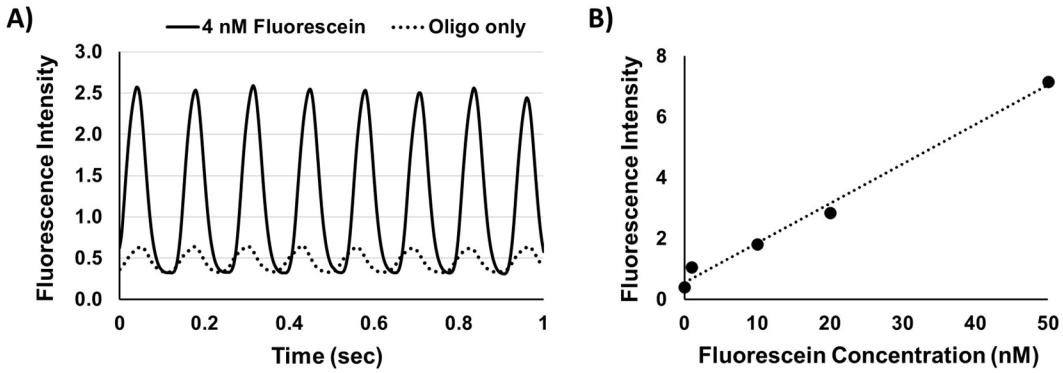

Figure 2.9*: Droplet peaks detected on the capillary-based platform. A) Overlaid plots of droplets containing 100 µM seq832 oligonucleotide (dotted line) and 100 µM seq832 oligonucleotide with 4 nM fluorescein (solid line). B) Average fluorescence intensity of droplets containing 100 µM poly T oligo and varying concentrations of fluorescein. $y = 0.1297x + 0.5613$, $R^2 = 0.9905$, LOD = 0.1 nM fluorescein.*

Table 2.2 summarizes the overall performance of the capillary-based platform in library screening experiments. The DNA library was loaded into 180 pL droplets at a concentration of 100 μM. Each droplet contained 10^{10} unique DNA sequences. With a detection rate of 6 droplets per second and a total of 6,000 droplets per run, the capillary-based platform could screen approximately 7×10^{13} sequences for catalytic activity in under 20 minutes. With slight scaling and optimization, the platform should be capable of measuring catalyst frequencies on the order of 1 per 10^{12} to 1 per 10^{14}.

***Table 2.2**: Performance summary for library-screening droplet microfluidic platforms*

	Capillary Platform	**PDMS Platform**	
Total drops per run	6,000	100,000	Adjustable parameters
Library concentration (μM)	100	50	
Incubation time (hours)	65	65	
Droplet volume (pL)	**180**	**30**	Somewhat adjustable, vary between runs
Drops detected per second	6	42	
Fluorescence threshold (nM fluorescein)	**10**	**0.5**	
Noise peaks per million drops	40	80	
Library sequences per drop	1×10^{10}	9×10^{8}	Calculated values
Library sequences per second	7×10^{10}	4×10^{10}	
Total library sequences per run	$\mathbf{7 \times 10^{13}}$	$\mathbf{9 \times 10^{13}}$	
Batch detection time (minutes)	17	40	
Minimum detectable rate (reactions sec^{-1})	**4.6**	**0.07**	
Sequences screened per noise peak	$\mathbf{3 \times 10^{14}}$	$\mathbf{1 \times 10^{13}}$	

A limiting characteristic of the capillary-based platform was its sensitivity for slow catalysts. The detection threshold used to identify positive and negative droplets was equal to the signal of 10 nM fluorescein droplets. Given the droplet volume, 10 nM is equal to approximately 10^6 fluorescein molecules per droplet. A single DNA molecule would need to catalyze one million reactions over the course of the incubation to be detectable, which

translates to a rate of 4.64 reactions per second. The capillary-based platform would therefore be sensitive enough to detect β-galactosidase, the protein enzyme that cleaves FDG (17.1 reactions per second), or an extremely fast ribozyme (16.7 reactions per second), but it would not be able to detect a typical *in vitro* selected DNAzyme (0.06 reactions per second).[53]

2.4.2 Technical performance of the PDMS device platform

The PDMS device platform was developed in response to the limitations of the capillary-based platform. Its primary goal was to detect slower catalysts, both by improving the sensitivity of the detector and by reducing the droplet volume, effectively concentrating the reaction product in a smaller space.

The photolithography techniques used to fabricate molds for PDMS devices can produce high-resolution features with very small dimensions. The droplet generation channel was 34 μm wide and 30 μm deep, smaller than the 50 μm I.D. tee and tubing used on the capillary-based platform. This scaled-down geometry reduced the volume of droplets on the PDMS device platform. Figure 2.8B shows droplets generated on the PDMS platform, which were imaged in a large chamber on a PDMS device. The average droplet volume, assuming an oblate spheroidal shape, was 30 pL, and the relative standard deviation of droplet volume after collection and reinjection was 7.5%. Droplets were uniform and could be stored off-chip in microcentrifuge tubes for several days without significant changes in volume or fluorescence.

The optical setup for on-chip droplet detection (Figure 2.10) also improved the sensitivity of the PDMS device platform compared to the capillary-based platform. Figure

2.10A shows the baseline-normalized fluorescence intensity of droplets containing 50 pM and 25 pM fluorescein. The platform was responsive to picomolar changes in fluorescein concentration, and its calculated limit of detection was 1 pM fluorescein (Figure 2.10B).

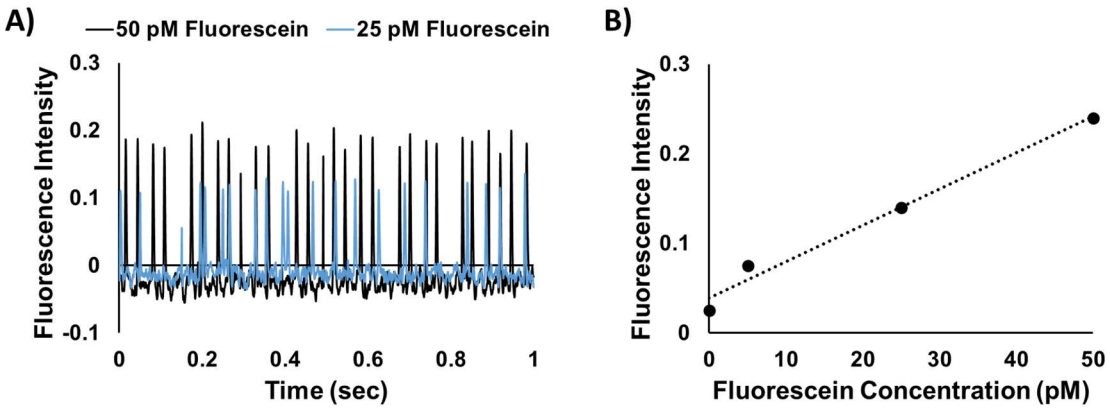

Figure 2.10*: Droplet peaks detected on the PDMS devices platform. A) Overlaid plots of baseline-normalized fluorescence from droplets containing 50 pM (black line) and 25 pM (blue line) fluorescein. B) Average fluorescence intensity of fluorescein droplets. $y = 0.004x + 0.039$, $R^2 = 0.9827$, LOD = 1 pM fluorescein.*

Table 2.2 describes the overall performance of the PDMS platform in library screening experiments. With a DNA library concentration of 50 µM inside 30 pL droplets, each droplet contained 9×10^8 DNA sequences, and 9×10^{13} (90 trillion) sequences could be screened for catalytic activity in only 40 minutes. The reduced droplet volume and improved detection sensitivity theoretically allowed the PDMS platform to detect catalysts cleaving the substrate at rates as slow as 0.07 reactions per second, assuming continuous catalytic activity over the course of a 65-hour incubation and a positive droplet threshold equivalent to 500 pM fluorescein. This sensitivity should allow the platform to detect a typical in-vitro selected DNA catalyst, which operate at rates of 0.1 to 5 reactions per minute.[53]

2.4.3 Peak identification and analysis

The droplet microfluidic approach to catalyst quantification is analytically demanding: In a single experiment, hundreds of thousands of droplets must be detected, sometimes at rates of 30-50 droplets per minute. It is necessary to accurately quantify the total number of droplets, selectively identify small changes in fluorescence intensity, and limit noise. Automated peak identification, filtering, and thresholding were therefore critical to accurate quantification.

In droplet detection experiments, a PMT continuously detected fluorescence intensity over time. Figure 2.11 shows an example of peak identification and filtering. Peaks were identified by a custom Matlab script using the findpeaks function and an automated prominence filter to separate true peaks from baseline noise. After all maxima in the data were identified, the script calculated the first minimum in the density distribution of peak prominence (Figure 2.11D). Maxima above this prominence threshold were considered peaks, and maxima below the threshold were considered baseline noise.

A set of width filters was applied to ensure that each peak represented a single droplet. Since all droplets had a uniform volume and moved past the detector at a constant rate, the distribution of peak widths was narrow and normal. Peaks with outlier widths were excluded from analysis by automated thresholding. The script determined the maximum value in the density distribution of all peak widths. To filter out the high-width tail of the distribution, a threshold was drawn at the first minimum in the distribution that occurred after the overall maximum (Figure 2.11E). Wide peaks were excluded from analysis because they typically occur as a result of droplets coalescence. Most often, coalesced

droplets will appear as a streak of consecutive, high-intensity peaks (Figure 2.11C). Narrow peaks, which can be caused by non-droplet debris, were also excluded in some experiments.

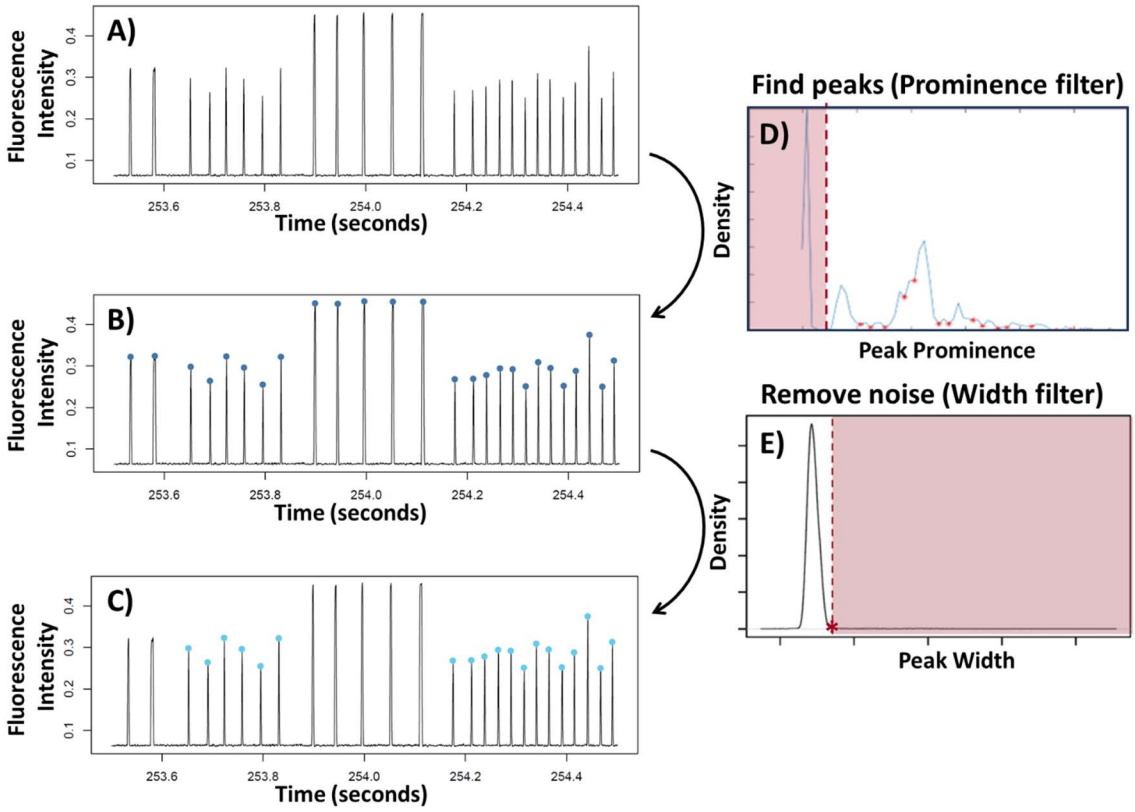

Figure 2.11*: Example of peak finding and filtering. A) Raw data. B) Dark blue points indicate identified peaks. C) Light blue points indicate peaks that represent a single droplet. Peaks from coalesced droplets and non-droplet debris are removed using width filters. D) Example of automated prominence thresholding. Minima in the peak prominence density distribution are identified. The first minimum represents the prominence threshold. Less prominent peaks are excluded. E) Example of automated width filtering. The first minimum in the peak width density distribution represents the width threshold. Wider peaks are excluded from further analysis.*

Once peaks were identified and filtered, intensity thresholding scripts were used to count "negative" (catalyst-free) and "positive" (catalyst containing) droplets. Library screening experiments on the capillary-based platform used 10 nM fluorescein droplets to set an absolute threshold. Experiments on the PDMS device platform used automated

thresholding scripts to account for experiment-to-experiment changes in the fluorescence of negative droplets and to improve the sensitivity of the platform for slower catalysts.

Manual thresholding introduces some degree of investigator bias, which is unacceptable in an application where the inclusion or exclusion of only a few points could determine experimental conclusions. Thresholding methods based on standard deviations are also inappropriate because they assume a normal distribution. The distribution of peak intensities usually tailed toward high intensities, and in fact this tail was the region of greatest statistical interest.

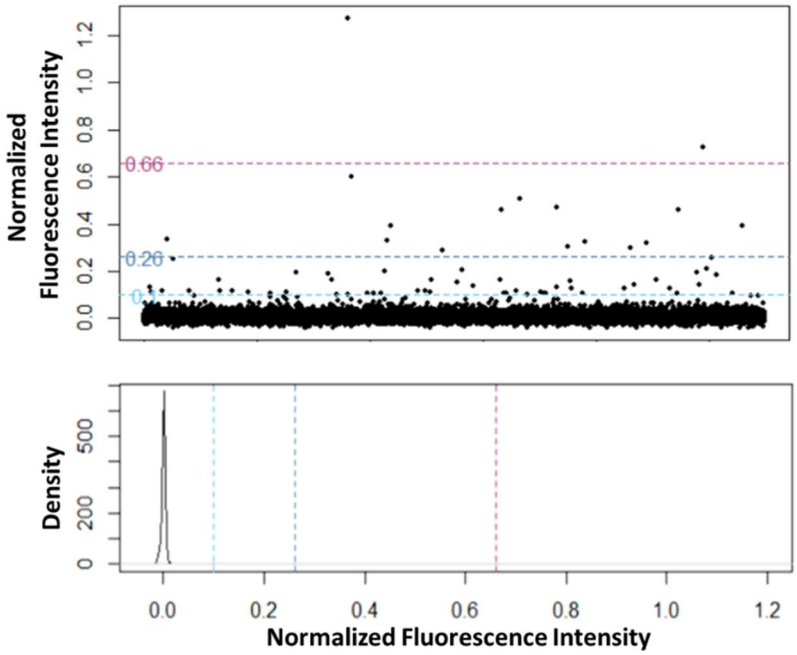

***Figure 2.12**: Normalized fluorescence intensity of approximately 550,000 negative control droplets. Each point in the dot plot (top) represents the intensity of one peak. The density plot (bottom) shows the distribution of peak intensities. Thresholds are drawn at confidence intervals of 0.95 (light blue, intensity = 0.10), 0.995 (dark blue, intensity = 0.26), and 0.9995 (purple, intensity = 0.66).*

A custom R script was adapted from the "ddpcRquant" tool developed by Trypsteen *et al.* for thresholding in droplet digital PCR experiments.[238] This automated tool uses

extreme value theory to model the distribution of peak intensities in combined negative control runs. Thresholds can be set to include a smaller or larger percentile of the modeled extreme value distribution (Figure 2.12). The frequency of positive droplets, defined as the number of peaks above the threshold per million peaks detected, was calculated for each droplet sample. To test for catalytic nucleic acid activity, the positive frequency among droplets containing a fluorescent substrate and random-sequence DNA library was compared to the positive frequency among droplets containing a non-catalytic control sequence. Replicate droplet samples were used to control for batch-to-batch variation.

2.4.4 Non-catalytic negative control

Incubation experiments required a negative control oligonucleotide that was known to be non-catalytic. Although no tools exist to predict catalytic activity based on nucleotide sequence, many tools can predict the stability of hairpin structures formed by intramolecular hydrogen bonding between nucleotides. Since three-dimensional structure is expected to be necessary for effective catalysts, oligonucleotides with minimal secondary structure are good candidates for negative controls. To design a negative control sequence with A/C/G/T content reflective of a "typical" library molecule, 999 randomly-generated N_{90} sequences were assessed for potential secondary structure using the Quikfold tool on the DINAmelt server[239] (for bulk-entry analysis of all sequences) and Integrated DNA Technologies' OligoAnalyzer tool[240] (for individual analysis of select sequences). The sequence with the weakest predicted secondary structure was identified, and the 30-nucleotide region of this sequence most prone to intramolecular hydrogen bonding was randomized (Figure 2.13). The resulting second-round sequences were assessed again

using Quickfold and OligoAnalyzer. An improved sequence, named seq832, was chosen as a negative control.

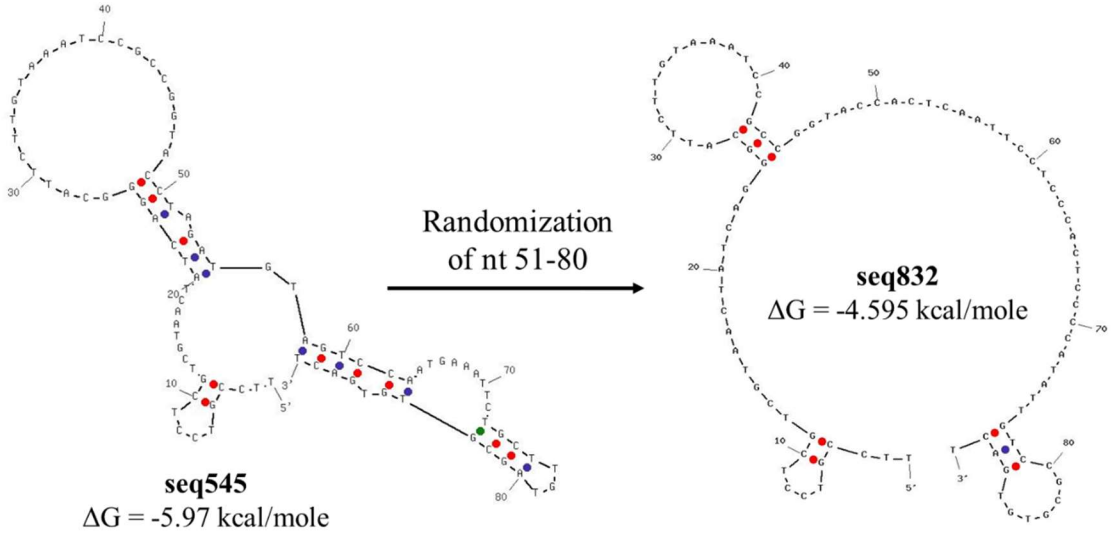

***Figure 2.13**: OligoAnalyzer-predicted folding of randomly generated sequence (left) and the weaker predicted folding of the sequence after randomization of 30 nucleotides most prone to hydrogen bonding. Red dots indicate a G-C base pair, purple dots indicate an A-T base pair, and green dots indicate a predicted non-canonical base pairing.*

2.4.5 Library screening: Substrates

The capillary-based and PDMS device platforms were both used to screen 90-nucleotide, random-sequence DNA libraries for catalytic cleavage of fluorogenic substrates. The initial substrate chosen was FDG, a widely-used indicator for the protein enzyme β-galactosidase. FDG is a di-substituted fluorescein analogue that is first hydrolyzed to a low-fluorescence intermediate (FMG) before being hydrolyzed again to highly fluorescent fluorescein (Figure 2.14). Subsequent experiments used FMG as a substrate, which reduces the mechanistic complexity of the screening reaction. However, FMG's higher background fluorescence means that DNA catalysts would need a slightly higher turnover rate to produce a detectable increase in droplet fluorescence.

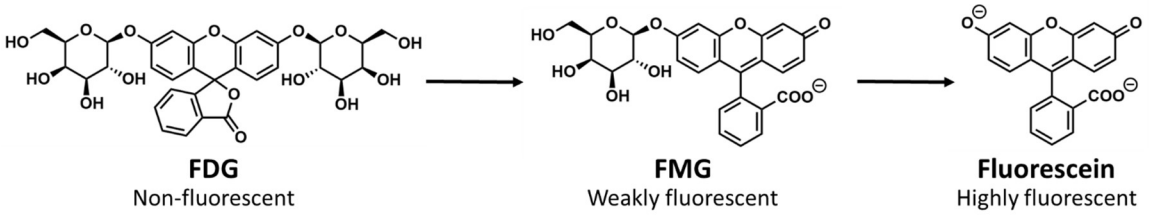

***Figure 2.14**: Fluorogenic substrates. Fluorescein di-β-D galactopyrianoside (FDG) is hydrolyzed to fluorescein mono-β-D galactopyrianoside (FMG), which is hydrolyzed to fluorescein.*

Since DNA catalyst selection has historically relied on intramolecular reaction designs, many of the fastest and best-characterized DNA catalysts cleave or otherwise modify DNA and RNA. Meanwhile, there is no documented precedent for DNA-catalyzed cleavage of FDG or FMG. To address the possibility that sugar-cleaving DNA catalysts simply do not exist, a third fluorogenic substrate was designed based on a published application of the well-characterized, RNA-cleaving 10-23 DNAzyme.[241] This custom oligonucleotide contained two RNA bases flanked by DNA arms. It was labelled with FAM its 5' end and Iowa Black dark quencher on its 3' end (Figure 2.15). FAM's fluorescence is quenched by Iowa Black in the intact substrate, but hydrolysis at the RNA bases (or any other site along the molecule) will free the fluorophore from the quencher and dramatically increase the fluorescence of the system.

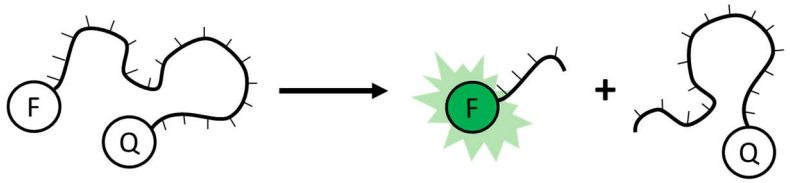

***Figure 2.15**: RNA substrate labeled with FAM (F) and Iowa Black quencher (Q) becomes fluorescent when cleaved.*

2.4.6 Library screening: Capillary-based platform

Library and control droplets were detected on the capillary-based platform before and after a 65-hour incubation at 37°C. Figure 2.16 shows the intensity of each droplet

detected, as well as the frequency of positive droplets among library and negative control droplets. Each point on the plot represents the fluorescence intensity of one droplet, and each panel represents one detection run. Approximately 6,000 droplets were detected per run.

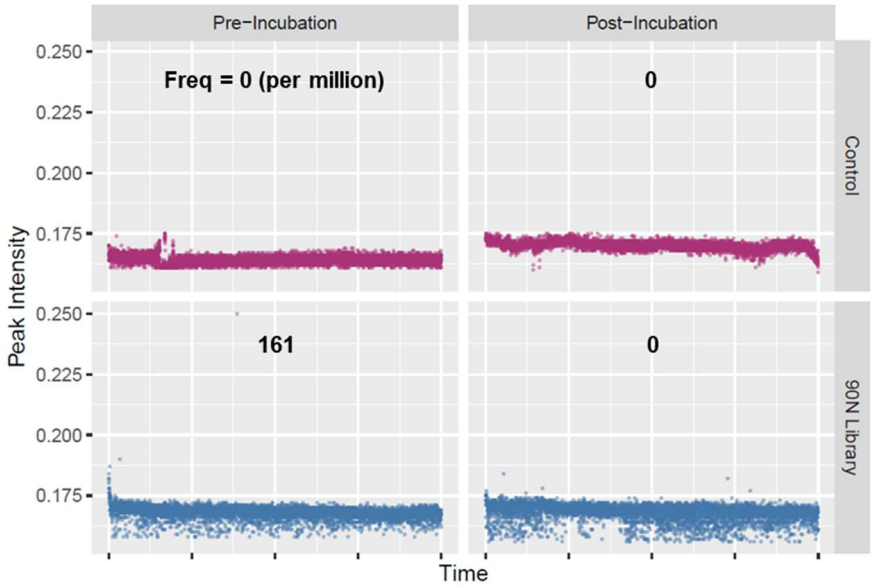

Figure 2.16*: 3-day incubation of 90N library or negative control oligonucleotide with FDG at 37 °C. Droplets were generated and detected on the capillary-based platform. The frequency of positive droplets per million droplets detected is listed for each run. Each point represents the fluorescence of one droplet. ~6,000 droplets per panel. With no positive droplets after incubation, there was no evidence of catalysis.*

Droplets containing the non-catalytic negative control sequence (top panels, plotted in purple) had a uniformly low-intensity "negative" signal before and after incubation because they did not contain a library of possible catalysts to interact with the substrate. Library droplets detected before incubation (bottom left panel, plotted in blue) were also expected to be negative because a single catalytic DNA molecule would not be fast enough to produce a detectable amount of product in the short time between droplet generation and initial detection.

If the DNA library contains sequences that catalyze FDG cleavage, we expect to see an increase in the frequency of positive droplets after incubation. For example, given the number of unique DNA sequences in each droplet (Table 2.2), a positive droplet frequency of 10 in 6,000 droplets would correspond to a catalyst abundance of 1 catalyst for every 2 trillion sequences screened.

Across all four droplet detection runs, only one "positive" droplet exceeded the fluorescence threshold. The single positive droplet in the pre-incubation library run is better explained by noise than catalysis. Since there was no increase in the frequency of positive droplets after library incubation, there was no evidence of DNA-catalyzed cleavage of FDG.

2.4.7 Library screening: PDMS device platform

Using the PDMS device platform, the 90-nucleotide DNA library was screened for catalytic activity in droplets with all three fluorogenic substrates: FDG, FMA, and the RNA substrate. Library screening in PDMS devices used an automated thresholding script to identify positive and negative droplets.

Figure 2.17 shows the results of a 2-day incubation of the 90-nucleotide DNA library with FDG. Although the intensity of some droplets exceeded the calculated threshold, The frequency of positive library-containing droplets (top panels) was higher before incubation than after incubation at either 21°C or 37°C. There was a similar positive frequency among droplets that contained the non-catalytic control sequence, indicating that positive droplets in this experiment were better explained by random noise than by catalytic activity.

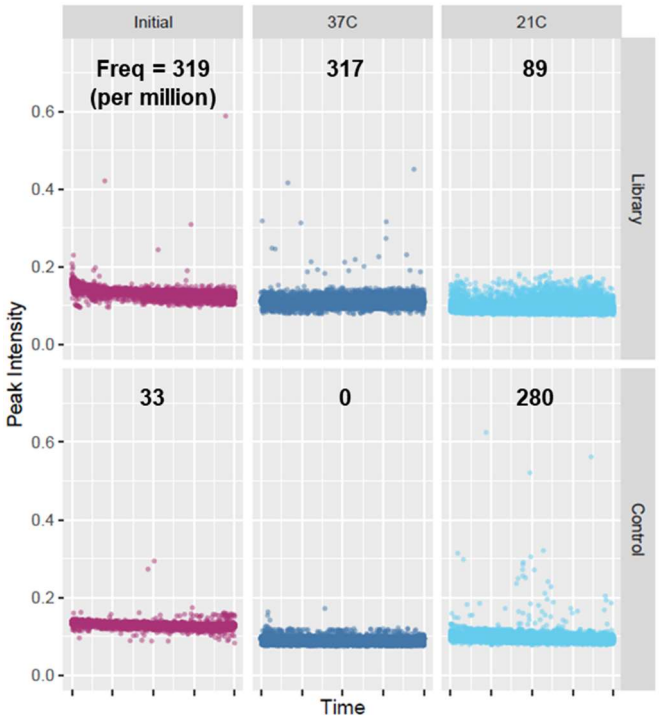

Figure 2.17*: 2-day incubation of 90N library or negative control oligonucleotide with FDG at 37 °C and 21 °C. Droplets were generated and detected in PDMS devices. The frequency of positive droplets per million droplets detected is listed for each run. Each point represents the fluorescence of one droplet. ~100,000 droplets per panel.*

A subsequent library screening experiment used FMG as a substrate in an effort to simplify the reaction of interest and increase catalyst frequency. Figure 2.18 shows the results of a 3-day incubation of the 90-nucleotide DNA library with FMG. This experiment gave an example of batch-to-batch variability in the frequency of high-intensity droplets. Although one batch of library-containing droplets incubated for 48 hours and one batch incubated for 72 hours showed high frequencies of positive droplets, replicate batches under the same conditions were consistent with pre-incubation controls and negative controls. High positive frequencies in the two library batches are better explained by noise – caused by contamination, debris, detection misalignment, or other factors – than by catalysis.

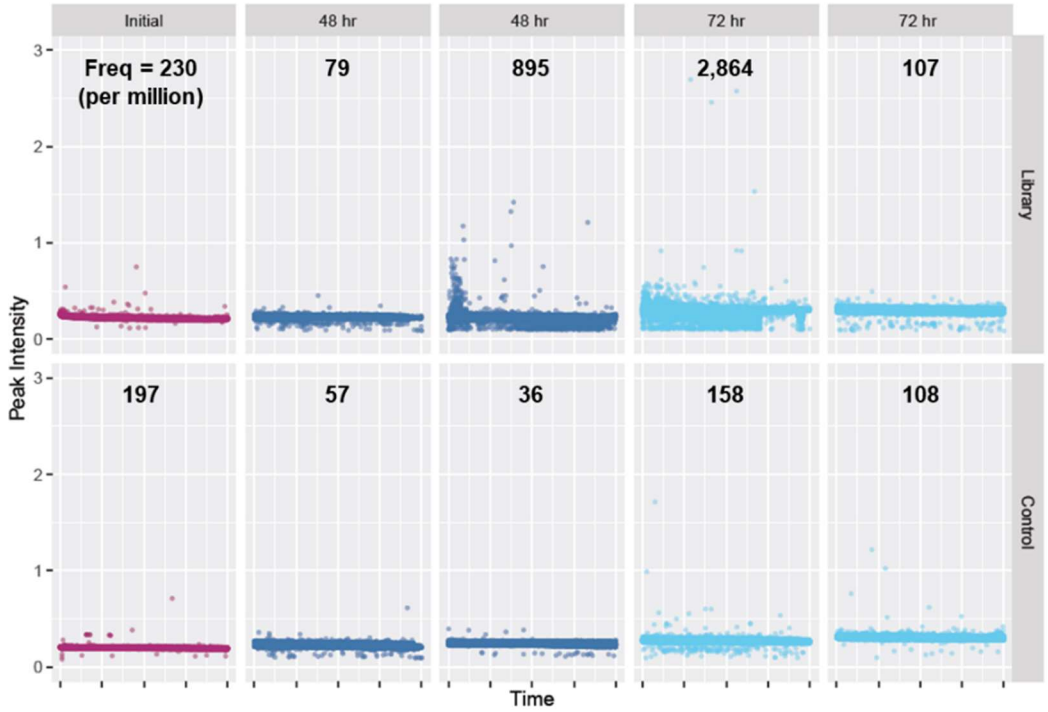

***Figure 2.18**: 2-day and 3-day incubation of 90N library or negative control oligonucleotide with FMG at 21 °C. Droplets were generated and detected in PDMS devices. The frequency of positive droplets per million droplets detected is listed for each run. Each point represents the fluorescence of one droplet. ~100,000 droplets per panel. Although there is high-intensity noise in some library runs, the overall results are not consistent with catalysis.*

In other experiments, pre-incubation controls and negative controls also occasionally showed high frequencies of high-intensity droplets (Figure 2.19). These results underscore the importance of controls, replication, and noise reduction in library screening experiments, since conclusions regarding catalytic activity will rely on careful measurement of rare phenomena.

Figure 2.20 shows the results of a two-day incubation of the 90-nucleotide DNA library with the custom RNA substrate. The frequency of positive droplets was uniformly low among both library and negative control droplets, before and after incubation. There was no evidence of DNA-catalyzed cleavage of the RNA substrate.

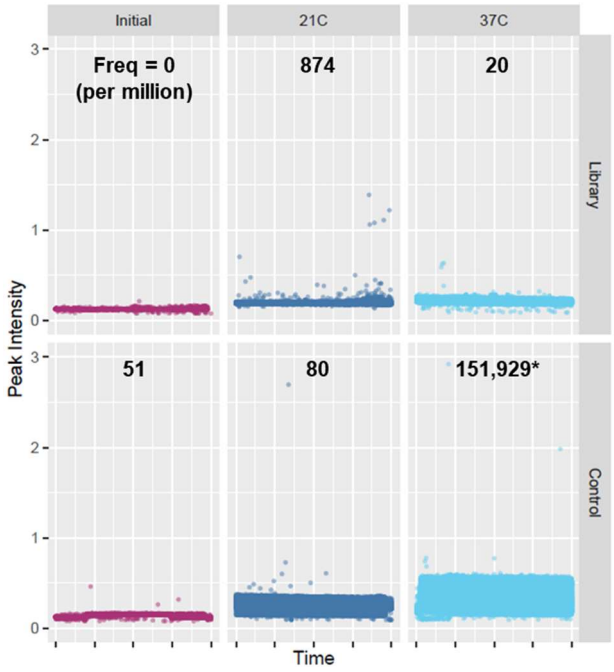

***Figure 2.19**: 2-day incubation of 90N library or a negative control oligonucleotide with FMG at 21 °C and 37 °C. Droplets were generated and detected in PDMS devices. The frequency of positive droplets per million droplets detected is listed for each run. Each point represents the fluorescence of one droplet. ~100,000 droplets per panel. High-intensity noise is present in negative controls droplets after incubation at 37 °C.*

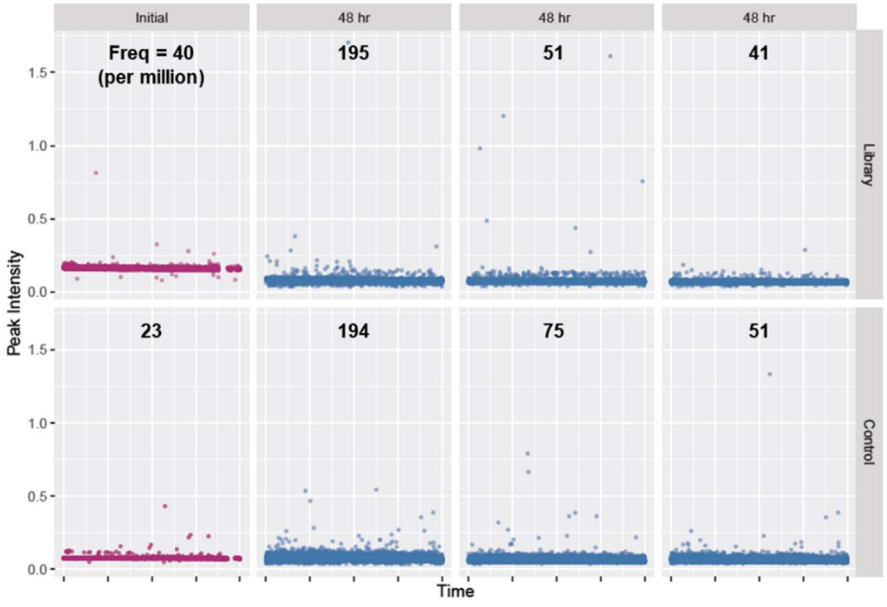

***Figure 2.20**: 2-day incubation of 90N library or negative control oligonucleotide with RNA substrate at 37 °C. Droplets were generated and detected in PDMS devices. The frequency of positive droplets per million droplets detected is listed for each run. Each point represents the fluorescence of one droplet. ~100,000 droplets per panel.*

2.4.8 Remaining limitations of the PDMS device platform

The PDMS device platform was capable of screening approximately 9×10^{13} library sequences in a single run (Table 2.2). This library size could be expanded by increasing either the concentration of the DNA library or the number of droplets screened, changes that are feasible within a few orders of magnitude. In terms of throughput, the PDMS device platform should theoretically be capable of quantifying DNA catalyst abundance on the order of one in 10^{13} to one in 10^{15}. Although the abundance of nucleic acid catalysts is still unknown, the success of *in vitro* selection procedures, which begin with libraries on the order of 10^{12} to 10^{16} sequences, is a promising indicator that this microfluidic platform is within range.[1]

However, as the throughput of the platform increases and the frequency of catalyst-containing droplets decreases, a new technical limitation arises. Among nearly all batches of blank and negative control droplets, a handful of high-intensity droplets were detected. Particulates like dust, debris, precipitates, or biological contaminants can cause high-intensity signal spikes that are falsely registered as positive droplets. If the catalyst frequency is extremely low, the frequency of false-positive noise peaks will begin to limit catalyst detection. For every million droplets detected on the PDMS device platform, there were approximately 80 high-fluorescence noise peaks. That equates to approximately one noise peak for every 10^{13} (ten trillion!) library sequences screened. But because catalytic sequences are expected to be extremely rare, the tolerance of the platform for noise is exceptionally low. The current PDMS device platform is statistically unable to differentiate catalysts frequencies below 1×10^{-13} from the noise inherent in droplet detection.

2.5 Conclusion

Two droplet microfluidic platforms were constructed to screen libraries of random-sequence DNA for catalytic activity in the presence of a fluorogenic substrate. The capillary-based platform was limited by large droplet volumes. A catalyst in the 180 pL droplets would need to have very high turnover to produce a detectable concentration of fluorescent product. Theoretically, the slowest detectable catalyst on the capillary-based platform would act at a rate of 4.6 reactions per second, a realistic catalytic efficiency for naturally-occurring protein or RNA catalysts, but significantly faster than any known DNA catalyst.

A second microfluidic platform was designed to overcome the limitations of the initial system by generating and detecting droplets in PDMS devices. The platform's reduced droplet volume and increased detection sensitivity significantly improved overall sensitivity to slow catalysts. The slowest detectable catalyst on the PDMS platform would act at a rate of 0.07 reactions per second and could theoretically detect most DNA catalysts identified through *in vitro* selection. The experiments described here screened libraries containing nearly 10^{14} sequences, and the platform could be scaled up to screen libraries of 10^{15} or even 10^{16} sequences. With high sensitivity and throughput achieved, the current limitation of the PDMS device platform is noise. False positive peaks, though rare, make it challenging to quantify extremely low catalyst frequencies. The current platform would be most appropriate for screening libraries with catalyst frequencies of at least one catalyst per trillion (10^{12}) sequences.

Library screening experiments with FDG, FMG, and a fluorogenic RNA substrate did not reveal any statistically significant evidence of catalytic activity. There are several possible explanations for these results. First, it is possible that catalysts are rarer than 1 per trillion and that the noise inherent in droplet microfluidics will overwhelm any infrequent catalyst signals. In future experiments, larger droplets or droplet-free microwell arrays might reduce the frequency of noise per molecule screened.

Second, it is possible that DNA catalysts are not efficient enough to generate the concentrations of fluorescent product required for detection. All known DNA catalysts have been identified through *in vitro* selection processes. These catalysts may represent a very small fraction of all catalytic sequences and may be at the highest end of possible DNA catalyst performance. Droplet-based, single molecule detection places high demands on catalysts because they must have high turnover rates and also perform many repeated catalytic cycles without damage. In future experiments, smaller droplets could better confine the limited product of lower efficiency catalysts.

A third explanation for the lack of demonstrated catalysis is that the reactions and conditions chosen so far for library screening experiments are not ideal for DNA catalysis. Most known catalysts have binding arms as a result of the selection processes used to identify them. The entirely randomized design of the DNA libraries used here require catalysts to both bind and cleave the substrate. There are no examples of FDG or FMG cleavage by DNA. The preferred reaction conditions are unknown. Future screening experiments could explore different library designs, substrates, and reaction conditions.

A fourth explanation is that fast catalysts for these reactions do exist in sufficiently high abundance, but the droplet environment inhibits their activity. This possibility is explored in more detail in Chapter 3.

Chapter 3: DNA-catalyzed RNA cleavage in small scale and single-molecule reactions

3.1 Summary

Chapter 2 describes a droplet microfluidic platform for the quantification of catalytic nucleic acids. PDMS devices achieved the throughput and sensitivity theoretically required to detect single DNA catalyst molecules in picoliter-scale droplets. However, library screening experiments did not demonstrate any evidence of catalysis. In this chapter, an RNA substrate and known DNA catalyst (DNAzyme) sequence were used in proof-of-concept reactions to investigate the platform's capacity for single molecule detection. The DNAzyme's catalytic activity in low-volume, bulk reactions was consistent with literature values. In bulk reactions with excess substrate, fluorescence increased steadily over the course of a 20-hour incubation, demonstrating that DNAzymes are capable of multiple-turnover RNA cleavage. However, the DNAzyme did not appear to catalyze RNA substrate cleavage over time in droplets. When the DNAzyme was loaded at low concentrations in droplets with excess substrate, there was a small, immediate increase in fluorescence, but there was no additional increase in fluorescence over the course of multi-hour incubations. Single DNAzyme molecules did not produce enough fluorescent product to distinguish catalyst-containing droplets from catalyst-free droplets. Moving forward, it will be necessary to develop new technical approaches to single molecule detection of catalytic oligonucleotides.

3.2 Introduction

Nucleic acid catalysts are an appealing alternative to protein enzymes in therapeutic and biosensing applications.[4,242,243] Identified through *in vitro* selection, these DNA, RNA, or XNA molecules can bind to a target of interest and catalyze useful bond-breaking or

bond-forming reactions. Chapter 2 describes a droplet microfluidic platform designed to answer fundamental questions about the abundance and scope of catalytic nucleic acids. On this platform, a library of random-sequence DNA was encapsulated in low-volume droplets with a fluorogenic substrate. Droplets were incubated for up to 72 hours and detected using laser-induced fluorescence (LIF). A sufficiently active catalyst should cleave the substrate, increasing the fluorescence of the droplet. We aimed to determine the frequency of highly catalytic sequences in the library by measuring the number of fluorescent droplets after incubation. This unique approach could reveal patterns in the catalytic activity of nucleic acids before any selective pressures have been applied.

The oligonucleotide library screening experiments described in Chapter 2 found no evidence of catalytic activity across several incubation conditions and fluorogenic substrates. This finding may reflect a low abundance of catalysts in the libraries – information that would be valuable in establishing a quantitative "upper limit" of catalyst abundance. However, it could also reflect technical limitations in the droplet platform itself. To draw meaningful conclusions from the results of our library screening experiments, we must thoroughly evaluate the suitability of the droplet platform for oligonucleotide catalyst detection.

Water-in-oil droplets are a popular tool for the detection,[244] quantification,[141,245] and characterization[140,142] of individual enzyme or catalyst molecules. They are often used in conjunction with chromogenic or fluorogenic substrates, which provide dramatic signal amplification because a single catalytic molecule can produce millions of copies of the product.[130,135] Droplets act as picoliter- to femtoliter-scale reactors, isolating catalysts in

single-molecule environments and confining their product in a very small volume. This confinement increases product concentration and improves detection sensitivity. In droplet-based single catalyst analysis experiments, detection is limited by the turnover of the catalyst (moles of product), the confinement provided by the droplet (volume), and the optical sensitivity of the detector (concentration LOD).

Although droplet microfluidics have been successfully applied to protein enzyme characterization,[87,140–142] there are few examples of DNA catalyst (DNAzyme) activity in droplets. DNAzymes are commonly applied to biosensor technologies, and a handful of DNAzyme-based biosensors for bacterial[123,124] and viral[125] targets have been developed on droplet microfluidic platforms. These techniques detect a single target molecule, but the DNAzyme itself – which is used as a detection and signal amplification agent – is present at relatively high concentrations. Droplet digital platforms also exist for the quantification of non-catalytic nucleic acids. For example, droplet digital PCR (ddPCR) is a commercially successful quantification method that amplifies target DNA or RNA encapsulated at single-copy concentrations in droplets.[246] However, these systems use protein enzymes for amplification.

To our knowledge, microfluidic approaches have not been used to detect single copies of DNAzymes in droplets. A handful of non-droplet approaches have been used to monitor single DNAzyme molecules to better understand their catalytic mechanisms. These single-molecule approaches include fluorescence resonance energy transfer (FRET),[144,145,247] atomic force microscopy (AFM),[146] and solid-state nanopores.[147] Existing studies have not used fluorogenic substrates for signal amplification.

The 10-23 DNAzyme is an RNA-cleaving DNA sequence identified through *in vitro* selection by Santoro and Joyce in 1997.[34] It consists of a 15-nucleotide catalytic core sequence flanked by binding arms, which can be designed to target specific sequences of interest (Figure 3.1). Since its discovery, the core sequence has been well characterized and broadly applied in techniques including microbial detection,[248] real-time PCR reporting,[249] and mutation detection.[250] It is a tool of interest for therapeutic applications targeting disease-associated messenger or non-coding RNA,[4] and it has been used to inhibit or interfere with viruses like HIV.[67,251]

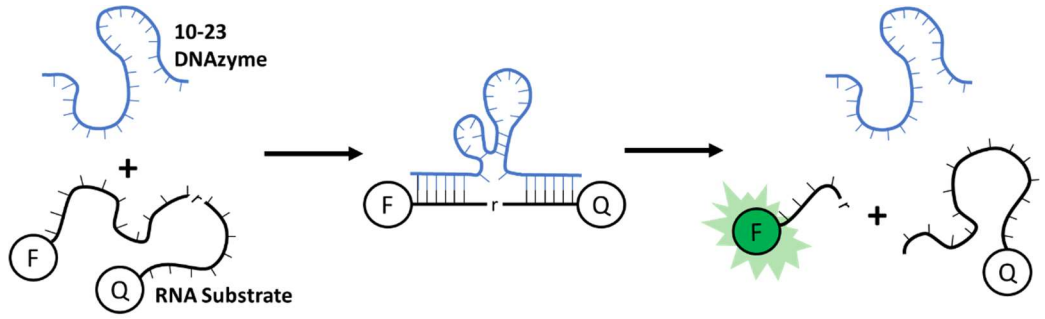

Figure 3.1*: Example of 10-23 DNAzyme-catalyzed RNA cleavage. Complementary binding arms on the DNAzyme hybridize to an oligonucleotide substrate containing an RNA base (r), a fluorophore (F), and a quencher (Q). The catalytic core cleaves the substrate, freeing the fluorophore from the quencher. Fluorescence increases after catalytic cleavage of the substrate.*

DNAzyme kinetics depend strongly on reaction design and conditions. Turnover rates are sensitive to changes in pH and metal ion cofactor concentration. The Michaelis constant, K_M, is sensitive to changes in the length and sequence of the binding arms.[34,252] Ven et al. optimized the hybridization arms of a 10-23 DNAzyme for use in room-temperature RNA cleavage reactions.[241] Here, the room-temperature 10-23 DNAzyme is incorporated into small volume and droplet reactions with a fluorogenic RNA substrate to assess the feasibility and limitations of single DNAzyme molecule detection on a droplet microfluidic platform.

3.3 Experimental

3.3.1 Chemicals and reagents

All solutions were made using deionized water (18.3 MΩ, Milli-Q; Millipore, Bedford, MA). Chemicals were obtained from Sigma-Aldrich (St. Louis, MO) unless otherwise specified. DNAzyme reactions were incubated in 5 mM Tris buffer (pH 7.5) with 50 mM KCl and 20 mM $MgCl_2$. Droplets were generated and stored in Bio-Rad (Hercules, CA) ddPCR Droplet Generation Oil for EvaGreen. DNA and RNA oligonucleotides (Table 3.1) were synthesized by IDT (Coralville, IA), resuspended in nuclease-free water (IDT), and stored in aliquots at -20°C.

***Table 3.1**: Oligonucleotide sequences*

	Sequence (5' → 3')
DNAzyme	TGG TGA GGC TAG CTA CAA CGA GGT TGT
RNA Substrate	/56- FAM/ACA ACC rGrUC ACC A/3IABkFQ/
Negative Control (Seq-832)	TTC CGT CCT CGT CGT AAC TAT CAG GGC ATT CTT GTA AAT CCG CCG GTA CCA CTC AAT TCC TCC CAC TCC CCA TAT TGT CCG CGT GTG ACT
Binding Control 1	TGG TGC AAG GGA GTT TCA AGG GGT TGT
Binding Control 2	TGG TGC TGT CTT GGT CGC GGG GGT TGT

3.3.2 Bulk reactions

The DNAzyme and RNA substrate were incubated in small-volume bulk reactions in a 384-well plate and detected on a BioTek (Winooski, VT) Synergy 2 plate reader. For kinetic characterization, 1 nM DNAzyme was incubated with 10 to 400 nM RNA substrate in 25 µL reactions. Reaction fluorescence (excitation 485/20 nm; emission 528/20 nm) was recorded in 20- second increments after the addition of the DNAzyme, and the initial rate of fluorescence increase was calculated over the first 5 minutes of the reaction.

For endpoint determination, reaction fluorescence was recorded in 5-minute increments over the course of many hours. 1 nM DNAzyme was incubated with 50-250 nM RNA substrate in 25 μL reactions and detected for 9 hours. For long incubation turnover calculations, 250 nM RNA substrate was incubated with 50-500 pM DNAzyme for 20 hours.

3.3.3 PDMS device fabrication

PDMS devices for droplet generation and detection were fabricated using standard photolithography techniques.[237] Photolithography was performed in the Minnesota Nano Center. Briefly, silicon wafers were coated with SU-8 2025 photoresist (Kayaku, Westborough, MA), pre-baked, and aligned with a photomask of the device features (Fineline Imaging, Colorado Springs, CO). The pattern was transferred to the photoresist by UV light exposure. The exposed wafer was baked and then immersed in propylene glycol monomethyl ether acetate to remove unreacted photoresist. The master mold was tempered at 150 °C, and features were silanized by vapor exposure with trichloro-perfluorooctanyl silane. Device designs are shown in Figure 3.2.

3.3.4 Droplet generation and detection

In initial experiments, droplets were generated in a device with a single aqueous inlet (Figure 3.2A), which required mixing of the substrate and catalyst prior to droplet generation. In this device, the oil and aqueous phases were loaded into gastight syringes on a syringe pump. Syringes were connected to the PDMS device using PTFE tubing (O.D. 1 mm, I.D. 0.022 in., McMaster-Carr, Elmhurst, IL), and both phases were introduced at a rate of 180 μL/hour. Droplets exited the device through a short piece of PTFE tubing and

were collected in excess oil in a microcentrifuge tube, where they could be stably incubated for up to a week at room temperature.

For experiments where incubation time was a greater concern, droplets were generated in a device with two aqueous inlets (Figure 3.2B). In this device, the substrate and DNAzyme were introduced through separate inlets and met on the device immediately before emulsification. The oil phase was flowed at 180 µL/hour, the substrate and DNAzyme solutions were flowed from a separate pump at 90 µL/hour each.

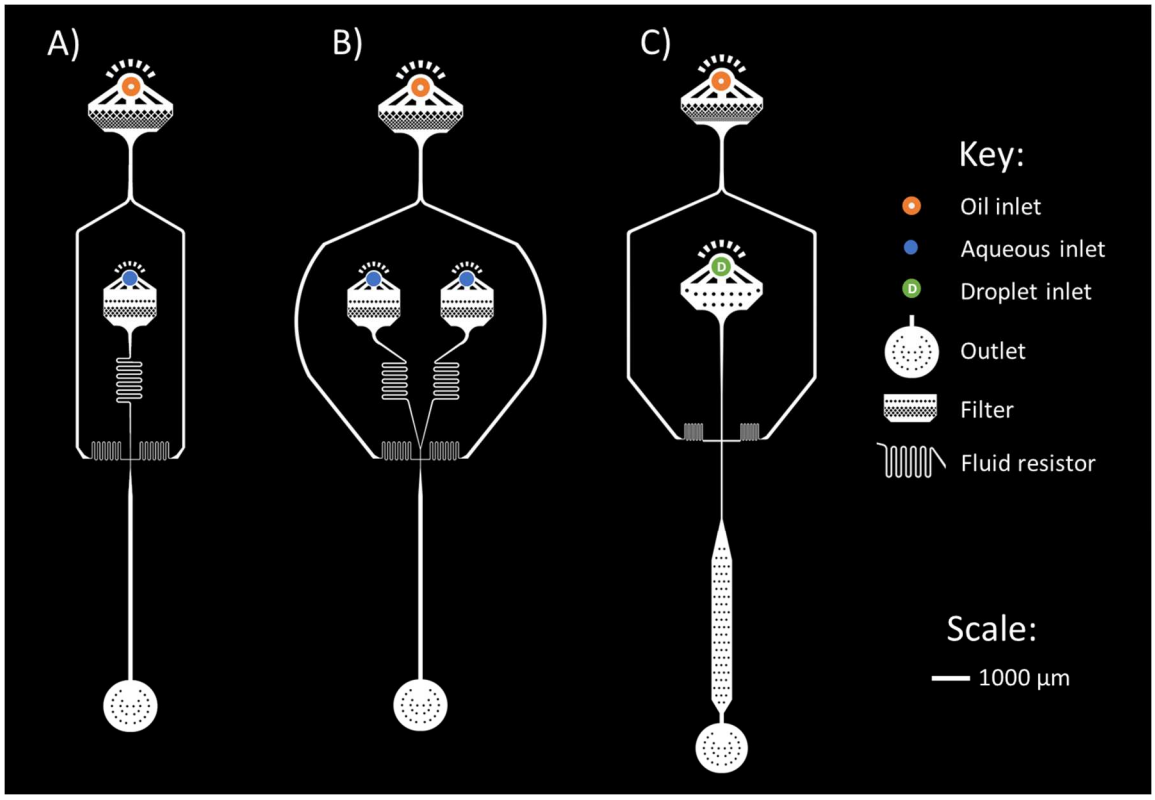

***Figure 3.2**: Photomask designs for single aqueous inlet droplet generation device (A), double aqueous inlet droplet generation device (B), and droplet detection device (C).*

A third device (Figure 3.2C) was used for droplet detection. Incubated droplets were reinjected onto the device from a gastight syringe positioned upright on a syringe pump to prevent injection of excess oil. Droplets entered the device at 10 µL/hour and were

spaced by a 100 μL/hour flow of HFE-7500 oil (Oakwood, Estill, SC). As the spaced droplets flowed single-file through a detection channel, their fluorescence intensity was read by a custom epifluorescence system. A 488 nm laser (Sapphire 488-50, Coherent, Santa Clara, CA) was focused using a 506 nm longpass dichroic mirror (Edmund Optics, Barrington, NJ) and a 20× A-plan objective (Zeiss, Jena, Germany). Fluorescent signal was collected by a 1× Zeiss tube lens and filtered through a 520 nm bandpass filter (Intor, Socorro, NM) and 488 nm notch filter (Edmund Optics) before detection by a PMT (Hammamatsu, Shizuoka, Japan).

3.3.5 Data analysis and filtering

The fluorescence intensity reported for both plate reader and droplet experiments was normalized using wells or droplets containing a fluorescein standard to improve quantitative comparisons across multi-well, multi-batch, or multi-day experiments. Custom Matlab scripts were used to identify peaks in the data collected by the PMT. Peaks were filtered by prominence to remove baseline noise and then filtered by width to remove narrow spikes caused by debris and wide peaks caused by coalesced droplets.

3.4 Results and Discussion

3.4.1 Characterization of an RNA-cleaving DNAzyme in bulk reactions

DNAzyme-catalyzed cleavage of the fluorogenic RNA substrate was monitored by fluorescence detection of 25 μL reactions in a 384-well plate. The aim of these bulk reactions was to confirm that DNAzyme-catalyzed RNA cleavage occurs under the multiple turnover conditions that would ultimately be necessary to detect catalysts in droplets. Limitations in the catalytic efficiency or lifetime of DNAzyme molecules (i.e.,

the total number of reactions performed before inactivation) would restrict the total amount of product generated during long incubations and would likely prohibit the detection of single DNAzyme molecules in droplets. More complete kinetic and mechanistic characterizations have been performed elsewhere.[34,252–254]

Figure 3.3 shows the initial rate of reactions containing 1 nM DNAzyme and 10 to 400 nM RNA substrate. Because of the relatively large volume of the well plate reactions, each well contained approximately 1.5×10^{10} DNAzyme molecules. The initial rates of the reaction were fit to the Michaelis-Menton equation: $v = k_{cat}$ [E]/(K_M + [S]), giving a K_M of 170 ± 30 nM and k_{cat} of 3.43 reactions per minute. There was no significant increase in fluorescence for control reactions without the DNAzyme. These kinetic parameters are consistent with previous characterizations of the 10-23 catalytic core sequence, confirming that DNA-catalyzed RNA cleavage is occurring in the well plate reactions.[34,252]

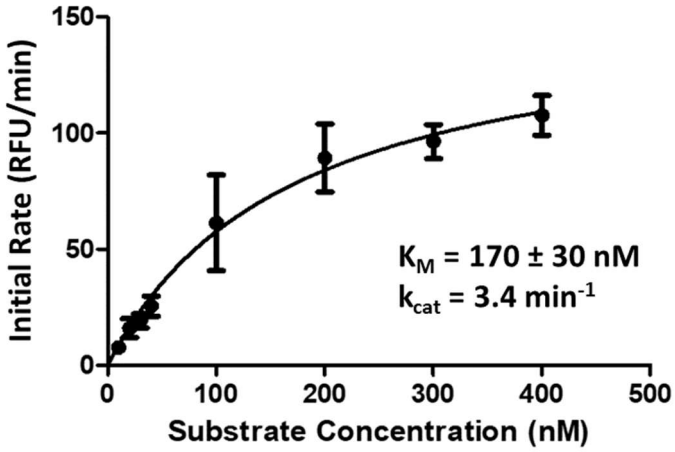

Figure 3.3*: Initial rates of reactions containing 1 nM DNAzyme*

To detect the activity of 10-23 DNAzymes in droplets with a single catalyst molecule, each individual DNAzyme must perform many cleavage reactions, producing a detectable amount of fluorescent product. We can begin to assess the lifetime of the catalyst

in bulk reactions before moving to droplets. In these bulk reactions, our main questions are:

1. Is the DNAzyme capable of multiple turnovers?
2. When the substrate is present in excess, does the activity of the DNAzyme continue over the course of a multi-hour incubation?

For reactions with a constant 1 nM DNAzyme and 50-250 nM RNA substrate (Figure 3.4A), the initial reaction rate increased with increasing substrate concentration. Fluorescence intensity rose for approximately 3 hours before plateauing at a constant intensity proportional to the concentration of substrate in the reaction. This demonstrates that for reactions with less than 1000-fold excess substrate, the reaction ends in substrate consumption. The lifetime of the DNAzyme did not limit product formation at these moderate concentrations.

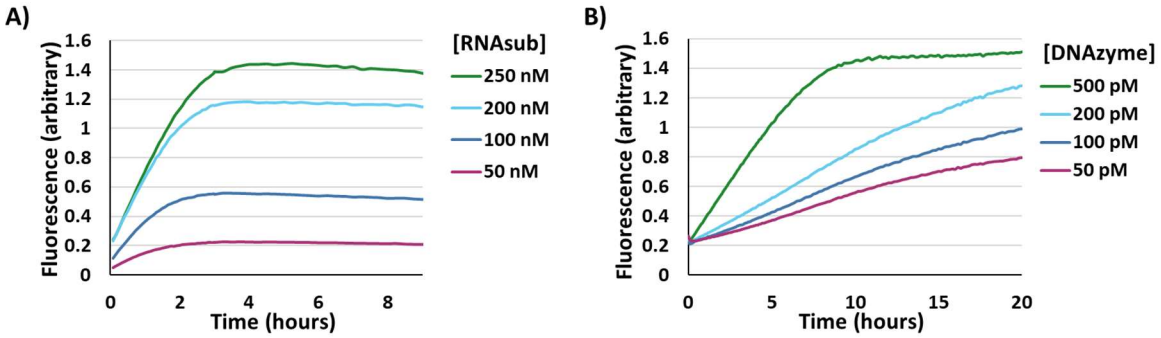

Figure 3.4*: Fluorescence intensity over time for 25 µL reactions with constant concentrations of A) 1 nM DNAzyme or B) 250 nM RNA substrate.*

For reactions with a constant 250 nM RNA substrate and 50-500 pM DNAzyme (Figure 3.4B), the initial reaction rate increased with increasing DNAzyme concentration. Fluorescence intensity plateaued only for the reaction containing the highest concentration of DNAzyme. At lower DNAzyme concentrations, fluorescence intensity continued to

increase over the course of the entire 20-hour incubation period. When the substrate was not completely consumed, DNAzyme activity continued for extended time periods. After a 20-hour incubation, the 100 pM DNAzyme reaction's fluorescence was equal to a control well containing 125 nM fluorescein. To achieve this intensity by freeing FAM from the quenched RNA substrate, the DNAzyme would need to work at an average rate of 1.04 reactions per minute per enzyme molecule, and each DNAzyme molecule would need to catalyze an average of 1,248 reactions over the course of the incubation.

In summary, the 10-23 DNAzyme catalyzed RNA cleavage in bulk reactions with relatively high turnover. At the concentrations and timescales studied here, there were no obvious limits in the number of substrate molecules a single DNAzyme could cleave.

Given the activity of the 10-23 DNAzyme in well plate reactions, single-molecule DNAzyme detection is expected to be challenging but within reach of the droplet microfluidic platform. Assuming a droplet volume of 30 pL and a fluorescence sensitivity threshold of 100 pM fluorescein, a single DNAzyme molecule in a droplet would need to perform approximately 1,800 RNA cleavage reactions to produce a detectable amount of fluorescent product. At a rate of 1.04 reactions per minute, an incubation period of less than 48 hours should be sufficient to accumulate enough product for single-molecule DNAzyme detection. When tens, hundreds, or thousands of DNAzyme molecules are incubated in a single droplet, their activity should be readily detectable.

3.4.2 High-concentration DNAzyme in droplets

Reactions involving high concentrations of both the DNAzyme and RNA substrate also produced high fluorescence in droplets. Figure 3.5 compares the fluorescence intensity

of droplets containing 250 nM RNA substrate and 250 nM DNAzyme to the intensity of control droplets containing the RNA substrate alone. Each droplet contained approximately 4.5×10^6 DNAzyme molecules. Less than an hour after droplet generation, DNAzyme droplets showed a 6-fold increase in signal over control droplets. There was no subsequent increase in the fluorescence intensity of either the DNAzyme droplets or the control droplets after 4 hours of incubation. At high concentrations, the DNAzyme appeared to quickly and completely transform the RNA substrate into its fluorescent product.

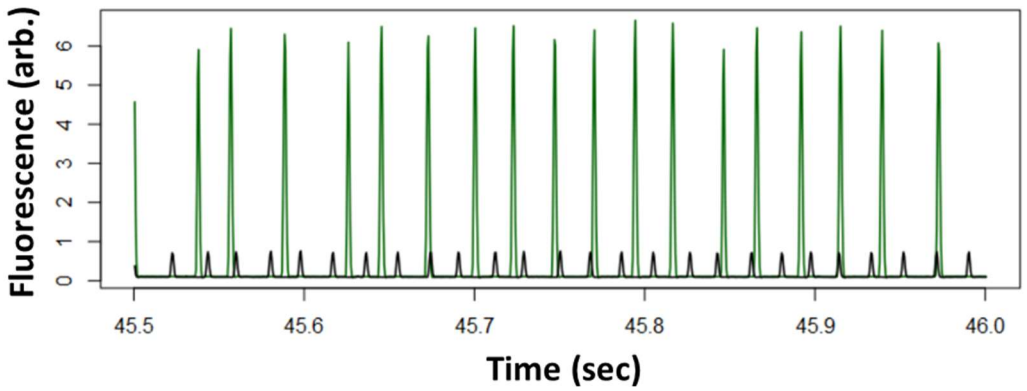

Figure 3.5*: Droplets containing 250 nM RNA substrate and 250 nM DNAzyme (green) or 250 nM RNA substrate alone (black).*

The droplets in Figure 3.5 were generated using a device with a single aqueous inlet (see Figure 3.2A). The DNAzyme and substrate were mixed immediately before droplet generation. Although the fluorescence increase shown in Figure 3.5 may reflect DNAzyme activity in droplets, it could alternatively be explained by rapid substrate cleavage before emulsification. To prevent substrate cleavage prior to emulsification, all subsequent experiments used a droplet generation device with separate aqueous inlets for the DNAzyme and RNA substrate (Figure 3.2B).

3.4.3 Low-concentration DNAzyme in droplets

Next, the concentration of the DNAzyme was decreased until the expected number of catalyst copies per droplet was close to or less than one. For 30 pL droplets, a DNAzyme concentration of 500 fM corresponds to an average of 10 catalyst molecules per droplet. A DNAzyme concentration of 5 fM corresponds to a catalyst frequency of 0.1 catalysts per droplet. In other words, only one droplet out of every 10 is expected to contain a catalytic molecule. When all droplets contain a few copies of the DNAzyme (in addition to the RNA substrate), we expect to see a small, uniform signal increase across all droplets. However, in the single molecule detection regime, we should instead see two distinct droplet populations: A majority of droplets are "negative"; they contain no catalyst and have the same signal intensity as the negative control. A smaller population of droplets are "positive", each containing a single catalytic molecule. The fluorescence of positive droplets should be higher than that of negative droplets, and if catalyst performance is robust over many turnover cycles, the intensity of the positive droplets should increase over time.

Figure 3.6 shows the fluorescence intensity of droplets containing 250 nM RNA substrate and 0, 5 fM, 500 fM, or 50 pM DNAzyme, corresponding to 0, 0.1, 10, or 1000 catalytic molecules per droplet, respectively, after 24 hours of incubation. As the concentration of DNAzyme increased, so did the average fluorescence intensity of the droplets. This could be consistent with a low but uniform number of catalytic molecules in all droplets.

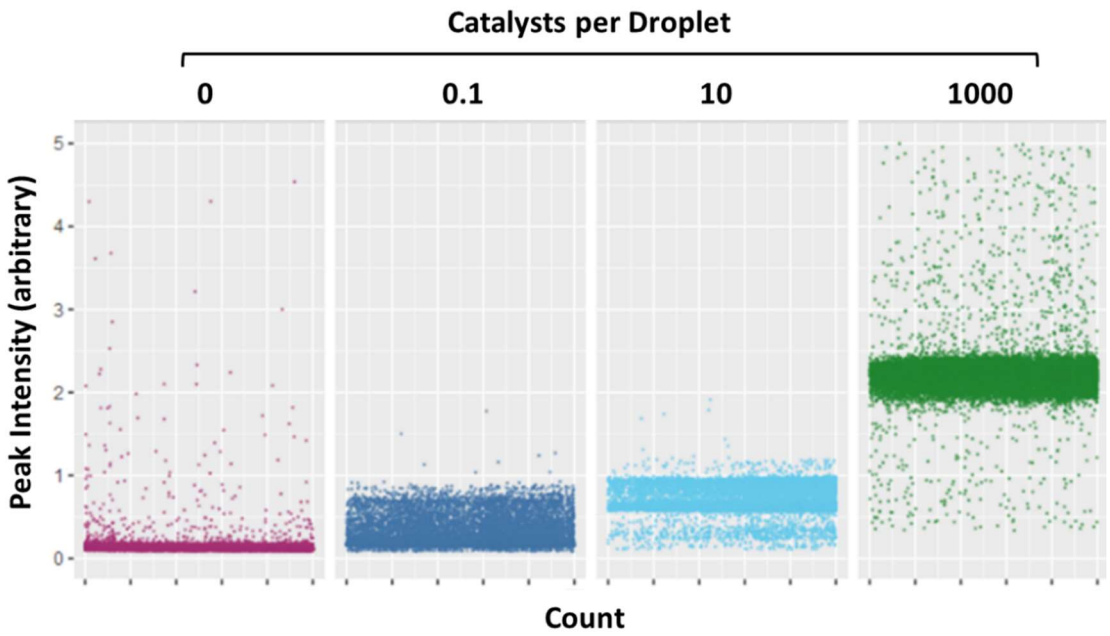

Figure 3.6*: Normalized peak intensity of droplets containing 250 nM RNA substrate and (from left to right) 0, 5 fM, 500 fM, or 50 pM DNAzyme after a 24-hour incubation at room temperature. Each point represents the fluorescence of one droplet. ~100,000 droplets per panel.*

However, Figure 3.7 shows density plots of the fluorescence intensity of 500 fM DNAzyme droplets, which were detected at multiple timepoints over the course of a 72-hour incubation. Statistically, each droplet was expected to contain approximately 10 copies of the DNAzyme. Instead of increasing as catalytic molecules cleaved more substrate, the fluorescence intensity of all droplets decreased slightly over time, likely as a result of slight fluorophore bleaching and leaching. This result is inconsistent with the turnover and lifetime of the 10-23 DNAzyme observed in bulk reactions, where DNAzyme activity continued after at least 20 hours of incubation with excess substrate.

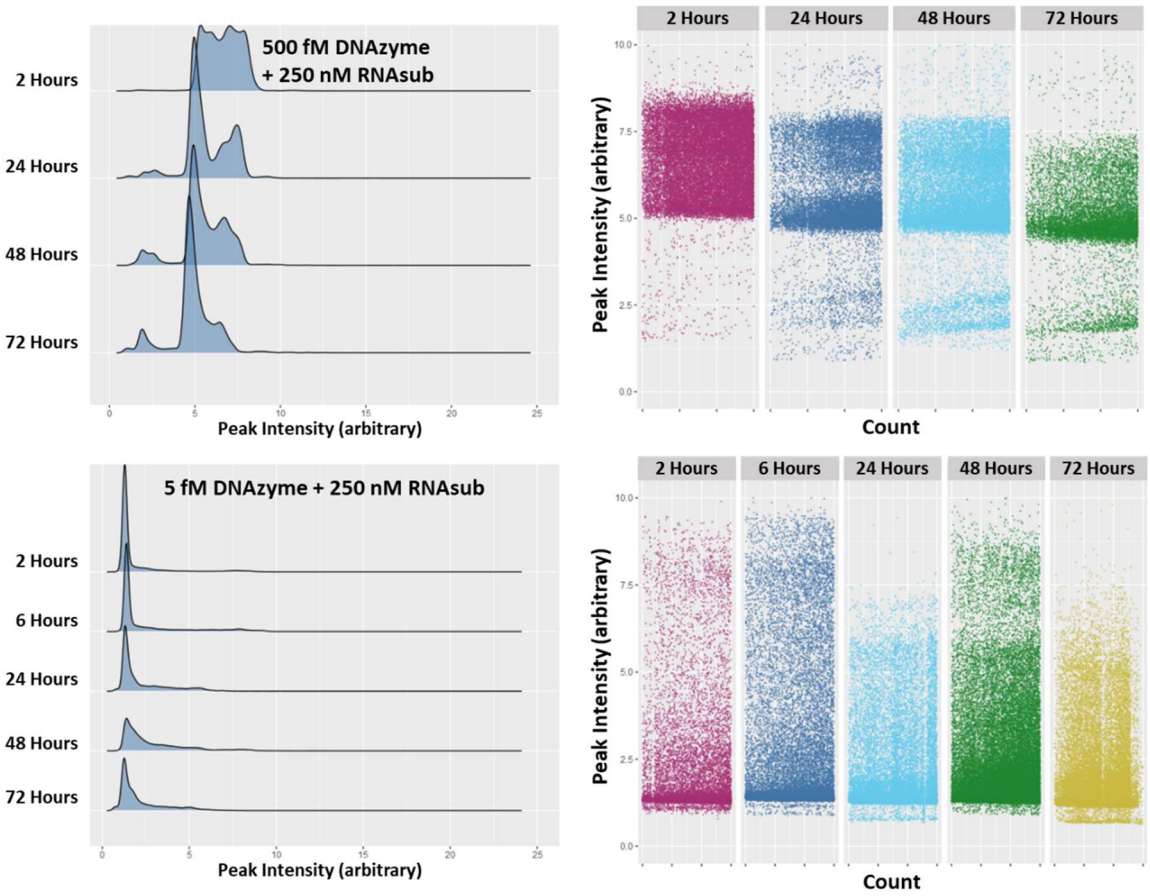

Figure 3.7*: Droplets containing 500 fM (top) or 5 fM DNAzyme (bottom) and 250 nM RNA substrate were detected over the course of a 72-hour incubation. Density plots (left) show the distribution of all droplet intensities, and dot plots (right) show the fluorescence intensity of individual droplets, with each peak represented by one point. The fluorescence intensity of positive droplets did not increase over the course of the incubation, indicating that little to no substrate cleavage occurs during this time.*

Droplets containing 5 fM DNAzyme presented similar results. As expected in the single catalyst regime, most droplets had a low fluorescence intensity and would be classified as negative (Figure 3.7, bottom density plot). A smaller number of droplets had higher fluorescence intensity. High-intensity droplets had a broad distribution of intensities, so there were not discrete "positive" and "negative" populations. More telling, the intensity of "positive" droplets also did not increase over time. If the activity of individual DNAzyme molecules was uniform and reflective of the bulk kinetics observed

in plate reader reactions, we would expect to see a population of droplets with uniformly high fluorescence intensity that increases with longer incubation times. Broad fluorescence distributions among the positive droplets could represent heterogeneity among catalytic molecules. However, the positive droplets shown in Figure 3.7 did not demonstrate a fluorescence increase with longer incubations. It is possible that the positive droplets are caused by noise, carryover, or a one-time increase in signal as opposed to true catalysis. Regardless, without a clear distinction between droplets that do and do not contain a catalyst, this platform would have limited application in catalyst detection experiments.

3.4.4 Binding control oligonucleotides

Across all droplet incubation experiments, it was clear that when the RNA substrate was in excess, increasing concentrations of the DNAzyme produced increased fluorescence intensity. However, this increase seemed to occur immediately after droplet generation, and the signal did not continue to rise over time. One possible explanation for this phenomenon is that the DNAzyme may increase droplet fluorescence without cleaving the substrate, either through its own intrinsic contribution to total fluorescence or because when the DNAzyme binds to the RNA substrate, a conformational change in the substrate moves the fluorophore further from the dark quencher, creating a small change in fluorescence that is measurable on the highly sensitive droplet detection platform. To test this hypothesis, two binding control sequences were designed. Each binding control sequence included the same substrate-binding arm sequences as the DNAzyme but a non-catalytic sequence between them. Figure 3.8A shows the fluorescence intensity of well plate reactions containing the RNA substrate and either the DNAzyme or binding control

oligonucleotides. The fluorescence intensity of the DNAzyme reaction increased over time, but the fluorescence of the binding control reactions remained constant, demonstrating that the controls are non-catalytic.

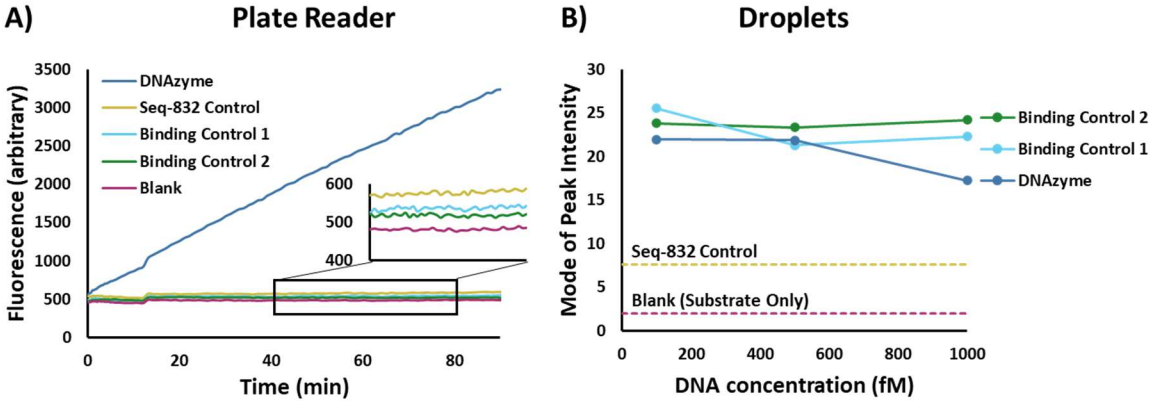

***Figure 3.8**: Binding of any sequence (catalytic or non-catalytic) to the RNA substrate causes a slight increase in droplet fluorescence intensity over the substrate alone. A) Fluorescence intensity of wells containing 100 nM RNA substrate and 1 nM DNA over the course of a 90-minute incubation. B) Mode of peak fluorescence intensity of droplets containing 250 nM RNA substrate and 100 fM, 500 fM, or 1000 fM DNA. DNA oligonucleotides incubated with the substrate include the catalytic 10-23 DNAzyme, two non-catalytic controls with substrate-binding hybridization arms, and the non-catalytic, non-binding Seq-832 control.*

Compared to blank droplets containing only the RNA substrate, droplets containing the substrate plus the non-binding, non-catalytic control Seq-832 showed slightly higher fluorescence (Figure 3.8B). Droplets containing the substrate plus the DNAzyme or either of the two binding controls showed even higher fluorescence. The fluorescence increase for all three binding DNA sequences was comparable, and no droplets showed fluorescence increases over time, confirming that there is a non-catalytic explanation for increased fluorescence in DNA-containing droplets.

3.4.5 Direct comparison of a bulk and droplet DNAzyme reaction

Figure 3.9 shows the fluorescence intensity of droplets containing 50 pM DNAzyme and 250 nM RNA substrate as they were detected over the course of a long incubation using either a plate reader to read the fluorescence of many droplets in a well (Figure 3.9A) or the droplet detection platform to read the fluorescence of each droplet individually (Figure 3.9B). In the bulk reaction on the plate reader, these substrate and catalyst concentrations produced a 4-fold increase in fluorescence intensity over the course of a 20-hour incubation, with fluorescence increasing roughly linearly throughout the entire 20-hour period (Figure 3.4). However, when the reaction is performed in droplets, there was no increase in fluorescence intensity over time, demonstrating no evidence of catalytic activity.

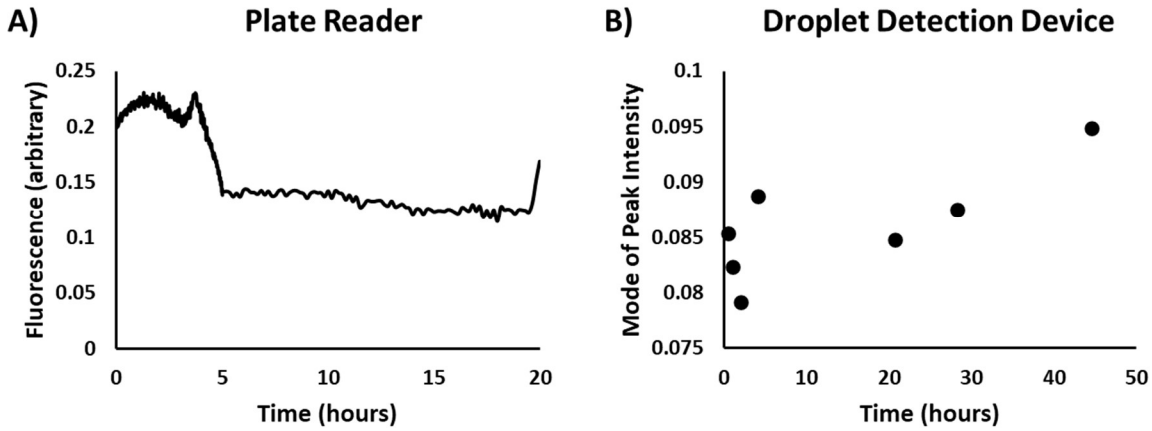

Figure 3.9*: Normalized fluorescence of droplets containing 50 pM DNAzyme and 250 nM RNA substrate detected over the course of a room-temperature incubation using A) a plate reader (many droplets detected in a single well) and B) a PDMS droplet detection device (droplets detected individually; mode of peak intensity reported).*

3.5 Conclusion

A well-characterized DNAzyme and its RNA substrate were used to explore the application of a droplet microfluidic platform for single molecule DNAzyme detection.

The DNAzyme performed well in microliter-scale reactions in a well plate. Its experimental turnover rate was consistent with literature reports at 3.4 reactions per minute, and DNA-catalyzed RNA cleavage continued at a stable rate over a period of at least 20 hours. However, when the same reaction was performed with identical DNAzyme and RNA substrate concentrations in droplets, there was no evidence of DNA-catalyzed RNA cleavage. Although addition of the DNAzyme generally produced a slight initial increase in the average droplet fluorescence compared to a non-catalytic control, there was no change in fluorescence over time.

The initial fluorescence increase could be explained by substrate conformational changes induced by catalyst binding. Control oligonucleotides were designed with binding arms complementary to the RNA substrate sequence but without the catalytic 10-23 core. Each of these binding controls increased the fluorescence of RNA substrate droplets compared to droplets with the substrate and a non-binding sequence or the substrate alone.

Another potential explanation for the initial increase in fluorescence intensity is that a small amount of catalytic cleavage occurs in the very brief time period after the substrate and catalyst meet on-chip but before the reaction is emulsified in droplets. Alternatively, the DNAzyme may be inactivated shortly after emulsification.

The absence of robust catalytic activity in droplets has concerning implications for the application of the droplet platform in DNA catalyst detection experiments. Single molecule detection requires high catalytic turnover over the course of a relatively long incubation period to produce a detectable concentration of the fluorescent product. These proof-of-concept experiments demonstrate that an otherwise catalytic DNA sequence does

not operate with high turnover in droplets. We have therefore highlighted a need to redesign the platform for future catalyst detection applications.

A significant difference between the reaction environments of the well plate and the droplets is the boundary of the reactor. The boundary of the well is a polystyrene wall designed to minimize analyte binding. Meanwhile, the boundary of the droplet is a water-oil interface stabilized by a proprietary surfactant. Interactions between the droplet interface and the DNAzyme, substrate, or counterions involved in the reaction may reduce DNAzyme activity in droplets. Future work should explore the application of alternative interfaces and "containers" for low-volume, DNA-catalyzed reactions. Other oil phases, particularly those with simple, non-proprietary formulations or those optimized for nucleic acid applications, could be used. Alternatively, small-scale reactions could be performed on microarray chips that remove the need for an oil phase altogether.

Chapter 4: Assessing surface adsorption in cyclic olefin copolymer microfluidic devices using two-dimensional nano liquid chromatography-micro free flow electrophoresis separations

4.1 Summary

Surface interactions are a concern in microscale separations, where analyte adsorption can decrease the speed, sensitivity, and resolution otherwise achieved by miniaturization. Here, we functionally characterize the surface adsorption of hot-embossed cyclic olefin copolymer (COC) micro free-flow electrophoresis (μFFE) devices using two-dimensional nLC × μFFE separations, which introduce a 3- to 5-second plug of analyte into the device and measure temporal broadening that arises from surface interactions. COC is an attractive material for microfluidic devices, but little is known about its potential for surface adsorption in applications with continuous fluid flow and temporal measurements. Adsorption was minimal for three small molecule dyes: positively charged rhodamine 123, negatively charged fluorescein, and neutral rhodamine 110. Temporal peak widths for the three dyes ranged from 3 to 7 seconds and did not change significantly with increasing transit distance. Moderate adsorption was observed for Chromeo P503-labeled myoglobin and cytochrome c with temporal peak widths around 20 seconds. Overall, COC surface adsorption was low compared to traditional glass devices, where peak widths are on the order of minutes. Improvements in durability, long-term performance, and ease of fabrication, combined with low overall adsorption, make COC μFFE devices a practical choice for applications involving time-resolved continuous detection.

4.2 Introduction

Micro free-flow electrophoresis (μFFE) is a technique used to separate components of a continuous sample stream. The sample enters a wide, planar separation channel, where it is carried toward the outlet by a continuous flow of buffer. Meanwhile, an electric field

applied perpendicular to the direction of buffer flow deflects analytes laterally based on their electrophoretic mobility.[183,185,186] μFFE has been used to separate a broad range of analytes, including fluorescent dyes,[190–192] amino acids,[194,195] proteins,[188,189,198–200] organelles,[205,206] and aptamers.[201,202,204] Its continuous sample flow is advantageous in preparative applications,[199,205,233,255,256] multidimensional separations,[194,195,219] reaction monitoring,[213,216,214,215] and rapid optimization or characterization.[201,206,218]

As is true for many microfluidic applications, the high surface area-to-volume ratio of the separation channel presents challenges for surface adsorption, particularly of large biomolecules like proteins. However, control of surface properties must be balanced with the ease, cost, and reproducibility of fabrication, as well as the performance and robustness of devices.

To address this balance, μFFE device fabrication methods have been developed for many materials. Glass devices are durable, chemically resistant, and optically transparent, but they must be fabricated in specialized photolithography facilities and often require surface treatment to reduce electroosmotic flow and surface adsorption.[187,205,219,224] Polymeric devices generally have lower fabrication costs, and a variety of fabrication methods offer faster prototyping and the potential for mass production. Hybrid glass-polydimethylsiloxane (PDMS) devices can be fabricated relatively easily using soft lithography techniques,[199,200,227,228] but device designs must counteract the deformability of PDMS by incorporating support pillars or increasing the aspect ratio of the separation channel. PDMS is also porous and hydrophobic, leading to both adsorption[257] and absorption[258] of analytes. Rigid polymer μFFE devices have been fabricated using fused

deposition modeling 3D printing,[231] polyjet 3D printing,[233] injection molding,[234,235] and computer numerical control milling.[236] Overall, the expansion of μFFE fabrication to a wider range of techniques and materials promises improved customizability to meet application-specific needs.

We have recently developed a cleanroom-free hot embossing method for fabrication of μFFE devices in COC.[259] The optical transparency, chemical resistance, rigidity, and durability of COC make it an appealing material for microfluidic applications. Additionally, COC fabrication costs are low compared to traditional glass etching, and COC device lifetimes are much longer than polymeric ABS devices. However, interactions between analytes and the surface of the COC separation channel have yet to be characterized.

Native COC is neutral and hydrophobic due to its composition of ethylene and norbornene monomers.[260] Hydrophobicity is often a concern in bioanalytical applications, where analytes like proteins interact strongly and sometimes irreversibly with the surface, causing carryover, sample loss, decreases in resolution, and quantitative inaccuracy. Microfluidic devices fabricated in COC often undergo surface treatments to introduce hydrophilic groups that reduce these interactions.[261] Common surface functionalization approaches include plasma treatments,[260,262–264] UV/ozone oxidation,[264–266] and hydrophobic chemical coatings introduced by UV photografting,[267–269] dip-coating,[270] or dynamic coating.[271]

Previous surface characterization studies have demonstrated that hydrophilic treatments successfully reduce adsorption in COC devices.[257,266–271] Surface-treated COC

devices exhibit similar or lower adsorption of proteins[266] and hydrophobic small molecules[257] than devices made from other surface-treated polymers. However, these studies rely on single-timepoint measurements of analyte retention or recovery after a period of incubation. For example, a device may be flushed with a solution of fluorescently-labeled analyte, rinsed, and imaged to determine long-term adsorption. They offer limited insight on the functional effects of surface adsorption in dynamic, temporal applications with a continuous flow of solution and fluctuating analyte concentrations.

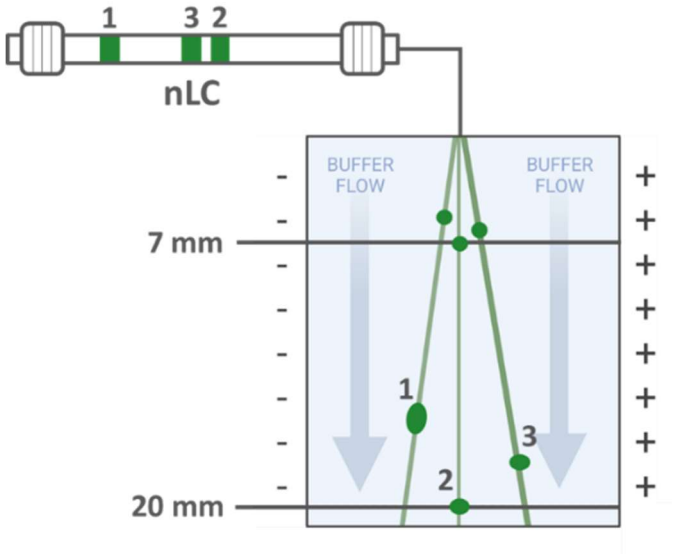

Figure 4.1*: Diagram of a nLC × µFFE separation. A sample is injected onto a nLC column, which flows directly into the µFFE device. Separated analytes are detected at multiple distances from the device inlet (7 mm, 20 mm, etc.). In this illustration, analyte 1 experiences temporal broadening due to surface adsorption while analytes 2 and 3 do not. Created with Biorender.com.*

We have previously characterized surface adsorption in glass[188] and ABS[189] devices using two-dimensional nano liquid chromatography (nLC) × µFFE separations. Figure 4.1 summarizes this technique. The nLC dimension separates analytes in time based on their affinity for the stationary and mobile phases. Analyte plugs then leave the nLC column and flow directly into the µFFE separation channel. In the µFFE dimension, an electric field

applied perpendicular to the direction of buffer flow separates analytes in space based on their electrophoretic mobility. Fluorescence intensity is detected across the width of the separation channel at several distances from the sample inlet. Analytes that adsorb significantly to the device's surface will have broader temporal peak widths as the distance from the sample inlet increases. This approach is particularly valuable in its dynamic quantification of analyte adsorption in a continuous-flow system. In the current manuscript, we characterize surface adsorption in COC μFFE devices and compare these results to previous adsorption studies in glass and ABS, an investigation with broader implications for the development of microfluidic technologies using thermoplastic materials.

4.3 Experimental

4.3.1 Chemicals and reagents

Chemicals were purchased from Sigma-Aldrich (St. Louis, MO) unless otherwise specified. Solutions were prepared using deionized water (18.3 MΩ, Milli-Q; Millipore, Bedford, MA) unless otherwise specified. μFFE separation buffer contained 25 mM HEPES and 300 μM Triton X-100, adjusted to pH 7.0 using 1 M NaOH and filtered through a 0.22 μm nitrocellulose filter membrane (Millipore). Triton was omitted from the Triton-free buffer used in EOF and protein adsorption experiments.

Eluents for nLC were prepared using methanol (Fisher Scientific, Fair Lawn, NJ), water (Fisher), acetonitrile (ACN, Fisher) and trifluoroacetic acid (TFA), all HPLC-grade. Rhodamine 110 chloride, rhodamine 123, and fluorescein disodium were dissolved in 190 proof ethanol (Fisher) at 0.98, 0.76, and 1.05 mg/mL, respectively, and diluted to their final concentrations in HPLC-grade water. Myoglobin (equine skeletal muscle) and cytochrome

c (bovine heart) (Sigma-Aldrich) were dissolved in 10 mM aqueous $NaHCO_3$ at concentrations of 1.1 and 2.0 mg/mL, respectively. To label the proteins, a 10 mg/mL Chromeo P503 (Santa Cruz Biotech, Dallas, TX) solution in DMSO (Fisher) was prepared. A 10 µL aliquot of the Chromeo P503 solution was added to 490 µL of each protein solution and vortexed for 10 minutes. Mixtures were incubated at room temperature for 24 hours. Fluorophore solutions and labeled proteins were stored at 4°C when not in use. Samples for nLC were filtered using a 0.4 mm diameter, 0.22 µm cellulose acetate syringe filter (Restek, Bellefonte, PA).

4.3.2 µFFE device fabrication

Figure 4.2 shows representative µFFE devices fabricated in COC with one (Figure 4.2A) and two (Figure 4.2B) buffer inlets. The devices have a 40 µm deep separation channel that is 10 mm wide by 25 mm long. The separation channel is flanked on both sides by electrode channels that are 400 µm deep and 2 mm wide.

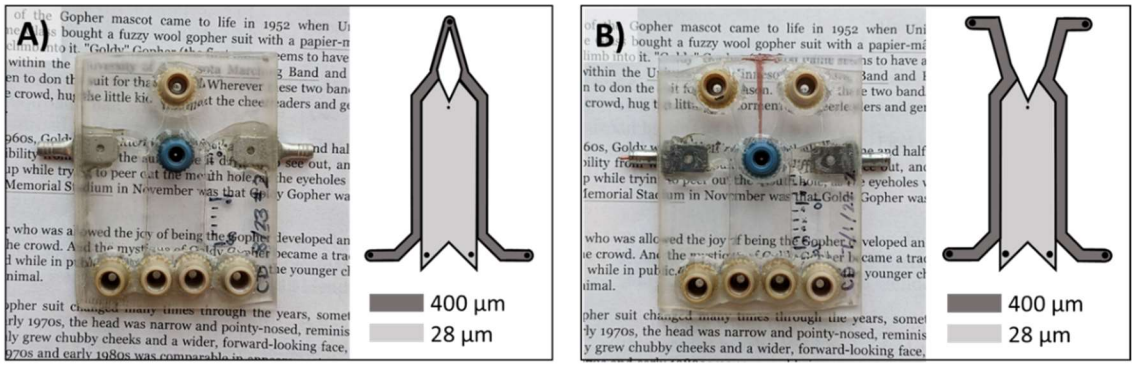

***Figure 4.2**: µFFE devices (total dimensions 1.75 in. wide × 2.25 in. long) fabricated in COC using hot embossing and solvent vapor assisted thermal bonding. Devices have either one (A) or two (B) buffer inlets and four outlets. The sample capillary enters the separation channel through a small hole (blue NanoPort) drilled at a 90° angle with the direction of buffer flow. Diagram shading indicates feature depth.*

We have recently described a method for fabrication of μFFE devices in COC.[259] Briefly, a master mold with raised device features was printed in Verowhite resin (Sculpteo Inc., Oakland, CA) using a Stratasys J750 Polyjet 3D printer. A positive mold was then cast in Silastic RTV-3110 polymer with Xiameter RTV-3010S catalyst (Dow, Midland, MI). From the Silastic mold, a negative hot-embossing mold was cast in Weicon C (Weicon, Ontario, Canada). The features on the Weicon C mold were transferred to pre-cut TOPAS 6017s-04 COC (TOPAS, Raunheim, Germany) substrates by hot embossing. COC was embossed at 185°C under a load of 750 pounds on a Carver thermal press (Wabash, IN), then de-embossed at 173°C. Substrates were flatted at 149°C under a load of 100 pounds. The imprinted surface was clarified by 30 minutes of exposure to cyclohexane (Fisher) vapor at room temperature to reduce surface imperfections that may scatter light during detection.

A platinum wire (0.1 mm diameter, Alfa Aesar, Haverhill, MA) was threaded through a 400 μm hole drilled at the top of each electrode channel and pressed in place along the entire length of the channel using a hot soldering iron. A second, unimprinted COC substrate was prepared by drilling 1 mm holes aligned with each buffer inlet and outlet and a 400 μm hole for sample entry at the top of the separation channel.

The embossed substrate was bonded to the cover substrate through solvent vapor assisted thermal bonding. The unimprinted COC substrate was exposed to cyclohexane vapor for 34 minutes, and the imprinted substrate was exposed for 9 minutes. The exposed faces were pressed together so that port holes aligned with channels, and the device was

held at 200°F under a load of 250 pounds for 30 minutes to fully bond the edges of the channels.

The wire electrodes were soldered to durable wire terminals, which were attached to the device and coated with protective quickset epoxy (Loctite, Westlake, OH). NanoPorts (Upchurch Scientific, Oak Harbor, WA) were aligned over the holes drilled in the cover substrate and glued in place using quickset epoxy.

The sample capillary was introduced through a hole in the top substrate so that sample flow met buffer flow at a 90° angle. A 380 µm I.D. NanoPort was aligned with the 400 µm hole at the top of the separation channel. The insertion depth of the sample capillary was adjusted to match the thickness of the COC to minimize dead volume at the interface of the capillary and separation channel.

4.3.3 Two-Dimensional nLC × µFFE separations

Nano-liquid chromatography (nLC) separations were performed using a Thermo-Dionex UltiMate3000 RSLC nano pump with WPS autosampler (Waltham, MA), controlled using Chromeleon v6.8 software (Thermo-Dionex). The analytical column (Thermo-Dionex Part number 164562) was 75 µm i.d. × 15 cm long packed with 2 µm Acclaim PepMap C18 particles. For the fluorescent dye separations mobile phase A was H_2O with 0.1% TFA and mobile phase B was 90:10 MeOH:H_2O with 0.1% TFA. The composition of the isocratic mobile phase was 15:85 A:B. For protein adsorption experiments mobile phase A was H_2O with 0.1% TFA and mobile phase B was 90:10 ACN:H_2O with 0.1% TFA. The composition of the isocratic mobile phase was 40:60 A:B. Separations used 500 nL injections and a 300 nL/min flow rate.

The end of the nLC column was connected to an intermediate fused silica capillary using a PTFE sleeve (Thermo Fisher, Waltham, MA). The intermediate capillary was connected to the sample capillary using a zero dead volume microfluidic union and MicroTight sleeves (IDEX, Lake Forest, IL), and the sample capillary flowed directly into the μFFE device.

For nLC × μFFE separations of fluorescent dyes, separation buffer was pumped through a two-inlet μFFE device (Figure 4.2B) at a flow rate of 2 mL/min using a pressure-driven microfluidic flow controller and ESI software (Elveflow, Paris, France). Flow was split at a microfluidic tee (IDEX) immediately before the device, so the flow rate at each inlet was 1 mL/min. Linear velocity in the separation channel was ~0.7 mm/sec. Upon injection, +75 V was applied to the right electrode while the left was held at ground. The dye sample contained 5.2 μM fluorescein, 0.2 μM rhodamine 110, and 1.6 μM rhodamine 123.

The same buffer flow rate was used for protein separations, and +100 V was applied across the device. The protein mixture contained 0.22 mg/mL Chromeo P503-labeled myoglobin and 1.6 mg/mL Chromeo P503-labeled cytochrome c. Individual protein injections used 2.8 mg/mL Chromeo P503-labeled myoglobin and 3.6 mg/mL Chromeo P503-labeled cytochrome c.

4.3.4 Electroosmotic flow (EOF)

For the one-dimensional separations used in EOF experiments, separation buffer was pumped through a one-inlet μFFE device (Figure 4.2A) at a flow rate of 3 mL/min (~0.3 mm/sec in the separation channel). A syringe pump (Harvard Apparatus, Holliston,

MA) was used to pump a mixture of fluorescein (1.2 μM), rhodamine 110 (0.2 μM), and rhodamine 123 (1.6 μM) into the sample inlet at 500 nL/min. Potentials from +25V to +100V were applied in 40-second pulses.

4.3.5 LIF detection

For laser-induced fluorescence (LIF) detection, a 50 mW beam from a variable power 488 nm 150 mW diode pumped solid state laser (Sapphire, Coherent, Santa Clara, CA) was expanded to a ~2.5 cm wide by ~150 μm thick line across the μFFE separation channel. To investigate broadening effects, replicate separations were performed with the detection line positioned at several distances from the top of the separation channel. For on-capillary detection, a window was burned in a 360 μm O.D., 20 μm I.D. fused silica capillary (Polymicro Technologies, Phoenix, AZ) and positioned under the laser line.

Fluorescence imaging across the separation channel was performed using a Prime BSI Express camera (Teledyne Photometrics, Tucson, AZ) mounted on an AZ 100 stereomicroscope (Nikon, Tokyo, Japan) with a 0.5× objective. Fluorescent dye separations were imaged using an exposure time of 200 ms and an Endow GFP filter cube (Nikon) containing a dichroic mirror (495 nm cutoff) and a 500-550 nm band pass filter. Separations of Chromeo P503-labeled proteins were imaged using an exposure time of 500 ms and a custom filter cube (Nikon) containing a dichroic mirror (500 nm cutoff) and a 570-640 nm bandpass filter.

4.3.6 Data analysis

Image stacks were acquired and binned in μManager software.[272] For each frame in the stack, the fluorescence intensity at each pixel across the detection zone was tabulated

using ImageJ.[273] Subsequent data analysis, including background subtraction, signal averaging, plotting, slicing, and peak finding, were performed using custom Matlab scripts. Total chromatograms show the maximum intensity value across the separation channel for each timepoint. Extracted chromatograms represent the intensity at a single position in the separation channel for each timepoint. Asymmetry was assessed by fitting chromatogram peaks to a fifth-degree Gaussian function. Peak asymmetry factors were calculated at 1/10 the max height.

4.4 Results and Discussion

4.4.1 Fluorescent dye surface adsorption

Although COC is an attractive material for microfluidic techniques like μFFE, previous characterizations of analyte adsorption in COC devices do not adequately describe dynamic adsorption patterns in continuous-flow applications. Therefore, the functional effects of surface adsorption in COC devices were quantified using two-dimensional nLC × μFFE separations. nLC separations create discrete analyte plugs that enter the μFFE separation channel and are carried to the outlet by a continuous flow of separation buffer. As they travel the length of the channel, plugs are separated laterally according to their electrophoretic mobility (Figure 4.1). Previous nLC × μFFE studies in glass[188] and ABS[189] devices have demonstrated that broadening in the lateral dimension is governed by diffusion and hydrodynamics. Meanwhile, broadening in the temporal dimension is governed by interactions between the analyte and the channel surfaces. Strong surface interactions delay analyte transit through the separation channel, inducing broadening and asymmetry in the temporal dimension.

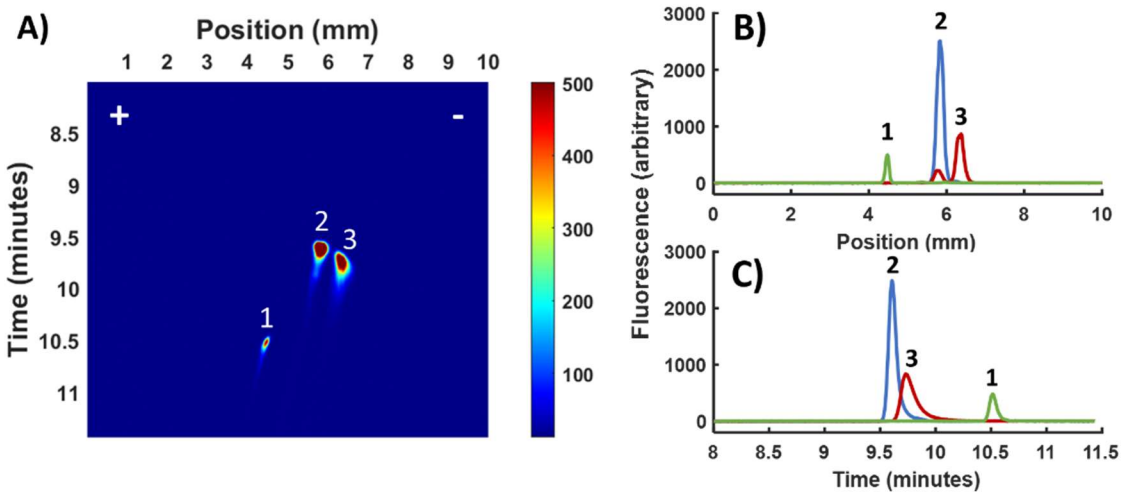

***Figure 4.3**: nLC × µFFE separation of fluorescein (1), rhodamine 110 (2), and rhodamine 123 (3), detected 17 mm from the sample inlet. A) Three-dimensional plot of fluorescence intensity in time (nLC dimension) and space (µFFE dimension). B) Intensity across the width of the µFFE separation channel at 9.61 minutes (rhodamine 110), 9.73 minutes (rhodamine 123), and 10.52 minutes (fluorescein). C) Chromatograms extracted at a separation channel position of 4.48 mm (fluorescein), 5.83 mm (rhodamine 110), and 6.38 mm (rhodamine 123).*

Figure 4.3 shows a nLC × µFFE separation of fluorescein, rhodamine 110, and rhodamine 123 in a COC device. Although rhodamine 110 and rhodamine 123 coelute in the nLC separation, addition of the µFFE dimension achieves complete resolution of all three dyes. At each time point, the plot of fluorescence intensity versus separation channel position gives narrow, well-resolved peaks (Figure 4.3B). Single-dye chromatograms can be extracted from the two-dimensional separation by plotting fluorescence intensity over time at a single position on the separation channel (Figure 4.3C).

The nLC × µFFE dye separation was repeated at four positions on the separation channel. For each separation, single-dye chromatograms were extracted (Figure 4.4A). Qualitatively, there was no apparent change in peak shape, and the relative retention times of the three peaks were consistent across all detection positions.

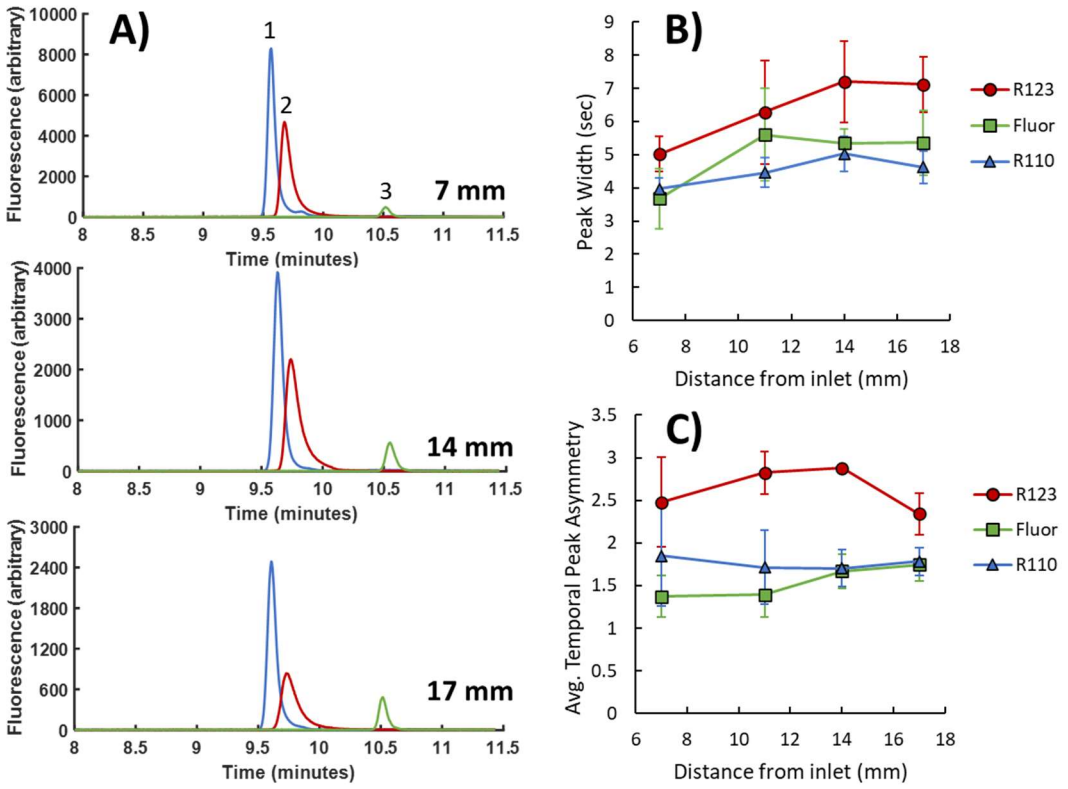

***Figure 4.4**: Extracted chromatograms (A) for rhodamine 110 (1), rhodamine 123 (2), and fluorescein (3) at 7 mm, 14 mm, and 17 mm from the sample inlet. Average temporal peak width (B) and peak asymmetry (C) were calculated for peaks detected at four positions along the µFFE separation channel. n = 3-5 for each detection distance.*

Figure 4.4B shows the average and standard deviation of temporal peak width (at half max height) for replicate separations at each position. As the distance from the sample inlet increased, there was a slight increase in temporal peak width for each of the three dyes. Figure 4.4C shows the average and standard deviation of temporal peak asymmetry for replicate separations at each detection position. There was minimal increase in peak asymmetry with increasing distance from the sample inlet. Combined, the small increase in peak width and asymmetry as peak transited the µFFE separation channel demonstrates minimal adsorption of small molecules on the COC surface, regardless of the net charge of the analyte.

The neutral, hydrophobic surface of COC is expected to have limited interaction with small molecules that carry a positive (rhodamine 123) or negative (fluorescein) net charge. Rhodamine 110 has no net charge but carries both a positive and a negative charge at pH 7 and is also expected to have little interaction with COC. A previous study of surface adsorption in ABS devices, which present a neutral, hydrophilic surface, found no temporal broadening for rhodamine 123 or fluorescein.[189] However, ABS μFFE devices demonstrated 2-fold temporal broadening and a 2.5-fold increase in temporal asymmetry of the rhodamine 110 peak. In this case, it appears that the relative hydrophobicity of COC reduces adsorption of neutral, hydrophilic analytes like rhodamine 110 compared to a more hydrophilic polymer like ABS.

Both COC and ABS devices demonstrated minimal dye adsorption compared to glass devices, which have a negative surface charge and experienced 5-fold temporal broadening of the rhodamine 123 peak.[188] On glass devices, the rhodamine 123 peak width increased from approximately 10 seconds near the sample inlet to 50 seconds near the outlet.[188] Given these clear examples of surface adsorption in ABS and glass devices, the COC device appears to have very little interaction with small molecule analytes of any charge.

Physical surface properties like roughness, topology, and porosity also influence adsorption. While glass devices have smooth channel surfaces with minimal defects from the fabrication process, the physical surfaces of ABS and COC devices depend substantially on the 3D printing and hot embossing processes, respectively. Future studies

could combine nLC × μFFE separations with physical surface characterization to explore the relationships between fabrication parameters, surface topology, and surface adsorption.

4.4.2 Electroosmotic flow

Surface properties of COC devices were also compared to previous device materials by assessing the strength of electroosmotic flow (EOF), which arises from surface charge. EOF was determined using the migration distance of the rhodamine 110 peak under an applied potential. In the absence of EOF, neutral rhodamine 110 should not shift from the position of the resting stream at 0 V. Observed movement of the peak on application of the electric field is attributed to EOF. Stronger surface charge results in higher EOF and a larger shift in peak position. Figure 4.5 shows the migration distance (relative to the resting stream at 0 V) of fluorescein, rhodamine 110, and rhodamine 123 in continuous μFFE separations. Bold plots show separations performed in normal separation buffer with 300 μM Triton X-100. EOF acts equally on the total mobility of all analytes, and negative surface charge causes all peaks – including rhodamine 110 – to shift toward the cathode.

Although COC showed minimal interaction with charged analytes, the existence of low EOF toward the cathode suggests that the surface bears some negative charge. The EOF recorded with normal separation buffer was 2.3×10^{-5} cm^2 V^{-1} s^{-1}, a 17-fold reduction over glass devices (3.80×10^{-4} cm^2 V^{-1} s^{-1}) and a 4-fold reduction over PEO-treated glass devices (8.63×10^{-5} cm^2 V^{-1} s^{-1}).[187] EOF was measured in glass devices without any surfactants or additives in the separation buffer, so these values reflect the uniformly negative surface of untreated glass and the reduced surface charge achieved by PEO

treatment. As expected, COC devices present much less surface charge than glass devices, even after surface treatment.

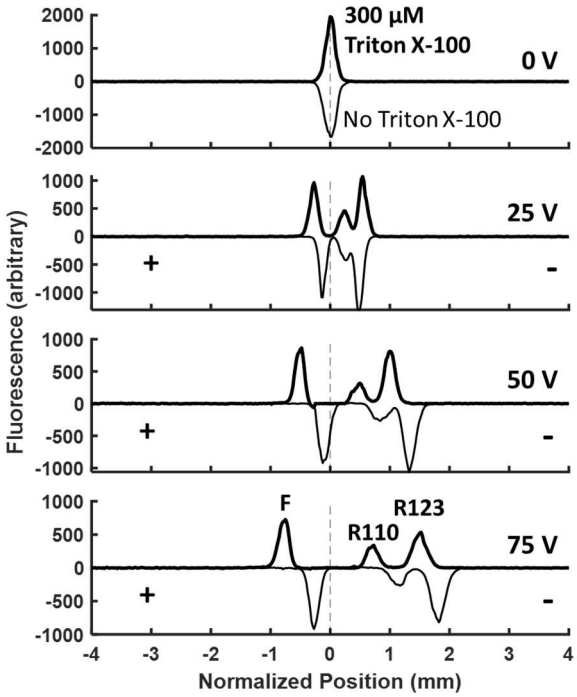

***Figure 4.5**: µFFE separations of fluorescein (F), rhodamine 110 (R110), and rhodamine 123 (R123) at 0-75 V, normalized to the position of the resting stream at 0 V. Separations were performed with 300 µM Triton X-100 in buffer (bold intensity plots, EOF = 2.3 × 10^{-5} cm^2 V^{-1} s^{-1}) and without Triton X-100 in buffer (inverted intensity plots, EOF = 3.3 × 10^{-5} cm^2 V^{-1} s^{-1}).*

The EOF in COC devices was 2-fold higher than the EOF measured in ABS devices with Triton X-100 in the separation buffer (1.1 × 10^{-5} cm^2 V^{-1} s^{-1}). Both ABS and COC are expected to have low surface charge and similar interactions with Triton X-100.

Triton X-100 is a surfactant added to the µFFE separation buffer to minimize interference from electrolysis bubbles.[274] By performing, brief separations at low voltages in Triton-free buffer, we were able to directly assess the interaction between Triton X-100 and the COC surface. We hypothesized that the COC surface would interact primarily with the hydrophobic ends of Triton X-100, leaving hydrophilic tails to interact with analytes.

This increase in surface hydrophilicity, while maintaining a neutral charge, was expected to decrease protein adsorption and potentially increase the accumulation of surface charge.

Inverted plots in Figure 4.5 show dye separations performed in Triton-free buffer. The larger shift toward the cathode indicates greater EOF in the absence of Triton X-100 compared to separations with Triton X-100. When Triton X-100 was removed from the separation buffer, EOF increased from 2.3×10^{-5} $cm^2 V^{-1} s^{-1}$ to 3.3×10^{-5} $cm^2 V^{-1} s^{-1}$. This change suggests that that Triton X-100 does indeed reversibly modify the COC surface. Specifically, Triton X-100 decreases the total COC surface charge, which contradicts our hypothesized surfactant interaction. These results suggest that the surface of native COC may be less nonpolar than originally thought. Sources for residual charges present on the native COC surface may be surface oxidation during fabrication or by an accumulation of charged species during operation. Triton X-100 could then decrease surface charge by masking oxidized groups, presenting a more uniformly hydrophilic, neutral surface. Given these results, it may be possible to tune surface properties to minimize analyte interactions by optimizing buffer composition.

4.4.3 Protein surface adsorption

Surface adsorption poses particularly complex challenges to biological separations. Analytes like proteins often present regions of high surface charge, hydrophobic pockets, or conformational flexibility, which contribute to multi-faceted surface interactions. To test protein adsorption on the surface of COC devices, we performed a two-dimensional separation of myoglobin and cytochrome c (Figure 4.6), proteins that demonstrate particularly strong adsorption on glass surfaces.[188]

Chromeo P503-labeled myoglobin and cytochrome c were first detected on a fused-silica capillary immediately after the nLC column. To prevent surface adsorption in the capillary, the mobile phase contained TFA, and the inner surfaces of the capillary were coated with PEO.[275] Figure 4.6A shows a nLC × µFFE separation of the two proteins. The nLC chromatogram for the mixture shows two narrow, unresolved peaks (Figure 4.6B), but addition of the µFFE dimension successfully separates the proteins. At an applied potential of 100 V, myoglobin and cytochrome c were separated with near-complete resolution in the spatial dimension (Figure 4.6C), once again demonstrating the utility of multidimensional µFFE separations. Although peak broadening is obvious in the temporal dimension, the peaks are narrow and symmetrical in the spatial dimension. This is consistent with previous findings that surface adsorption has no effect on spatial broadening or position in µFFE.[188]

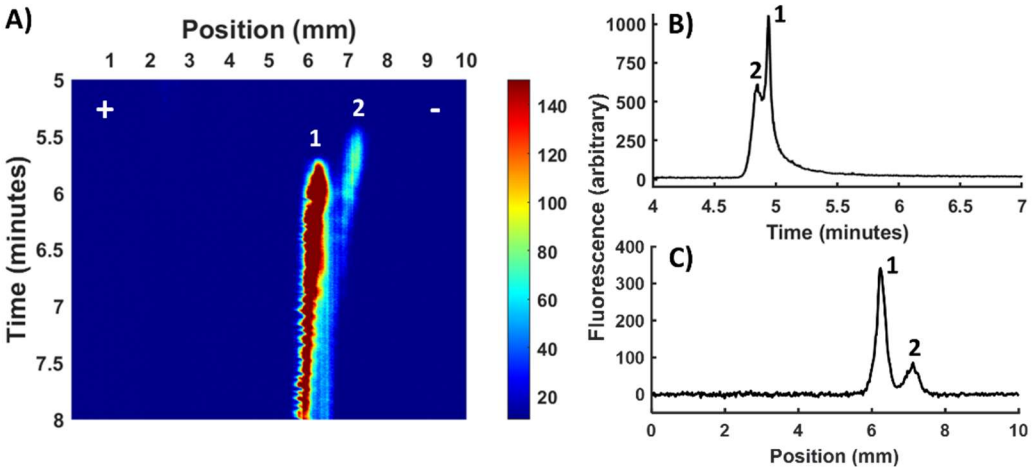

***Figure 4.6**: A) Three-dimensional plot of nLC × µFFE separation of Chromeo P503-labeled myoglobin (1) and cytochrome c (2). B) nLC separation of Chromeo P503-labeled myoglobin and cytochrome c detected before entering the COC device. C) Plot of fluorescence intensity measured across the width of the µFFE separation channel at 5.8 min.*

Figure 4.7 shows total chromatograms for single-protein nLC × µFFE injections of Chromeo P503-labeled myoglobin and cytochrome c at two positions on the µFFE

separation channel. Bold plots show injections performed in normal μFFE separation buffer with 300 μM Triton X-100, and inverted plots show injections performed in Triton-free buffer. To isolate the effects of surface adsorption from flow imbalances and instabilities, proteins were injected separately and detected with no electrical potential applied at the electrodes. Compared to the 5-second peak widths observed for the proteins after nLC separation (Figure 4.7, top), both the myoglobin and cytochrome c peaks were measurably broader (~20 seconds) on the μFFE device. Cytochrome c was particularly difficult to remove from the surface, requiring at least 20 minutes of flowing buffer to return completely to baseline signal.

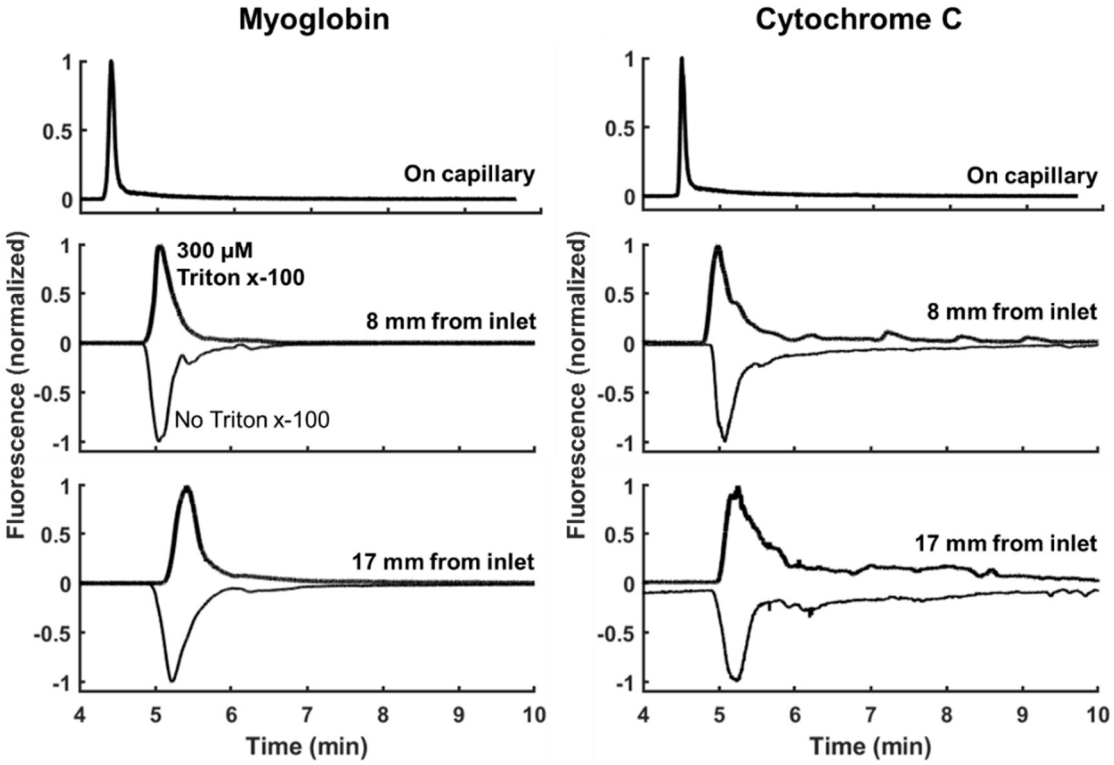

Figure 4.7*: Total chromatograms of Chromeo P503-labeled myoglobin and cytochrome c recorded in the sample capillary (top) and in the μFFE separation channel 8 mm (middle) and 17 mm (bottom) from the sample inlet. Bold chromatograms: separation buffer with 300 μM Triton X-100. Inverted chromatograms: separation buffer with no Triton X-100.*

Protein adsorption in COC devices was much lower than in glass devices, where myoglobin and cytochrome c peaks broadened to widths on the order of minutes, and full cytochrome c desorption occurred only after NaOH treatment.[188] However, it was higher than the adsorption reported in ABS devices, where peaks were under 15 seconds wide with full cytochrome c desorption in under 30 seconds.[189]

Although there was dramatic peak broadening between the nLC chromatogram and initial μFFE detection site, relatively small increases in myoglobin and cytochrome c peak widths were observed between the detection point near the sample inlet and the point near the outlet (Figure 4.7). This suggests that protein-COC interactions make a relatively small contribution to peak broadening as the sample transits the separation channel. The most influential contributor is the interface of the sample capillary and the separation channel. Since minimal broadening was observed at this interface during dye separations (Figure 4.3), interfacial broadening of protein peaks was likely driven more by adsorption to surfaces at the interface than by dead volume or hydrodynamic patterns in the sample inlet. Interface effects may also help to explain why more peak broadening occurred in COC devices than in ABS devices, which used a co-linear sample inlet with lower dead volume.[219]

There was no quantifiable change in protein peak width or shape when Triton X-100 was removed from the running buffer, suggesting that COC and Triton-modified COC exhibit similar interactions with the selected proteins. This reinforces the results of the EOF experiments, which suggest that the native COC surface is more polar than expected, and

Triton X-100 interactions do not necessarily present a substantially more hydrophilic surface layer.

The existence of protein adsorption in COC devices is well established.[266–271] However, nLC-μFFE separations provide unique contextual insight on the temporal dynamics of adsorption in a continuous-flow system. The relatively low protein adsorption on COC surfaces is appropriate for many μFFE applications, especially those that rely primarily on lateral, electrophoretic separation, which is not affected by surface interactions. Optimization of the sample interface is expected to reduce temporal broadening for applications that require temporal measurements on timescales under a minute. Additional surface treatments or buffer additives may also be beneficial in improving temporal resolution. The durability of COC devices (operating lifetimes >6 months) and low fabrication costs (under $100) are significant advantages over ABS and PEO-treated glass devices.

4.5 Conclusion

Hot embossed COC devices are appealing for a broad range of microfluidic applications because they represent a compromise between the robust long-term performance of etched glass devices and the accessible, inexpensive fabrication of other polymeric devices. Here, we demonstrate that COC devices for μFFE exhibit much lower surface adsorption than traditional glass devices, and that the surface of COC devices is less hydrophobic than initially assumed. The two-dimensional nLC × μFFE separations used here offer a dynamic, functional characterization of surface adsorption that is particularly relevant to temporal response and resolution. The surface properties of COC

devices, in addition to their durability, performance, and ease of fabrication, make them excellent candidates for a wide range of microfluidic applications, including biological separations and time-resolved continuous detection.

Chapter 5: A noncompetitive, aptamer-based affinity assay for continuous quantification of tumor necrosis factor α

5.1 Summary

Affinity assays are ubiquitous tools for quantifying biorelevant molecules. They use an affinity reagent – most often an antibody – that binds to a target with high specificity and selectivity. Most affinity assays also include a signal amplification tool that gives the assay high sensitivity. However, existing affinity assays use discrete samples and therefore quantify targets at discrete timepoints. They are not well-suited for measuring changes in concentration over time. This chapter describes the development of a continuous affinity assay for the quantification of tumor necrosis factor α (TNFα) using micro free-flow electrophoresis (μFFE). This noncompetitive assay uses a fluorescently-labeled aptamer to bind TNFα. The bound and unbound aptamer species are separated, detected, and quantified on a μFFE device. Changes in the aptamer fraction bound reflect changes in the concentration of TNFα in the sample. The μFFE aptamer assay was able to detect TNFα concentrations as low as 100 nM (1.7 μg/mL). The effects of sample and separation buffer strength on aptamer binding and μFFE separation were explored, and continuous, online injections of TNFα were performed.

5.2 Introduction

Affinity assays are a popular and effective tool for protein, peptide, metabolite, and pharmaceutical quantification.[276,277] Examples of widely-used affinity assays include enzyme-linked immunosorbent assays (ELISAs),[278] which use a signal-amplifying enzyme to report antibody-antigen binding, and lateral flow immunoassays,[279] which use immobilized antibodies on a paper-based flow channel to capture an antigen of interest.

Although most commercial affinity assays use antibodies as their affinity reagent, aptamer-based assays are also capable of sensitive and selective detection.[172,174,177]

Despite the success and popularity of affinity assays, a limitation of existing assays is that they use discrete samples, a disadvantage when studying fundamentally dynamic biological processes. Prominent techniques like ELISAs and lateral flow assays are not well-suited for profiling changes in antigen concentration over time.

One challenge of adapting affinity assays for continuous detection is the high affinity of antibodies and aptamers for their targets. Antibody and aptamer dissociation rates (k_{off}) are typically on the order of hours to days. Although this trait lends sensitivity and robustness to discrete assays, it also means that an individual antibody or aptamer molecule cannot report dynamic changes in antigen concentration.[280] The affinity reagent will stay bound to the target well after the target concentration has changed. Dynamic affinity assays need both a continuous sample and a continuous supply of fresh affinity reagent, requirements that are difficult and expensive to meet in the microwell formats often used in commercial assays.

Micro free-flow electrophoresis (μFFE) is a separation technique that can monitor analytes in continuously flowing samples. The sample enters a wide, planar separation channel and is carried by a continuous flow of separation buffer from the inlet to the outlet of the device. An electric field oriented perpendicular to the direction of buffer flow is applied across the entire separation channel, so analytes in the sample are separated laterally based on their electrophoretic mobility.[183,185,186]

μFFE has been used to separate a wide range of analytes. Its continuous nature makes it particularly well-suited for monitoring dynamic samples or processes over time.[186] For example, μFFE has been used for real-time reaction monitoring,[213–216] rapid optimization,[218] and two-dimensional separations of small molecules, amino acids, peptides, and proteins.[188,189,194,195,219] The separation power achieved in μFFE is often high enough to resolve a protein-bound aptamer and its unbound counterpart, and μFFE has been used for aptamer selection,[202] rapid characterization of aptamer binding kinetics,[201] and quantification of aptamer-protein complexes.[204] The small sample volumes, high separation efficiency, and continuous detection capabilities of μFFE make it an excellent platform for the development of continuous affinity assays. Small quantities of affinity reagent can be mixed into a flowing sample stream containing a target of interest. When the sample stream enters the μFFE device, the bound target complex will be continuously separated from excess affinity reagent, and sample composition can be monitored in real time.

Here, we describe the development of a noncompetitive aptamer affinity assay for continuous quantification of TNFα using μFFE. Aptamers offer several advantages over antibodies in the context of a μFFE affinity assay. First, aptamers can be chemically synthesized, reducing cost, decreasing labeling variability, and improving customizability over antibody reagents. Aptamers are also smaller than antibodies. When they bind to a target, there is a larger shift in electrophoretic mobility and therefore better resolution between the bound and unbound species during μFFE. Because of this large mobility shift, the aptamer can be directly labeled and used in a noncompetitive assay. μFFE-based

aptamer assays have recently been presented as an ELISA alternative with particular value for quantifying challenging targets or nuanced stoichiometries.[203,204,220] However, previously-reported assays use static samples and cannot quantify dynamic changes in target concentration over time.

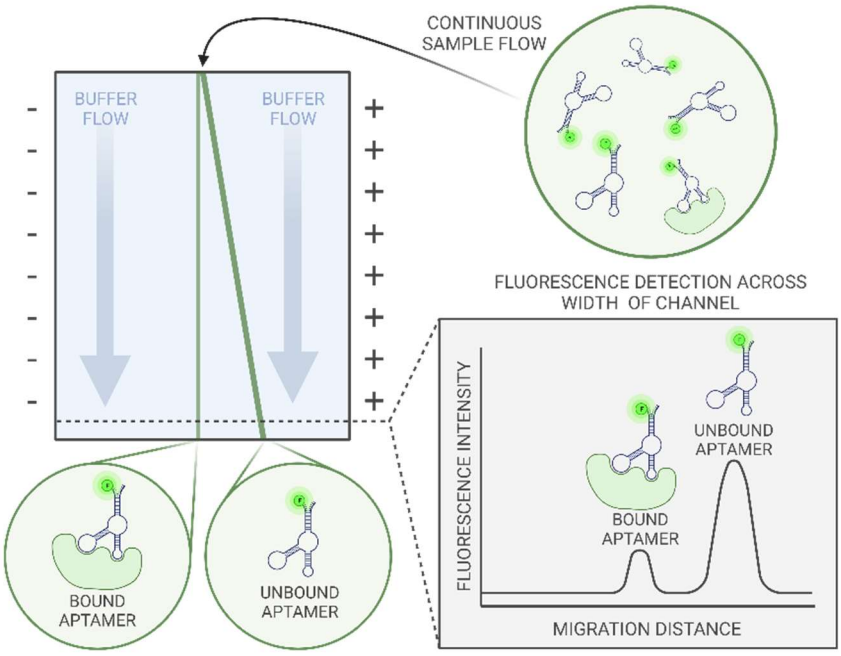

***Figure 5.1**: A continuous, noncompetitive aptamer affinity assay using μFFE. A sample containing a protein of interest is mixed with a fluorescently-labeled aptamer and flowed into the separation channel. The bound and unbound aptamer species are continuously separated and detected. Changes in bound and unbound peak intensity reflect changes in protein concentration. Created with Biorender.com.*

Figure 5.1 illustrates the design of the continuous μFFE aptamer assay. A sample containing TNFα is mixed with a fluorescently-labeled DNA aptamer. After an incubation period, the sample flows into the separation channel, where the bound and unbound aptamer species are separated according to their differing electrophoretic mobilities. TNFα is quantified based on fluorescence detection of the bound and unbound aptamer species.

As the concentration of TNFα in the sample changes, the intensities of the bound and unbound peaks should change proportionately.

Tumor necrosis factor α (TNFα) was chosen as a target for the continuous μFFE aptamer assay because of its dynamic role in cell-to-cell signaling. TNFα is a proinflammatory cytokine involved in essential immune response processes. The biologically active form of TNFα is a trimer (51 kDa), which is held together by noncovalent, primarily hydrophobic interactions between monomer (17 kDa) subunits.[281,282] Overactivation of TNFα signaling is associated with chronic inflammatory disorders including rheumatoid arthritis, Crohn's disease, psoriasis, and inflammatory bowel disease.[283] TNFα-binding antibodies and antibody fragments are used therapeutically to inhibit TNFα activity and manage inflammatory disease.[284–286] These therapeutic agents block receptor binding, stabilize the TNFα trimer and inhibit monomer exchange.[287,288] TNFα-binding aptamers have also been selected for therapeutic and sensing applications.[167,168,289–291]

Biological concentrations of TNFα vary widely depending on the cell type, cell line, stimulus, and sampling method used. Macrophages and other monocytes are the body's main producer of TNFα, and they are a common model for studying inflammatory processes.[292] TNFα secretion can be stimulated by lipopolysaccharide (LPS).[293,294] In studies of TNFα signaling, the most common method of detection and quantification is ELISA. LPS-stimulated macrophages can secrete TNFα at high concentrations. Multiple studies of murine RAW264 macrophages have reported TNFα concentrations exceeding 1 ng/mL in the cell supernatant, with some examples of TNFα exceeding 100 ng/mL.[294–296]

Without appropriate methods for continuous TNFα quantification, the exact temporal profile of the macrophages' response is unknown. However, ELISA-based quantification of noncontinuous samples has shown TNFα concentration increasing for several hours after stimulation and then plateauing.[294,295]

5.3 Experimental

5.3.1 Chemicals and reagents

Chemicals were purchased from Sigma-Aldrich (St. Louis, MO) unless otherwise specified. Buffers were prepared using deionized water (18.3 MΩ, Milli-Q; Millipore, Bedford, MA). TNFα (recombinant human, *E. coli*-derived) was purchased from R&D Systems (Minneapolis, MN), resuspended in low-NaCl PBS (100 mM NaCl, 2.7 mM KCl, 10 mM Na_2HPO_4, 1.8 mM KH_2PO_4, pH 7.4) and 0.01% Tween-20, and stored in aliquots at -20 °C.

μFFE separation buffer contained 25 mM HEPES and 300 μM Triton X-100, adjusted to pH 7.0 using 1 M NaOH and filtered through a 0.22 μm nitrocellulose filter membrane (Millipore). For separation buffer gradient experiments, the high-ionic strength separation buffer included an additional 50 mM NaCl.

5.3.2 Aptamer preparation and folding

Aptamers were purchased from Integrated DNA Technologies (IDT, Coralville, IA), resuspended in IDT's nuclease-free water, and stored in aliquots at -20 °C. Aptamers were folded immediately before use. To fold, aptamers were diluted in buffer, heated to 90 °C for 5 minutes, and cooled to room temperature on the benchtop for at least 15 minutes. Table 5.1 summarizes the sequences, folding buffers, and literature sources for all

aptamers. Folding Buffer A was PBS. Folding Buffer B was PBS supplemented with an additional 94.6 mM KCl (total KCl 100 mM). Folding Buffer C was PBS supplemented with 5 mM $MgCl_2$ and 2 mM $CaCl_2$. All folding buffers were adjusted to pH 7.4 and filtered using a 0.45 μm cellulose acetate syringe filter (Restek, Bellefonte, PA).

***Table 5.1**: Aptamer sequences*

	Sequence (5' → 3')	Buffer	Ref
VR11	/56-FAM/TGG TGG ATG GCG CAG TCG GCG ACA A	A	[289]
S01	/56-FAM/ATC CAG AGT GAC GCA GCA TGC TTA AGG GGG GGG CGG GTT AAG GGA GTG GGG AGG GAG CTG GTG TGG ACA CGG TGG CTT AGT	C	[167]
B01	/56-FAM/ATC CAG AGT GAC GCA GCA GGT TAA GGT GTA GGT CCG GGT GGG GGG GTG GGT TGG GGG ACT GGT GGA CAC GGT GGC TTA GT	C	[167]
aptTNF-α	/56-FAM/GCG CCA CTA CAG GGG AGC TGC CAT TCG AAT AGG TGG GCC GC	A	[290]
Apt05	/56-FAM/AAT TAA CCC TCA CTA AAG GGC GGA GTG GCG GGG GTG GGG GGC GGT CTA TA	B	[168]
Apt14-st	/56-FAM/GGG CGG GGG GAG GGC TGG TGG GGG GCG GCT	B	[168]
Apt14-linker	/56-FAM/TTT GGG CGG GGG GAG GGC TGG TGG GGG GCG GCT	B	

5.3.3 μFFE device fabrication

μFFE devices consisted of a 2.5 × 1 cm separation channel (depth: 40 μm) flanked on both sides by deeper electrode channels (depth: 400 μm), which each contained an embedded platinum wire (diameter: 0.1 mm). Devices were fabricated in cyclic olefin copolymer (COC) using a hot embossing process described by LeMon *et al*.[259] Figure 5.2 shows a finished COC μFFE device.

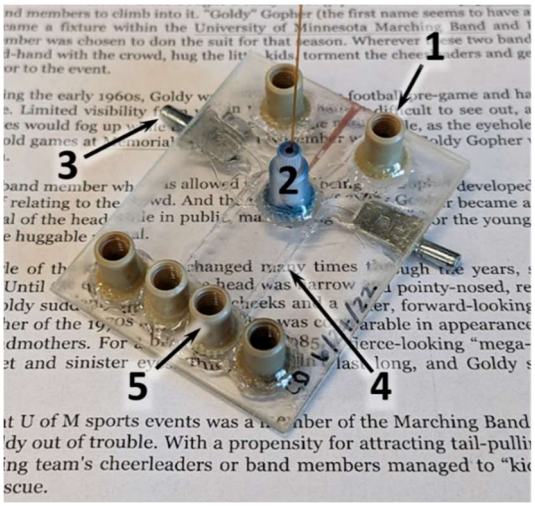

Figure 5.2*: A µFFE device fabricated in COC (total dimensions: 1.75 × 2.25 inches). Separation buffer enters the device through two inlets (1). Sample enters the device from a 20 µm I.D. capillary inserted perpendicular to buffer flow at the top of the 1 cm wide × 2.5 cm long × 40 µm deep separation channel (2). Platinum wire electrodes flank the separation channel, and a potential is applied at two reinforced terminals (3). Electrode channels (400 µm deep) remove electrolysis bubbles (4). Buffer leaves the device through four outlets (5).*

Briefly, a master mold was printed in Verowhite resin (Sculpteo Inc., Oakland, CA) using a Stratasys J750 Polyjet 3D printer (University of Minnesota Earl E. Bakken Medical Devices Center). An intermediate mold was then cast in Silastic polymer (RTV-3110, with Xiameter RTV-3010S catalyst, Dow, Midland, MI), and the final hot embossing mold was subsequently cast in Weicon C (Weicon, Ontario, Canada).

The features on the Weicon C mold were embossed on TOPAS 6017s-04 COC (TOPAS, Raunheim, Germany) substrates using a Carver thermal press (Wabash, IN) with an embossing temperature of 185°C, a load of 1000 pounds, and a de-embossing temperature of 173°C. After embossing, substrates were flattened at 149°C under a load of 100 pounds and clarified during a 30-minute exposure to cyclohexane vapor.

Wire electrodes were embedded in the electrode channels, and the embossed COC substrate was bonded to an un-embossed COC cover plate with pre-drilled access holes.

The un-embossed plate was exposed to room-temperature cyclohexane vapor for 34 minutes, and the embossed substrate was exposed for 9 minutes. The two pieces were aligned and bonded at 93°C under a load of 250 pounds for 30 minutes.

Inlets and outlets for the separation buffer were accessed using NanoPorts (Upchurch Scientific, Oak Harbor, WA) aligned with 1 mm holes in the cover plate. Separation buffer was introduced from 1/16 in. O.D., 0.04 in. I.D. Tefzel tubing (IDEX, Lake Forest, IL) The sample was introduced from a 360 μm O.D., 20 μm I.D. capillary inserted through a 400 μm hole in the cover plate. Sample left the capillary and met the flowing separation buffer at a 90° angle. The sample capillary was held in place using a 380 μm I.D. NanoPort.

5.3.4 LIF detection

On-chip laser-induced fluorescence (LIF) detection was performed using a 488 nm diode pumped solid state laser (Sapphire, Coherent, Santa Clara, CA). The beam was expanded to a ~2.5 cm by 150 μm line and positioned across the width of the μFFE separation channel. In most experiments, fluorescence was detected using a Prime BSI Express camera (Teledyne Photometrics, Tucson, AZ) mounted on an SMZ1500 stereomicroscope (Nikon, Tokyo, Japan) with a 1.6× objective (Nikon). In experiments with a separation buffer gradient, the camera was mounted on a Nikon AZ 100 stereomicroscope with a 0.5× objective. All separations were imaged using an exposure time of 500 milliseconds. A dichroic mirror (495 nm cutoff), and a 500-550 nm band pass filter were used to remove extraneous wavelengths.

5.3.5 Data analysis

Images were acquired using μManager,[272] and fluorescence intensity across the detection zone was tabulated using ImageJ.[273] Subsequent data analysis was performed using custom Matlab scripts.

5.3.6 μFFE separations for aptamer screening

To screen sequences for binding and μFFE separation, aptamers were folded and incubated with TNFα in the buffers described in Table 5.1. In initial screening separations, aptamers were folded in 2× strength buffer and incubated in 1× strength buffer. In low-salt screening separations, a subset of aptamers (S01, B01, Apt05, and Apt14-st) were folded in 0.2× strength buffer and incubated in 0.1× strength buffer.

The folded aptamer was mixed with TNFα in an opaque microtube (Argos Technologies, Vernon Hills, IL) and incubated at room temperature for at least 15 minutes. The incubated sample was loaded into a gastight syringe (Hamilton, Reno, NV) and flowed into the μFFE device at a rate of 500 nL/min using a Harvard Apparatus (Holliston, MA) syringe pump. Separation buffer was flowed through the device at a rate of 3 mL/min using 140 mL syringes on a second syringe pump (Harvard Apparatus). Potentials from +50 V to +150 V were applied in 70-second pulses.

5.3.7 Additional aptamer separations

Apt14-linker was folded in 0.426× Buffer B and incubated for at least 15 minutes with varying concentrations of TNFα to generate a standard curve. The buffer composition was 0.16× Buffer B + 0.01% Tween-20 during incubation and separation. Samples were injected onto the μFFE device at a flow rate of 500 mL/min. The sample capillary was

treated with polyethylene oxide (PEO) to prevent surface adsorption. Separation buffer entered the μFFE device at 3 mL/min. Potentials of +75 V, +100 V, and +125 V were applied in 70-second pulses. Rhodamine 110 (50 nM) was used as an internal standard.

Apt14-linker was folded in buffers of varying strength, ranging from 0.2× Buffer B (total monovalent cation concentration 40 mM) to 1.54× Buffer B (260 mM) to determine the effect of aptamer buffer strength on assay performance. The folded aptamer was incubated with TNFα, and samples were separated and detected using μFFE. The final sample concentrations were 1 μM Apt14-linker, 400 nM TNFα, 0.01% Tween-20, 50 nM rhodamine 110, and 0.08× - 0.31× Buffer B.

5.3.8 Separation buffer gradient

To create gradients in the composition of the separation buffer, a pressure-driven microfluidic flow controller and ESI software (Elveflow, Paris, France) were used to flow separation buffer from two reservoirs into the device. Reservoirs containing 25 mM HEPES, 300 μM Triton X-100, and 50 mM NaCl or 0 mM NaCl, respectively, were attached to the controller, and programmed flow rate gradients were used to control each reservoir channel. Buffers from the two channels met at a PEEK mixing tee (IDEX) before flowing into the buffer inlet of the μFFE device. The total flow rate was held constant at 3 mL/min.

5.3.9 TNFα injections

To test the temporal response of the assay, plugs of TNFα were injected, incubated with aptamer, and separated in a continuous online system. Figure 5.3 shows the fluidic setup used for injection, incubation, and separation. A 6-way HPLC valve (Vici Valco,

Houston, TX) was used to switch flow between buffer and a solution containing TNFα and rhodamine 110. Flow from the valve entered a PEEK tee (IDEX, inner diameter 50 µm), where it mixed with a constant flow of aptamer solution. The mixture equilibrated and incubated in a 30 cm length of PEO-treated fused silica capillary (inner diameter 150 µm) before flowing into the µFFE device for separation and detection.

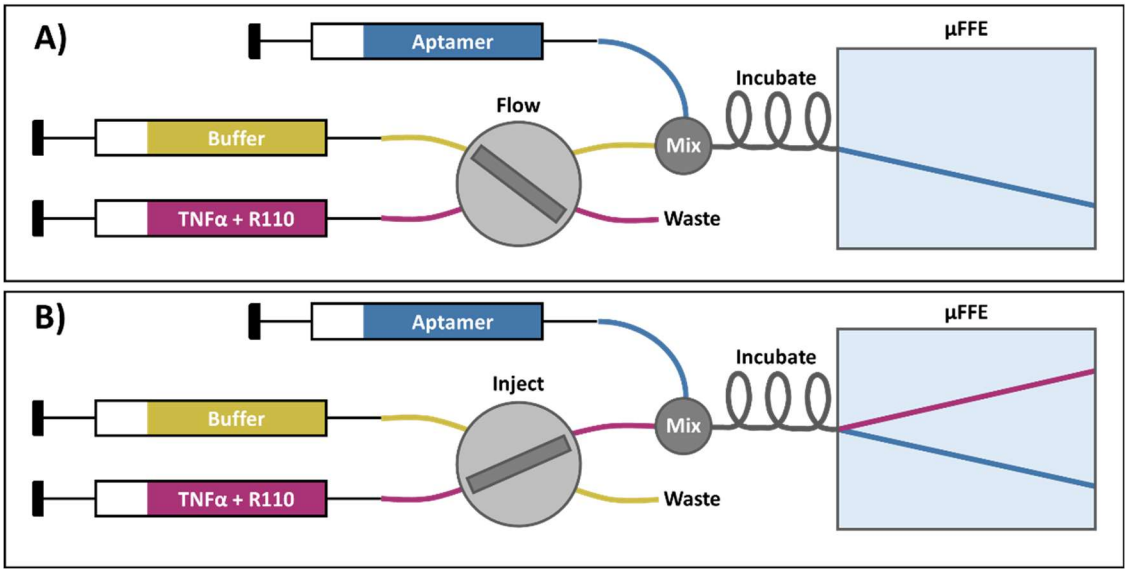

***Figure 5.3**: Diagram of TNFα injection fluidics. A) At rest, buffer flows through the valve and meets the flowing aptamer solution at a mixing tee. The two solutions equilibrate and incubate for ~15 minutes in a 30 cm segment of fused silica capillary (inner diameter 150 µm) before entering the µFFE device for separation and detection. B) During injection, a mixture of TNFα and rhodamine 110 flow through the valve and meet the aptamer solution at the mixing tee.*

5.4 Results and Discussion

5.4.1 Aptamer screening

A total of six literature-reported aptamer sequences (Table 5.1) were screened using µFFE separations. In the absence of TNFα, a single µFFE peak is expected, representing the unbound, fluorescently-labeled aptamer. As increasing concentrations of TNFα are incubated with the aptamer, an increasing fraction of the aptamer is expected to bind to the

protein. In a noncompetitive μFFE assay, the bound and unbound aptamer species must have sufficient differences in electrophoretic mobility to be separated by μFFE. Ideally, a distinct peak representing the bound aptamer species will appear as TNFα is added to the aptamer. However, for all six aptamer sequences screened, the bound aptamer species was either not present, not detectable, or not resolved in initial μFFE separations.

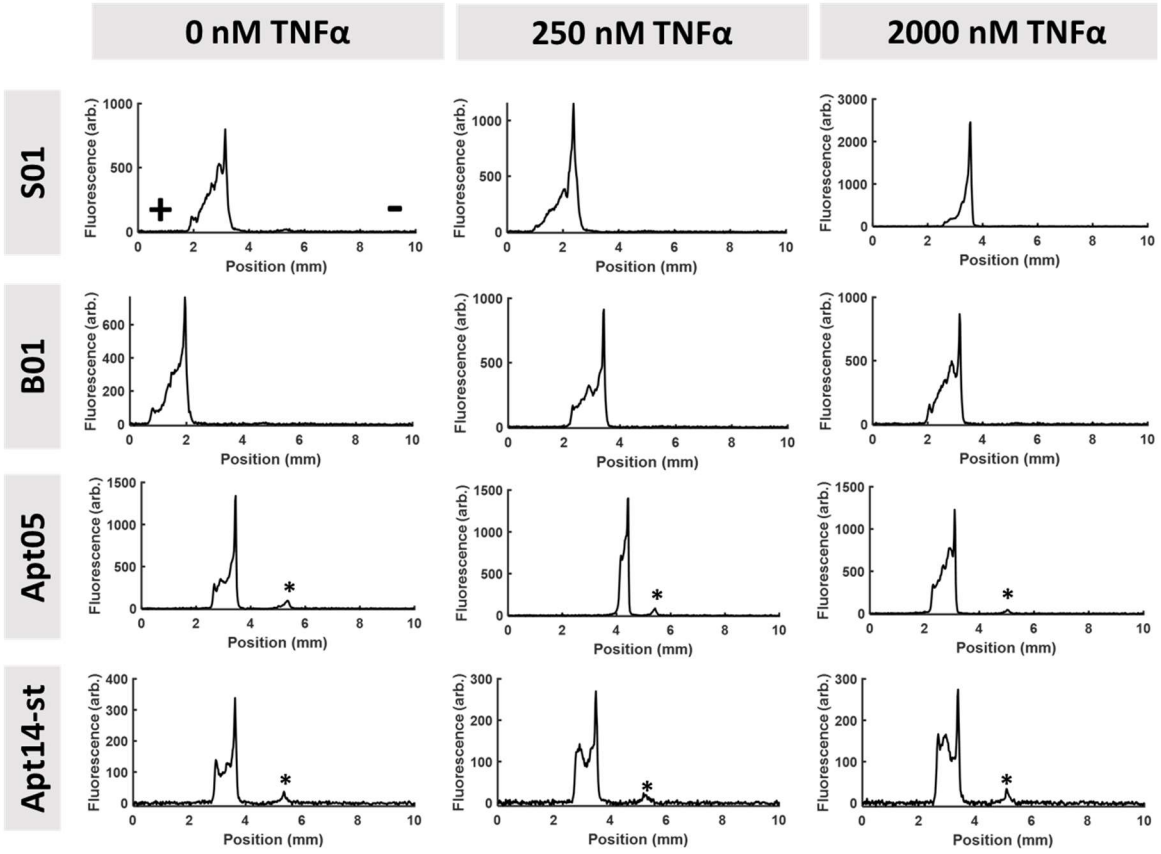

***Figure 5.4**: μFFE separations of 500 nM S01, B01, Apt05, and Apt14-st aptamer incubated with 0 nM, 250 nM, or 2000 nM TNFα under an applied potential of 125 V (anode on left). Plots show fluorescence across the width of the separation channel. Asterisk (*) indicates contaminant peak.*

Figure 5.4 shows example traces for four aptamers incubated with 0 nM, 250 nM, or 2000 nM TNFα under an applied potential of 125 V. A single peak was observed for all aptamers. Although a contaminant peak was detectable in the Apt05 and Apt14-st separations, the peak was present in the control sample with no TNFα, and its intensity did

not change with increasing concentrations of TNFα. It was likely caused by carryover from previous dye separations.

All aptamer peaks were asymmetric, and the aptamer was sharply concentrated on the tailing (cathode-side) edge of the sample zone. This dramatic deviation from the symmetric, Gaussian peak shapes usually observed in μFFE separations was caused by a conductivity mismatch between the high-salt sample buffer and the low-salt separation buffer filling the μFFE channels. If the mismatch is too severe, it may interfere with the separation and detection of the bound aptamer species.

To address this concern, the ionic strength of the aptamer folding buffer was reduced to more closely match the strength of the separation buffer. Four of the six aptamer sequences were screened again in low ionic strength aptamer buffer. Buffer strength was reduced 10-fold during aptamer folding and incubation with TNFα. As predicted, there was a significant change in the shape of the unbound aptamer peak. With a smaller conductivity mismatch, the aptamer peak was more symmetric and had a less intense peak front. After decreasing the strength of the folding buffer, a second peak appeared for one of the four aptamers, a sequence named Apt14-st (Figure 5.5).[168] The intensity of the peak increased with increasing concentrations of TNFα, suggesting that it corresponds to the protein-bound aptamer species.

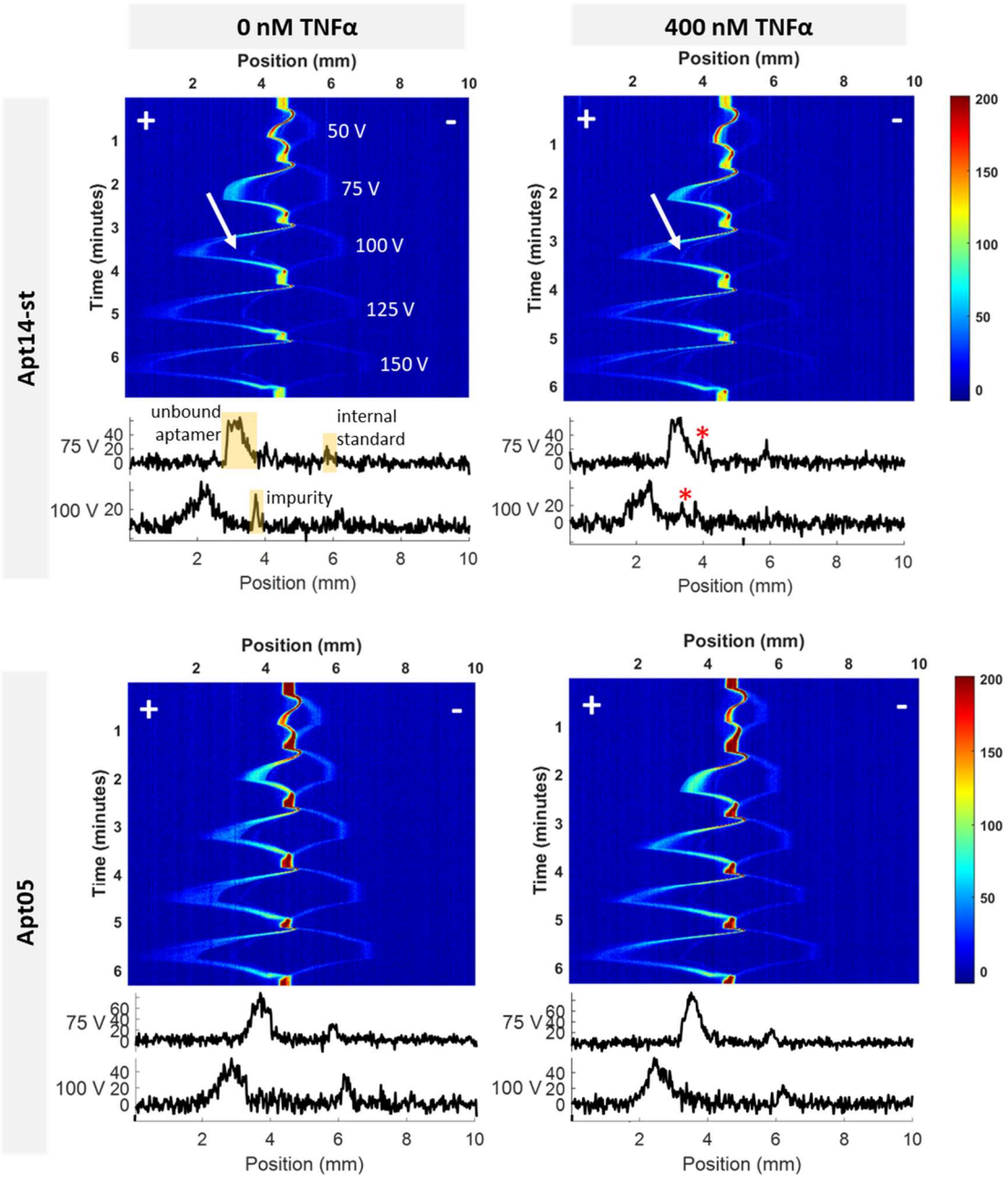

***Figure 5.5**: Aptamer screening data for 1 μM Apt14-st (top) and 0.2 μM Apt 05 (bottom) folded in low-strength buffer. Aptamers were incubated with no TNFα (left) or 400 nM TNFα (right) as well as trace rhodamine 110 (internal standard). 3D plots show fluorescence across the separation channel over the course of a 6-minute separation where voltage was applied in pulses from 50 to 150 V. 2D plots show fluorescence across the separation channel with 75 V and 100 V applied, respectively. The unbound aptamer peak, internal standard (rhodamine 110) peak, and an impurity peak appear in all separations. The bound aptamer peak (arrow, *) is present only when Apt14-st is incubated with TNFα.*

5.4.2 Increasing aptamer signal

The fluorescence intensity of Apt14-st was approximately ten-fold lower than the intensity of other FAM-labeled aptamers from the same synthesis batch (Figure 5.6). An explanation for this low signal lies in the sequence of the oligonucleotide. Table 5.1 shows the sequences of all six aptamers screened. Many of the sequences are guanine-rich, likely because their three-dimensional structures are stabilized by guanine quadruplexes.[297] However, Apt14-st is the only sequence with a FAM label directly adjacent to the guanine-rich region. Electron transfer between guanine and adjacent fluorophores is a well-known quenching mechanism, and can result in a significant decrease in fluorescence intensity.[298,299]

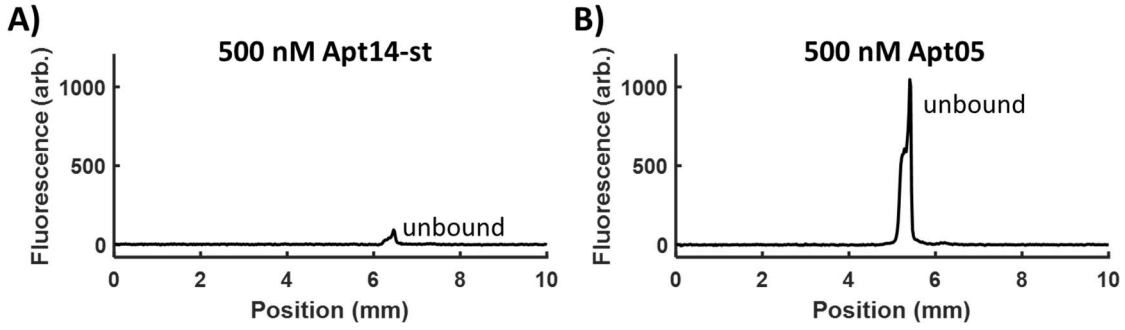

Figure 5.6*: µFFE peaks for 500 nM Apt14-st (A) and 500 nM Apt05 (B) demonstrate guanine quenching of the 5' FAM fluorophore. The fluorescence intensity of guanine-quenched Apt14-st is 10-fold lower than that of Apt05.*

To mitigate quenching and increase the fluorescence intensity of Apt14-st, a three-nucleotide thymine linker was added between the 5' FAM label and the beginning of the aptamer sequence. This updated aptamer, named Apt14-linker, had approximately 4-fold higher fluorescence than the original Apt14-st sequence (Figure 5.7). The linker increased the intensity of both the bound and unbound aptamer peaks, enabling more sensitive detection of TNFα with lower input and consumption of aptamer.

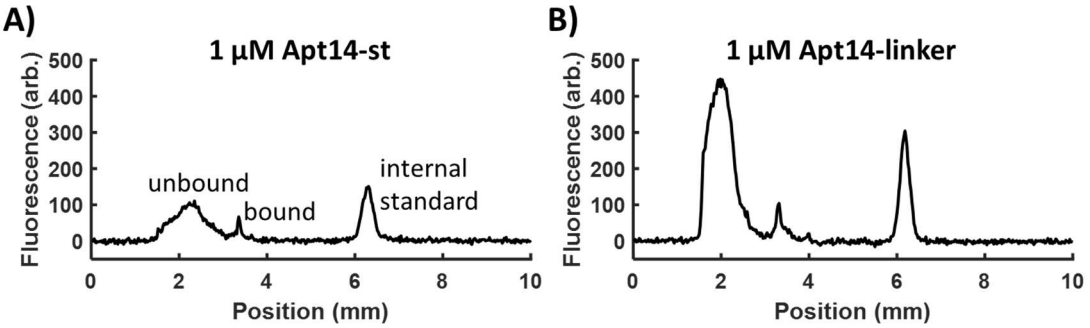

Figure 5.7*: µFFE separations of 1 µM Apt14 (A: without linker and B: with linker) with 400 nM TNFα and rhodamine 110 internal standard. A thymine linker between the 5' FAM and 5' guanine increases aptamer fluorescence 4-fold.*

5.4.3 Standard curve

A standard curve was generated to assess the response of the µFFE aptamer assay to increasing concentrations of TNFα and to determine the lower limits of TNFα detection. Figure 5.8A shows a series of µFFE separations after Apt14-linker was incubated with 0 nM to 800 nM TNFα. As the concentration of TNFα increased, the fluorescence intensity of the bound aptamer peak increased relative to the unbound aptamer peak. Figure 5.8B shows the relationship between the height ratio of the bound and unbound aptamer peaks and the concentration of TNFα in the sample. The assay responded predictably and linearly to TNFα, and the lowest concentration of TNFα detected was 100 nM, or approximately 1.7 µg/mL.

As expected, the µFFE aptamer assay is substantially less sensitive than commercial well-plate ELISAs for TNFα. Traditional ELISA assays detect TNFα concentrations in the range of approximately 10 to 1000 pg/mL, and high-sensitivity ELISA methods can decrease the limit of detection to around 0.1 pg/mL. ELISAs achieve this sensitivity by coupling an antibody with a signal-amplifying enzyme. For every

molecule of analyte present, the enzyme produces many-fold more fluorescent or colored product molecules.

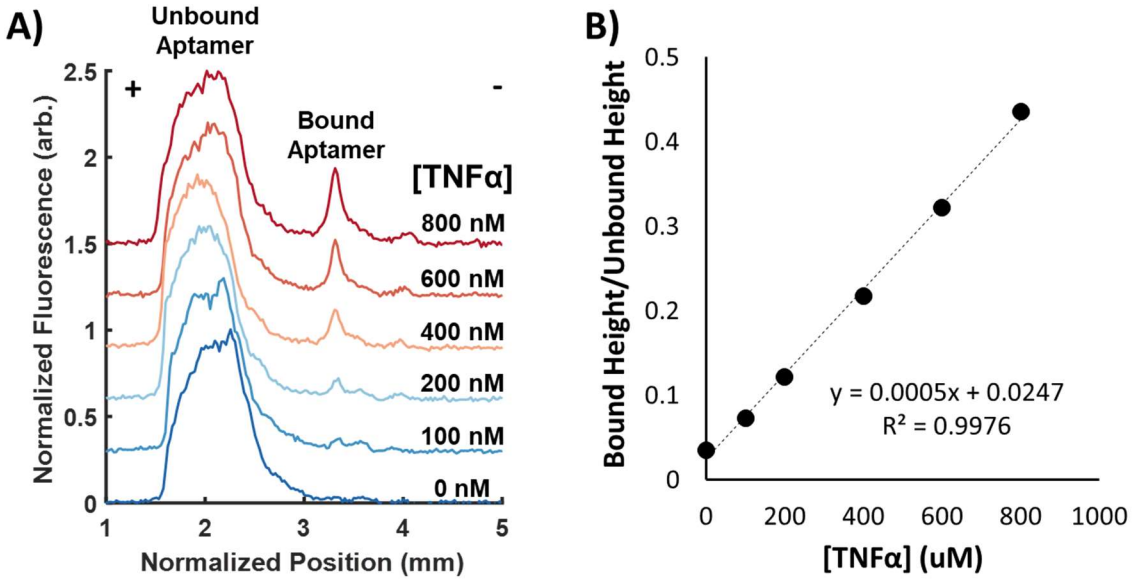

***Figure 5.8**: A) µFFE separations of 1 µM aptamer with 0 to 800 nM TNFα at 100 V (anode on left). Position and intensity are normalized to the position and height, respectively, of the unbound aptamer peak. B) Standard curve for aptamer µFFE assay.*

Because the µFFE aptamer assay presented here includes a single fluorophore label per analyte molecule, its limit of detection will be high compared to ELISAs and other high-sensitivity affinity assays. However, the goal of the µFFE assay is not to compete with ELISAs but rather to offer a framework of complementary information. While ELISAs quantify low-abundance targets in a discrete sample, the µFFE assay will quantify dynamic changes in target concentration over time. Macrophages can secrete TNFα at levels exceeding 100 ng/mL (~6 nM).[294–296] After optimization of the aptamer assay, fluidics, and cell perfusion method, we expect the µFFE affinity platform to be capable of measuring biologically relevant changes in TNFα concentration.

5.4.4 Optimizing the aptamer assay

The effects of buffer strength on peak shape and height were assessed to improve the sensitivity of the μFFE aptamer assay. Figure 5.9 shows the height ratio of the bound and unbound aptamer peaks in μFFE separations where the aptamer was folded in buffers of varying ionic strength. Apt14-linker was folded in a phosphate buffer containing a combined Na^+ and K^+ concentration of 40 mM to 260 mM and incubated at room temperature with 400 nM TNFα.

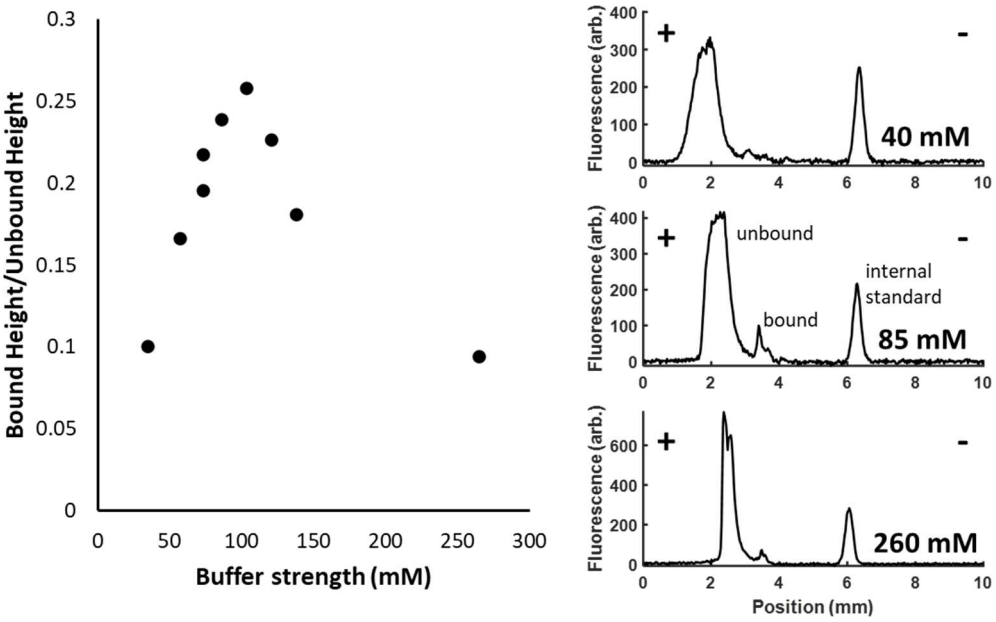

Figure 5.9*: Optimal ionic strength (85 mM) for the folding buffer used in the μFFE aptamer assay with 1 μM aptamer and 400 nM TNFα. Representative linescans show fluorescence intensity across the separation channel for aptamers folded at low (40 mM), optimal (85 mM), or high (260 mM) ionic strength. The ionic strength during incubation and separation is 0.5× the folding buffer strength. The applied potential was 100 V (anode on left).*

The optimal ionic strength of the aptamer folding buffer was between 80 and 100 mM monovalent cations (Na^+ and K^+). At low ionic strengths (40 mM), the bound aptamer peak is broad and has low intensity. Aptamers are selected in relatively high-strength buffers and use cations to stabilize both their structural conformations and their ligand

interactions. When the aptamer is folded and incubated in a low-strength buffer, it is unlikely to bind the target effectively.

At high ionic strengths (260 mM), the shapes of the bound and unbound aptamer peaks become irregular, and resolution between the two decreases. The dramatic change in peak shape is caused by the difference in ionic strengths between the sample buffer and the separation buffer that fills the μFFE device. Consistent with the results of aptamer screening experiments, high salt concentrations in the sample buffer interfere with the μFFE separation and complicate resolution and identification of the bound aptamer peak.

The strength of the μFFE separation buffer also has a dramatic effect on peak shape. In most μFFE experiments, it is advantageous to use a low-strength separation buffer because high conductivity buffers increase electrolysis at the electrodes. The resulting bubble formation interferes with flow through the separation channel. For this reason, aptamer screening experiments and initial optimization experiments used a separation buffer containing 25 mM HEPES and 300 μM Triton X-100 (a nonionic surfactant) with no additional salts.

To assess the effects of separation buffer strength on aptamer peak shape, a gradient was created in the separation buffer with increasing NaCl concentration over time. This approach capitalizes on the continuous nature of μFFE separations to rapidly screen a wide range of separation conditions. For example, with a 5-minute gradient of continuously increasing NaCl concentration and a data acquisition rate of 2 frames per second, we can monitor the separation at 600 unique concentrations.

Two buffer reservoirs, one containing normal separation buffer and one containing separation buffer with 50 mM NaCl, were connected at a mixing tee that flowed into the μFFE device's buffer inlet. The total ionic strength of the separation buffer was controlled by changing the flow rates of the salt-free and 50 mM NaCl buffers. Flow was controlled using an Elveflow controller, and the flow rate of each buffer channel was independently monitored using a flow sensor.

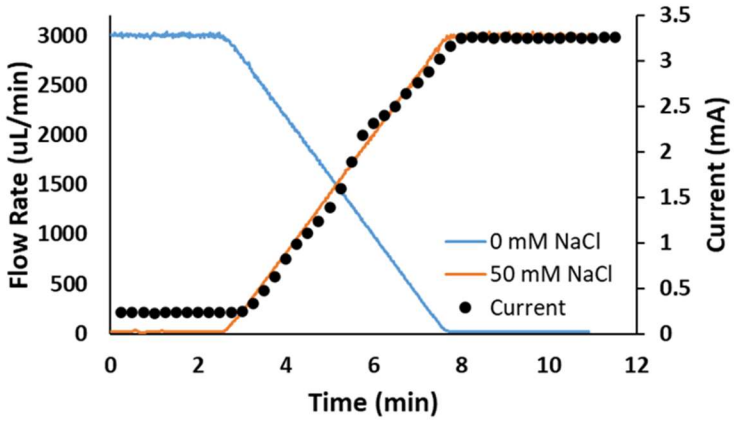

***Figure 5.10**: Gradient of increasing NaCl in the μFFE separation buffer. The flow rate of separation buffer containing 50 mM NaCl (orange line) was increased while the flow rate of buffer containing 0 nM NaCl (blue line) was simultaneously decreased. The current (black points) in the device was recorded over the course of the gradient.*

Figure 5.10 shows an example of a separation buffer gradient with increasing ionic strength over time. The flow rate of the 50 mM NaCl buffer increased from 0 to 3 mL/min while the flow rate of the salt-free buffer simultaneously decreased from 3 to 0 mL/min over a period of 5 minutes. The total flow rate was held constant at 3 mL/minute. A constant separation voltage of 50 V was applied throughout the separation, and the current in the separation channel was recorded every 15 seconds. Since electrical conductivity increases with ionic strength, the current increased proportionately with increasing concentrations of NaCl in the separation buffer. There was a 35-second delay between the start of the flow

rate gradient and the first measured change in current, which reflects the transit time between the mixing tee and the separation channel.

Figure 5.11 shows the shape of the Apt14-linker aptamer peak over the course of the separation buffer gradient. The monovalent cation concentration in the aptamer sample buffer was 33.5 mM. At the beginning of the gradient, the conductivity of the sample was much higher than the conductivity of the surrounding separation buffer. At the end of the gradient, the conductivity of the sample was slightly lower than that of the surrounding buffer.

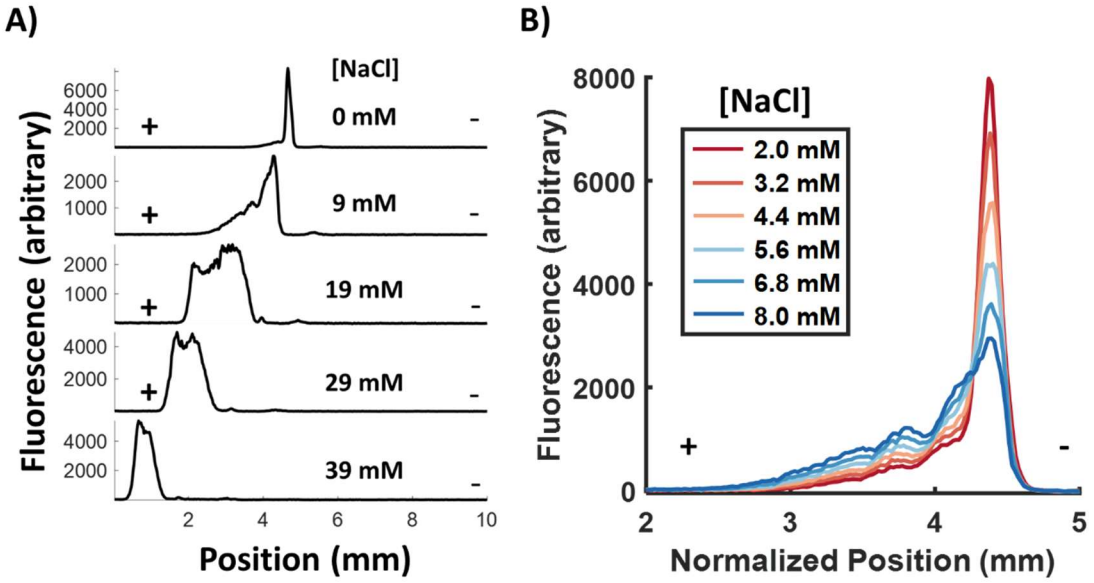

***Figure 5.11**: 2.7 µM Apt14-linker in 33.5 mM sample buffer detected by µFFE under a separation potential of 50 V (anode on left). Over the course of the separation, a gradient of increasing NaCl was applied to the µFFE separation buffer. A) Extracted linescans show the shape of the unbound aptamer peak with 0-39 mM NaCl in the separation buffer. B) Overlaid linescans with 2-8 mM NaCl in the separation buffer. Position normalized to remove electrolysis drift.*

Fluorescence intensity across the width of the separation channel was extracted at several points over the course of the gradient. When the conductivity mismatch was highest (0 mM NaCl in the separation buffer, 33.5 mM in the sample buffer), the aptamer was

strongly concentrated on the tailing (cathode-side) boundary between the sample buffer and separation buffer.[300,301] The aptamer peak was narrow and intense, with some low-intensity signal stretching toward the anode. As the concentration of NaCl in the separation buffer increased, the maximum intensity of the peak decreased, and the aptamer was increasingly distributed toward the anode (Figure 5.11B). By 19 mM, the aptamer peak was square and broad. The width of the peak decreased as the NaCl concentration increased from approximately 20 to 50 mM.

The position of the aptamer peak also shifted toward the anode over the course of the gradient. This was driven partially by the accumulation of electrolysis bubbles, but stacking and destacking effects also caused the peak maximum to move toward the anode as the strength of the separation buffer increased because the peak grew increasingly symmetric.

When the separation buffer strength was high, a small peak appeared to the right of the unbound aptamer peak. Although it occurred near the position where the bound aptamer peak is often found, its intensity did not change with changing concentrations of TNFα. The sample separated in Figure 5.11 contained no TNFα.

The plots shown in Figure 5.11 represent only a small fraction of the complete data set. In only five minutes, the separation buffer gradient captured changes in aptamer peak shape across 600 different buffer strengths. The gradient was an efficient approach to μFFE optimization for an application that is especially sensitive to changes in the composition, strength, and pH of the separation buffer. After a more thorough optimization of aptamer folding and incubation parameters, separation buffer gradients can be used to separate

samples containing both aptamer and TNFα. These experiments will identify the precise separation conditions that yield the greatest separation and signal of the bound aptamer peak.

5.4.5 Temporal response of the aptamer assay

The distinguishing feature of the μFFE aptamer assay compared to existing affinity assays is its potential for continuous measurement of a dynamic sample. To assess the temporal response of the aptamer assay, plugs of TNFα were injected into a continuously flowing stream of aptamer solution (see fluidic setup, Figure 5.3). In an aptamer assay with fast temporal response, we expect to see a single, unbound aptamer peak under rest conditions. When TNFα is injected, it should mix with and be bound by the aptamer, producing a second, bound peak during detection.

Figure 5.12 shows three replicate injections of 1.9 μM TNFα and 0.3 μM rhodamine 110. The injection plug met a continuous flow of 4 μM aptamer, was incubated for approximately 13 minutes as it flowed to the device, and was separated under an applied potential of 100 V. The first two injection plugs were one minute long, and the third was 30 seconds long. There were two minutes of buffer flow between each plug. Before the first plug, there was one large peak in the separation channel representing the unbound aptamer (Figure 5.12B). The arrival of each plug is clearly marked by the appearance of a rhodamine 110 peak. However, there was no clear peak corresponding to the TNFα-bound aptamer species.

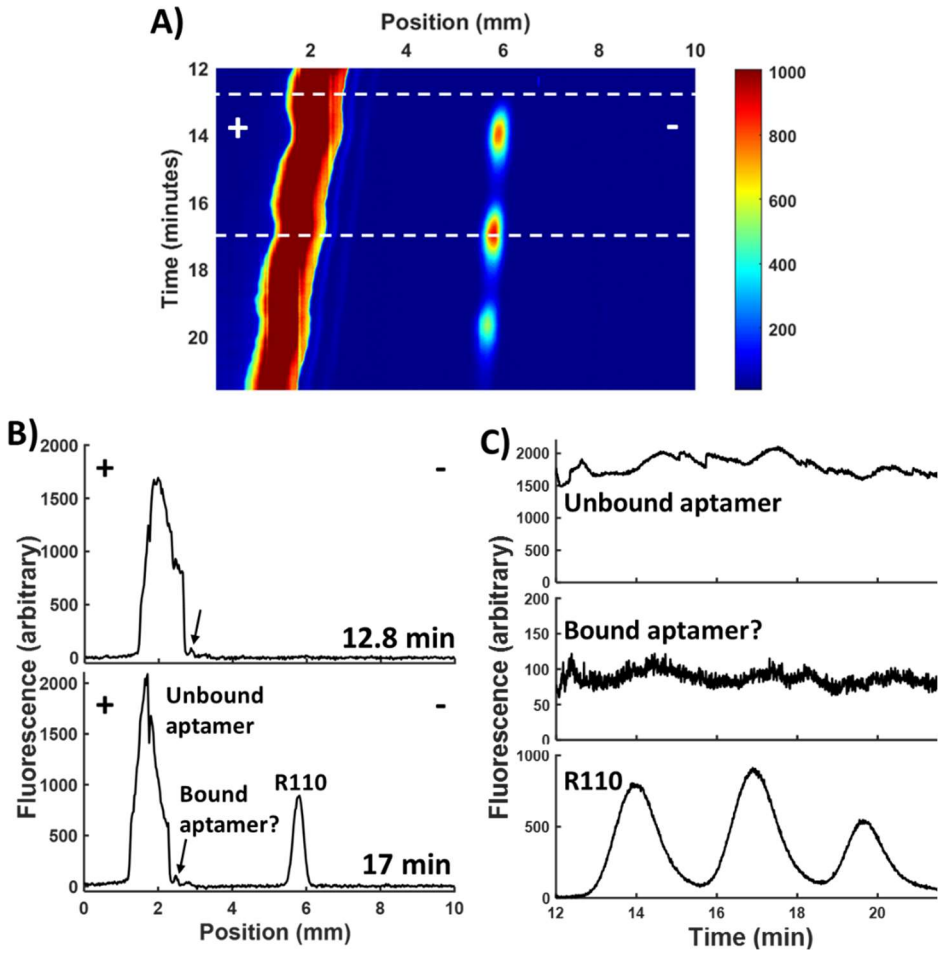

***Figure 5.12**: Injection of 1.9 µM TNFα and 0.3 µM rhodamine 110 into a continuous flow of 4 µM Apt14-linker. A) Three-dimensional plot of µFFE separation at 100 V (anode on left). Dotted lines indicate timepoints shown in linescans. B) Extracted linescans extracted at 12.8 minutes (before first plug) and 17 minutes (during second plug). The first plug was injected at t = 0 minutes. C) Extracted fluorescence intensity profiles for the unbound aptamer, bound aptamer, and rhodamine 110 over a 10-minute detection period.*

Figure 5.12C shows the fluorescence intensity over time for the unbound aptamer peak, the rhodamine 110 peak, and a small peak in the position where the bound aptamer peak is expected to occur. As expected, the intensity of the unbound aptamer peak is relatively constant. Slight increases and decreases in signal do not correspond to the timing of the injection sequence, and they are better explained by changes in flow stability and

device clarity as electrolysis causes a slow shift in peak position. There were three temporal peaks at the rhodamine 110 position, corresponding to the three injected plugs. The rise and fall time of the rhodamine 110 peaks was approximately 2 minutes. Surface adsorption and diffusion in the incubation capillary both contribute to temporal broadening of the one-minute injection plugs.

There was no significant change in the intensity of the putative bound aptamer peak over time. A possible explanation for poor temporal response to TNFα injection is surface adsorption as the protein travels from the valve to the separation channel. To reduce adsorption effects, the experiment was repeated with 1 μM TNFα in the constantly-flowing buffer solution and 5 μM TNFα in the injection solution. The higher concentration of background TNFα was intended to coat any adsorption-prone surfaces before they were exposed to the high-TNFα plug. In this experiment, there was still a small peak in the bound aptamer position, but it was again unresponsive to TNFα injections.

Alternatively, it is possible that the small peak represents an impurity present in the aptamer solution. The absence of a bound aptamer peak would indicate a more fundamental issue with reagent stability, preparation, and incubation. Improved reproducibility is a key goal of future μFFE aptamer assay development.

5.5 Conclusion

These results demonstrate significant progress toward a continuous, aptamer-based affinity assay using μFFE. An aptamer was identified that demonstrates a large shift in electrophoretic mobility upon binding to TNFα. The bound and unbound aptamer species can be continuously separated using μFFE, and TNFα concentrations as low as 100 nM

can be distinguished from background signal. The ionic strength of the aptamer folding buffer plays an important role in both binding and separation. The composition of both the sample buffer and separation buffer were varied to explore the relationship between ionic strength, conductivity, peak shape, and assay signal. In addition, plug injections assessed the temporal response of the μFFE platform, which demonstrated fluorescent dye rise and fall times on the order of minutes.

Future work will focus on improving the reproducibility and sensitivity of the assay. The aptamer binding equilibrium and separation are both sensitive to a number of parameters, including buffer strength and composition, folding conditions, incubation conditions, reagent storage, and fluid dynamics in the device. Additional optimization and control of each parameter will improve the relative signal of the bound aptamer peak and decrease variability between experiments.

The initial performance of the aptamer assay demonstrates potential for continuous TNFα monitoring. The ultimate objective of the assay is to couple the μFFE device with immune cells in a perfusion chamber to measure dynamic cellular responses to inflammatory stimuli. A successful μFFE aptamer assay would report continuous protein quantification profiles at timescales that are impractical or impossible to investigate using discrete affinity assays.

Chapter 6: Summary and outlook

6.1 Summary

Microfluidic platforms are fast, sensitive, and exceptionally customizable. They can be tailored to collect data at physical scales and time scales that would be inaccessible by other techniques. This thesis described the development of two microfluidic platforms to investigate biological questions that commercial instruments and well-established methods are poorly suited to address. Chapters 2 and 3 described progress toward a droplet microfluidic platform capable of quantifying the abundance of catalytic oligonucleotides in libraries of random-sequence DNA – a frequency that may be on the order of one per trillion or lower. Chapters 4 and 5 described the development of continuous affinity assays using micro free-flow electrophoresis (μFFE) – a technique designed to gather novel temporal information about a wide range of biologically relevant molecules and processes. Altogether, the previous chapters detailed significant advances in the design, operation, and technical performance of both platforms, as well as the chemistry occurring inside them. However, opportunities remain to fine tune both applications and expand their impact.

In Chapter 2, a droplet microfluidic platform was developed for the quantification of catalytic oligonucleotides in random-sequence libraries. The platform was used to screen libraries of 90-nucleotide, fully random DNA sequences for catalytic activity after incubation with two sugar substrates and an RNA substrate. An upgrade from the initial capillary-based platform to custom PDMS devices reduced the droplet volume, noise, and detection threshold while maintaining a screening rate of over 30 billion molecules per second. Although the PDMS platform was theoretically capable of detecting catalysts with

rate constants as low as k_{cat} = 0.07 reactions per second, there was no evidence of DNA-catalyzed cleavage of any of the three substrates studied. This result could indicate either a meaningful threshold of catalyst abundance or an underlying limitation in the design and operation of the droplet microfluidic platform.

In Chapter 3, the 10-23 DNAzyme, a well-studied RNA-cleaving DNA catalyst,[34,241,252] was used to evaluate the droplet microfluidic platform's suitability for oligonucleotide catalyst detection. The DNAzyme's activity in low-volume reactions in a 364-well plate was consistent with reported kinetic parameters. Activity persisted at a stable rate over the course of a 20-hour incubation, demonstrating high DNAzyme turnover. However, the DNAzyme did not catalyze RNA substrate cleavage when the same reaction was performed in droplets. This work established a control system for monitoring oligonucleotide catalyst activity in droplets and identified areas for further investigation and optimization before more DNA catalyst screening experiments should proceed. The droplet interface will be the primary focus of future platform development.

In Chapter 4, the surface chemistry of cyclic olefin copolymer (COC) devices was characterized using two-dimensional nLC-μFFE separations. Small molecule adsorption on the COC surface was significantly lower than in previously studied glass or ABS devices, regardless of the net charge of the molecule.[188,189] Protein adsorption was slightly higher in COC devices than in ABS devices, but it was much lower than in glass devices. Proteins fully desorbed from the COC surface on timescales of several minutes, and no additional treatments were required to strip adsorbed proteins. Triton X-100, a surfactant added to the running buffer during μFFE separations, reversibly modified the COC surface.

It decreased electroosmotic flow and had minimal effect on protein adsorption. This suggests that the COC surface, which was expected to be hydrophobic and neutral, acquired charge during fabrication or operation. The surface charge appeared to be masked by the Triton X-100. The relatively low protein adsorption was a characteristic of the COC surface itself, and Triton X-100 was not required to prevent adsorption.

In Chapter 5, an aptamer-based μFFE assay was developed for continuous quantification of tumor necrosis factor alpha (TNFα). The assay was able to detect TNFα concentrations as low as 100 nM. The effects of sample buffer and separation buffer strength on aptamer peak shape were assessed, and the temporal response of the assay was investigated using online injections of TNFα. Future work will focus on optimizing the aptamer assay and integrating it into an online system for continuous biological monitoring.

6.2 Future Work: Quantification of Catalytic Oligonucleotide

Future work on the catalytic oligonucleotides project will investigate the activity of known DNAzymes in small reactions and droplets. Insights can be applied to improve the droplet microfluidic platform or design an alternative microfluidic array for oligonucleotide library screening. Ultimately, the improved platform could be used to screen a wide range of libraries, substrates, and reaction conditions for catalytic activity.

6.2.1 Investigating 10-23 DNAzyme activity in droplets

The control experiments detailed in Chapter 3 produced an unexpected outcome: the 10-23 DNAzyme worked in small-volume reactions in a well plate, but it did not work in droplets. Future work will investigate that result with a particular focus on the droplet interface, the most significant difference between the two reaction environments. Does the

DNAzyme cleave the substrate when both are introduced at higher concentrations? Does it work in larger droplets? In smaller wells? Confocal microscopy techniques could reveal the localization patterns of DNAzyme, substrate, and cleaved product, which could help diagnose interface effects. For example, is the DNA concentrated around the perimeter of the droplet? Does droplet size, oil composition, or surfactant identity influence the uniformity of reactant, salt, or product distribution? If we can identify a precise explanation for the differing DNAzyme activity in wells and droplets, we could improve the platform to make it compatible with library screening. Any lessons learned would also be broadly relevant to other droplet microfluidic and nucleic acid catalyst applications.

6.2.2 Alternative microarray approaches

If future experiments identify droplet interface interference with DNAzyme activity, there are a number of ways to modify the interface or eliminate it entirely. A variety of fluorinated oils and surfactants have been developed and marketed for droplet microfluidics (see section 1.3.2).[95] Among commercial surfactant and stabilizer systems, there are ionic and nonionic molecules, a range of different polymeric structures, and non-polymeric nanoparticles. The identity of the surfactant in the Bio-Rad droplet generation oil used in Chapters 2 and 3 is proprietary. However, it should be possible to fundamentally change the chemistry of the droplet interface if needed. There is a significant literature precedent for nucleic acid applications in microfluidic droplets, so it is reasonable to expect an existing oil/surfactant system to be compatible with DNAzymes.

Alternatively, the droplet interface could be eliminated by moving the screening platform to a microwell array fabricated in PDMS, silicon, or another material. Hydrogel

emulsions are also gaining popularity as a middle ground between water-in-oil emulsions and rigid microwells.[102,302] Any microarray chosen for library screening will need small reaction volumes to contain the product of slow catalysts and high throughput to screen large libraries for rare catalytic sequences.

6.2.3 Alternative libraries

Once an effective catalyst-screening platform has been established, the composition and design of the oligonucleotide library can be varied. For example, libraries of DNA molecules longer or shorter than 90 nucleotides could be introduced to investigate the effects oligonucleotide size and sequence space on catalyst frequency. Patterned libraries with a bias for certain nucleotides could be compared to fully random libraries, and hybridization arms could be added to flank the random region and improve substrate binding. The abundance of catalysts in DNA libraries could be compared with RNA libraries.

Additionally, it would be valuable to quantify catalyst abundance within synthetic pools of XNAs, which have chemical backbones and bases that do not occur in nature. Although laboratory evolution of XNA catalysts has focused only on modified sugar backbones that are compatible with polymerase enzymes, our single molecule detection platform could study synthetic genetic polymers that have been under-utilized in catalysis. A robust microarray platform could also be used to screen non-nucleic acid libraries like synthetic peptides for catalytic activity.

Single-molecule catalyst detection dramatically increases the viable size and diversity of screening libraries. The droplet microfluidic platform is compatible with

abiotic, fully synthetic oligomer libraries, expanding its impact beyond naturally-occurring systems. Future experiments could therefore address important questions in exobiology and the origins of life: in a non-terrestrial or prebiotic environment, where would we find good catalysts?

6.2.4 Alternative substrates

The substrate and reaction conditions can also be varied. Existing nucleic acid selection techniques use intramolecular reaction designs like hairpin oligonucleotides that contain both the random region and the substrate moiety of interest in a single molecule. Our droplet platform is unique in its intermolecular design, which gives us unprecedented flexibility in the substrates we choose and the reactions we study. Fluorogenic substrates, which are already commercially available for assaying protein enzymes, exist across many classes of biomolecules, including sugars, nucleic acids, peptides, lipids, and small molecules. Custom substrates could also be synthesized for other reactions of interest.

6.2.5 Outlook: Quantification of Catalytic Oligonucleotides

Successful detection of catalytic molecules within large libraries of random oligonucleotide sequences would enable the first-ever quantification of oligonucleotide catalyst abundance, addressing a wide range of fundamental questions: How common are catalytic oligonucleotides? What reactions can they perform? What conditions do they prefer? What is their maximum turnover rate? Without the restrictions imposed by traditional, intramolecular selection reactions, a microfluidic library screening platform can explore novel library and reaction designs.

Overall, these results will help to build a framework for understanding the broader scope of nucleic acid catalysis, the potential role of these catalysts in the origins of life, and the potential applications of new catalytic technology in biosensing and therapeutics. They will contribute concrete, quantitative insights into questions that have historically been unanswerable.

6.3 Future Work: Continuous µFFE Affinity Assay

Chapters 4 and 5 describe progress toward a continuous µFFE affinity assay. First, COC devices were characterized to assess their suitability for time-resolved, continuous protein separations. Then, an aptamer-based µFFE affinity assay was developed for TNFα quantification. Future work will focus on optimizing this assay to improve its reproducibility and sensitivity, which may include changes to the fundamental design of the assay or choice of affinity reagent. The ultimate goal is to integrate the assay with a dynamic biological system for continuous, online measurements of cell secretion. Improvements to the design and fabrication of COC devices may also benefit the final application.

6.3.1 Optimizing the aptamer affinity assay

Initial efforts to improve and optimize the aptamer affinity assay described in Chapter 5 demonstrated the influence of ionic strength and separation buffer on assay performance. Additional optimization of these and other parameters may improve the sensitivity and reproducibility of the assay.

Beyond optimizing the total ionic strength of the aptamer buffer during folding, more nuanced changes to the proportions of sodium and phosphate may improve folding

and bonding while minimizing unwanted salt effects during electrophoretic separation. Apt14 was selected and originally characterized in a buffer similar to PBS because its intended application was *in vivo* inhibition of TNFα.[168] The buffer ingredient expected to be most critical to the aptamer's shape is potassium, which tends to stabilize the G quadruplex structures likely formed by the guanine-rich sequence.[303] Thus, increasing the concentration of potassium in the aptamer folding buffer while decreasing sodium concentration to maintain total ionic strength may benefit the assay.

Other changes to the aptamer folding protocol should also be explored, including non-phosphate buffer systems, varying pH, effects of aptamer concentration during folding, and the times and temperatures used for denaturing and folding. Buffer composition, reagent concentration, time, and temperature should also be optimized during aptamer incubation with TNFα. Other additives to the final sample buffer may reduce surface adsorption before the sample enters the μFFE device.

The choice of fluorophore and its attachment to the aptamer sequence is important to fluorescence intensity during detection. It may also affect binding efficiency (for example, if a bulky fluorophore moiety hinders the binding site) and electrophoretic mobility (for example, if the fluorophore and its linker significantly changes the size and charge of the aptamer). To a limited extent, it may be possible to conjugate multiple fluorophores to a single aptamer molecule to increase fluorescence intensity. There are a variety of fluorophores that have higher quantum yields than the FAM tag used for initial assay development. The length and composition of the linker between the aptamer

sequence and fluorophore could also be further optimized to reduce quenching, maximize binding affinity, and maintain separation resolution.

The composition of the μFFE buffer affects peak shape and resolution. When a salt-containing sample is injected into a separation channel filled with salt-free separation buffer, the aptamer is concentrated into a very sharp peak. As salt is added to the separation buffer, the peak broadens. The ionic strength of the separation buffer should be optimized to maximize resolution between the bound and unbound aptamer peaks while minimizing interference from electrolysis products.

Other mismatches between the sample buffer and separation buffer include pH (7.4 in the sample vs. 7.0 in the separation device) and surfactant (Tween-20 in the sample vs. Triton X-100 in the separation buffer. Optimizing these components may also improve the separation. The separation buffer gradient described in Chapter 5 is an efficient approach to buffer optimization, screening wide ranges of buffer composition in a period of a few minutes.

6.3.2 Alternative μFFE affinity assays

The noncompetitive aptamer assay described in Chapter 5 was chosen for its simplicity and cost effectiveness. Aptamers can be chemically synthesized at relatively low cost. Synthesis incorporates fluorescent labels with high uniformity, and aptamer purification tends to be very effective at removing truncated or unlabeled molecules. Aptamers are also small enough that substrate binding was expected to produce a significant change in electrophoretic mobility. A noncompetitive assay can therefore

quantify target concentration by separating and detecting the bound and unbound aptamer species (Figure 6.1A, top).

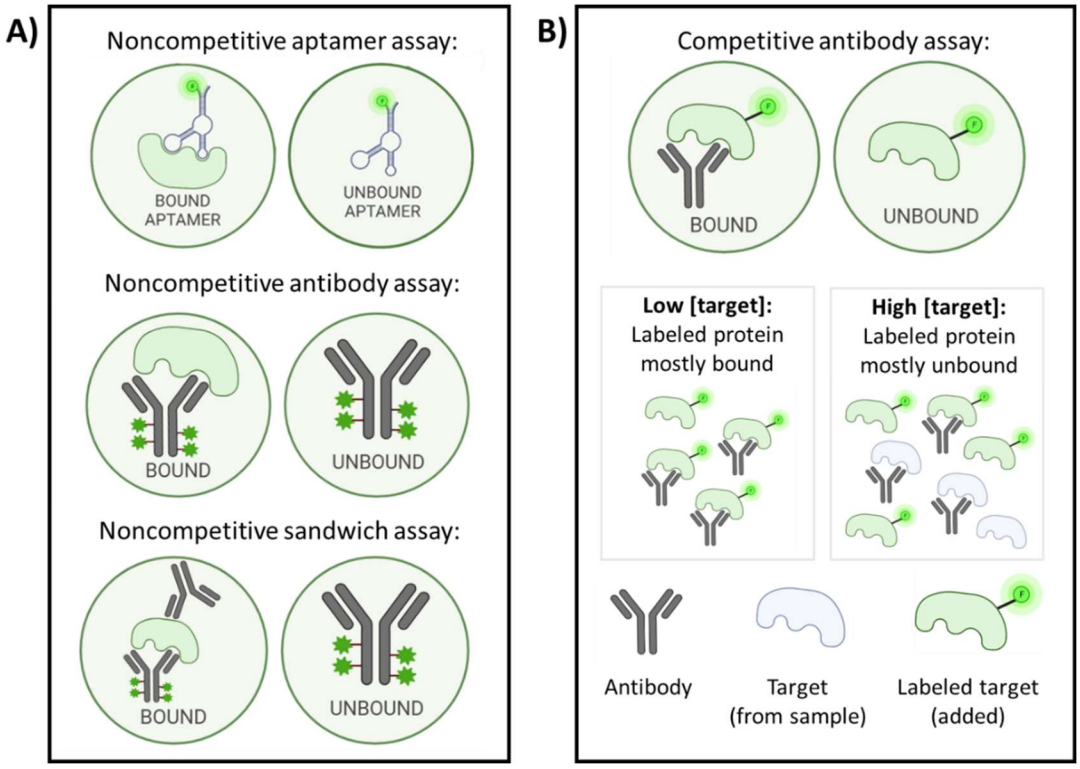

Figure 6.1*: Summary of noncompetitive (A) and competitive (B) affinity assays. Noncompetitive aptamer or antibody assays use a fluorescently-labeled affinity reagent that binds to an unlabeled target in the sample. Noncompetitive sandwich assays add a second, unlabeled affinity reagent that also binds the target and increases electrophoretic mobility shift. Competitive antibodies use an unlabeled affinity reagent and a fluorescently-labeled recombinant protein, which is added to the assay. Increasing target concentrations in the sample compete for binding with the labeled target, increasing the fraction of target that is unbound.*

Alternative assay designs and affinity reagents may be more sensitive and reproducible. Most commercial affinity assays use monoclonal antibodies instead of aptamers. Antibodies bind to antigens with extremely high affinity and selectivity. Unlike aptamers, they do not require folding before use. However, antibodies are much larger than aptamers, and antigen binding is expected to cause only a small change in the electrophoretic mobility of the antibody. A noncompetitive antibody assay (Figure 6.1A,

middle) modeled after the previously described noncompetitive aptamer assay would likely be unsuccessful because it would be difficult to resolve the bound and unbound antibody.

To increase the mobility shift – and therefore improve μFFE resolution – between bound and unbound antibodies, a second, unlabeled antibody could be added to the assay. In this noncompetitive antibody sandwich assay (Figure 6.1A, bottom), the fluorescently-labeled antibody would bind to the target at one site and the secondary antibody would bind at a second site. The antibody-target-antibody complex would be twice as large as the labeled antibody alone, ideally producing a significant change in electrophoretic mobility.

In addition to improving reproducibility by eliminating the aptamer folding step, this antibody sandwich assay may be able to dramatically improve sensitivity by increasing the number of fluorescent moieties on the affinity agent. The aptamer assay uses a short DNA oligonucleotide with a single FAM or ATTO 488 fluorophore moiety. Addition of multiple labels or a high-fluorescence tag like a bead or nanoparticle to the aptamer would increase signal but also decrease the mobility shift between the bound and unbound species. A sandwich assay may be able to overcome this limitation and incorporate bigger, brighter labels.

An alternative affinity assay approach would move the fluorophore to the target and perform a competitive assay (Figure 6.1B). In this design, a fluorescently-labeled, laboratory-derived target like a recombinant protein would be added to an assay with an unlabeled aptamer or antibody. The labeled target would compete with unlabeled target in the sample for binding sites on the antibody. As the concentration of target molecules in the sample increases, a smaller fraction of the labeled target will be bound to the antibody,

and a larger fraction will be unbound. If the target is significantly smaller than the antibody, there will be a larger mobility shift between the bound and unbound species, so the complex can be separated and detected using μFFE.

6.3.3 Continuous and biological measurements

The ultimate goal of the μFFE aptamer assay is to integrate the device with a biological specimen and continuously monitor the concentration of TNFα present as the specimen responds to stimuli. Figure 6.2 shows an example of an online detection setup using a μFFE aptamer assay and cells in a perfusion chamber. As perfusate leaves the chamber, it will be mixed with the fluorescently labeled aptamer. The mixture will equilibrate in a long reaction capillary, where the aptamer will bind to target molecules in the perfusate. Then the bound and unbound species will be separated and detected on a μFFE device. Changes in the levels of target secreted by the cells after stimulation will be quantified based on the changing fluorescence intensities of the bound and unbound aptamer peaks.

Before performing a fully integrated online affinity assay, a series of simplified experiments could be used to assess the compatibility of the platform and assay with dynamic, continuous samples and biological samples. Chapter 5 describes the injection of TNFα boluses into a flowing stream of aptamer, an approach intended to measure temporal response times to changes in TNFα concentration. Although the TNFα-bound aptamer peak was not clearly visible in initial attempts, additional optimization of the assay and fluidic setup is expected to improve the temporal response of the assay. This experiment would

determine the rise and fall time of the bound complex and could be used to optimize the length of the reaction capillary, which determines incubation time.

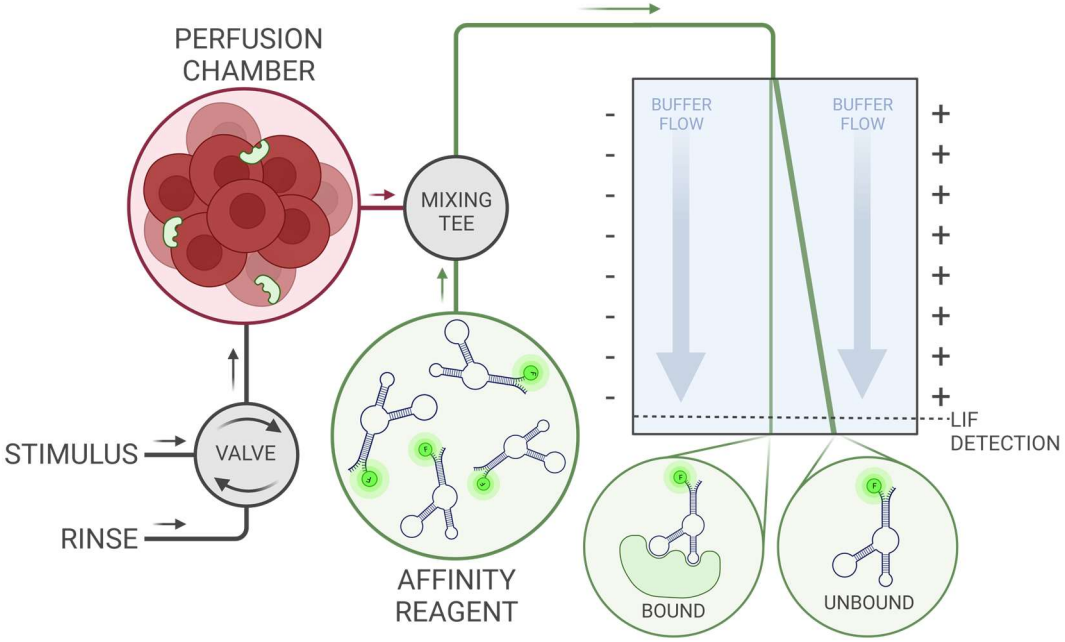

***Figure 6.2**: Online, continuous monitoring of cells in a perfusion chamber using a µFFE aptamer assay. Created with Biorender.com.*

To demonstrate the sensitivity of the assay to biological levels of TNFα, macrophages could be grown and stimulated offline. Media samples could be mixed with aptamer, and the static sample could be separated and detected using µFFE. This experiment would determine appropriate cell culture and stimulation parameters before the incorporation of more complex fluidic components. It would also assess the sensitivity and selectivity of the aptamer assay with a biological sample and its matrix.

6.3.4 µFFE device and fabrication improvements

Several opportunities exist to update the design and fabrication methods for COC devices. Of these, the most important goal is to improve the interface between the sample capillary and the µFFE device. In the current design, the capillary enters the device

perpendicular to the separation channel, through a hole drilled through the face of the device (Figure 6.3A). If the sample capillary is not inserted completely into the though-hole so that its end is flush with the separation channel, sample fills the dead volume before entering the separation channel, causing both spatial and temporal broadening (Figure 6.3B).

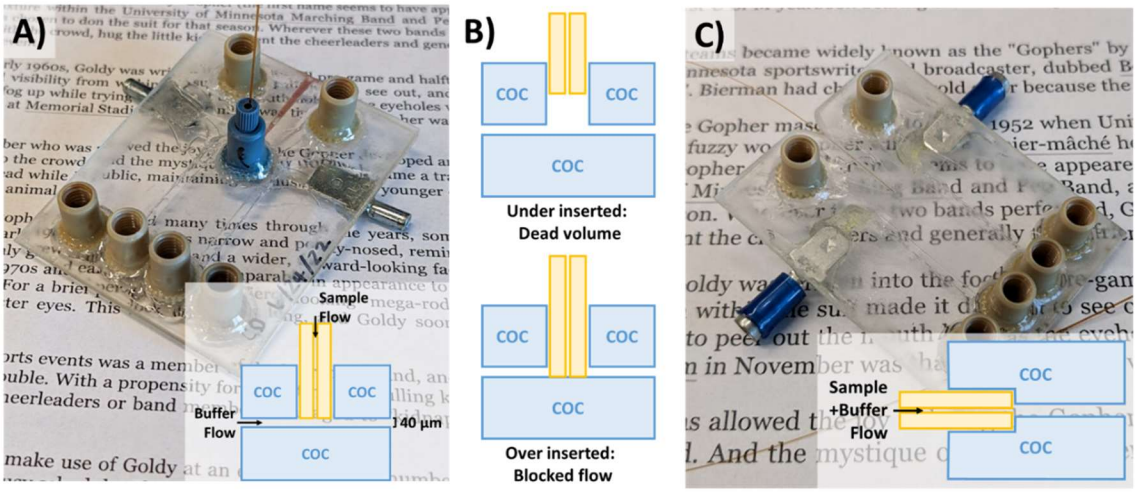

***Figure 6.3**: A) COC device with a 90° sample inlet. The sample capillary enters through a hole in the face of the COC imprint. B) Examples of under- and over-insertion of the sample capillary (yellow) into COC (blue) devices. C) COC device with a co-linear sample inlet. The sample capillary enters through an imprinted channel that exits the edge of the device.*

Previous µFFE device designs in both glass[219] and ABS[231] have used a co-linear sample inlet that reduces dead volume by introducing the sample capillary through the edge of the device, in the same plane and direction as fluid flow through the separation channel. Figure 6.3C shows an example of co-linear sample inlet in a COC device. This design is expected to improve spatial and temporal resolution in COC devices, but it also poses fabrication challenges. Both halves of the COC device need to be imprinted with a capillary channel, and bonding will require precise channel alignment.

Beyond the sample interface, other fabrication-related efforts could investigate the geometry of the separation channel and improve device design and fabrication to ensure uniform buffer velocity in the separation channel. Two-dimensional nLC × μFFE separations have revealed that the buffer velocity in the separation channel increases with increasing distance from the sample inlet. Dye separations also demonstrated a pattern of hydrodynamic focusing as samples approach the outlet of the separation channel (Figure 6.4). Both of these observations point to non-uniform buffer flow across the width and length of the separation channel.

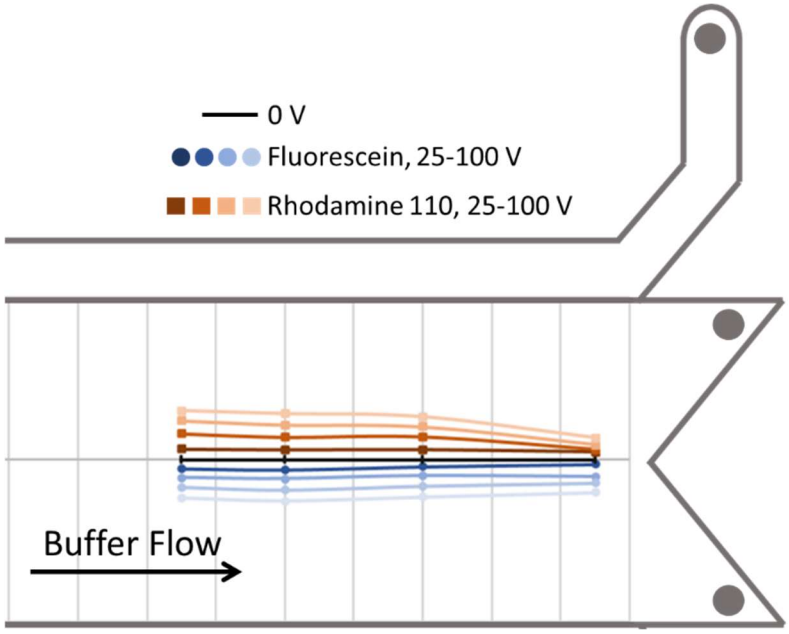

Figure 6.4*: Normalized position of fluorescein (blue circle) and rhodamine 110 (orange square) peaks detected at 7, 10, 14, and 19 mm from the sample inlet with an applied potential of 25-100 V. Grey lines indicate the boundaries of the separation channel and one electrode channel. Grey circles indicate outlets. Buffer flows from left to right through the separation channel. Peak positions demonstrate a focusing pattern as the sample approaches the outlet of the separation channel.*

Fluid modeling could identify fundamental issues in the device geometry that contribute to non-uniform buffer velocity, and surface profiling could isolate specific

fabrication steps that contribute to non-uniform separation channel depth. More uniform buffer flow would improve the stability and reproducibility of all separations on COC devices.

Finally, streamlining the fabrication process could decrease the total time required to produce usable devices and also reduce device-to-device variability. In particular, there is room to optimize the vapor exposure, temperature, and pressure used during bonding. More significant changes to the bonding protocol, including metal bonding rigs that allow higher bonding temperatures, exclusive (non-thermal) vapor bonding, or plasma bonding may prove more effective than current methods. Vapor-free thermal bonding of COC has also been reported by pressing a feature-free cover plate made of low T_g Topas 5013 into an imprinted COC substrate made of high T_g Topas 6015.[263]

6.3.5 Outlook: Continuous µFFE Affinity Assay

The µFFE affinity assay developed here offers broad flexibility in design, which can be leveraged to study a wider range of biological processes. Aptamers and antibodies can bind to targets with different sizes, charges, and structural features. Most importantly, µFFE affinity assays could be used to monitor biological responses on many timescales. Discrete assays like ELISAs use a separate sample and reaction for each timepoint studied. A ten-point time course would require ten discrete samples assayed in ten separate wells. Meanwhile, µFFE continuously separates and detects sample components. Sampling rates are limited only by the acquisition of the camera, and temporal resolution is limited by physical parameters like mixing, diffusion, and adsorption. µFFE is equally well suited for monitoring fast processes (e.g., several samples per second over a time course of minutes)

and slower processes (e.g., one sample per minute over a time course of hours). It can collect hundreds of thousands of temporal data points, creating a complete and continuous profile of the sample over time. Once optimized, μFFE affinity assays would offer an entirely new approach to biomolecule detection, sensitively and selectively monitoring dynamic systems that are otherwise only studied in discrete snapshots.

6.4 Impact

Altogether, this thesis describes advancements at the intersection of microfluidics and oligonucleotide technology. From screening billions of DNA sequences in a single second to continuously detecting the bound fraction of an aptamer, these microfluidic assays aim to address biologically relevant questions on remarkable scales. They underscore the value of microfluidics for investigating the dynamic and complex systems of the natural world.

References

(1) Hollenstein, M. DNA Catalysis: The Chemical Repertoire of DNAzymes. *Molecules* **2015**, *20* (11), 20777–20804.

(2) Silverman, S. K. Catalytic DNA: Scope, Applications, and Biochemistry of Deoxyribozymes. *Trends Biochem. Sci.* **2016**, *41* (7), 595–609.

(3) Morrison, D.; Rothenbroker, M.; Li, Y. DNAzymes: Selected for Applications. *Small Methods* **2018**, *2* (3), 1700319.

(4) Khachigian, L. M. Deoxyribozymes as Catalytic Nanotherapeutic Agents. *Cancer Res.* **2019**, *79* (5), 879–888.

(5) Gilbert, W. Origin of Life: The RNA World. *Nature* **1986**, *319* (6055), 618–618.

(6) Kruger, K.; Grabowski, P. J.; Zaug, A. J.; Sands, J.; Gottschling, D. E.; Cech, T. R. Self-Splicing RNA: Autoexcision and Autocyclization of the Ribosomal RNA Intervening Sequence of Tetrahymena. *Cell* **1982**, *31* (1), 147–157.

(7) Reed, R. E.; Baer, M. F.; Guerrier-Takada, C.; Donis-Keller, H.; Altman, S. Nucleotide Sequence of the Gene Encoding the RNA Subunit (M1 RNA) of Ribonuclease P from Escherichia Coli. *Cell* **1982**, *30* (2), 627–636.

(8) Cech, T. R.; Herschlag, D. Group I Ribozymes: Substrate Recognition, Catalytic Strategies, and Comparative Mechanistic Analysis. In *Nucleic Acids and Molecular Biology*; Eckstein, F., Lilley, D. M. J., Eds.; Springer, Berlin, Heidelberg, 1996; pp 1–17.

(9) Stark, B. C.; Kole, R.; Bowman, E. J.; Altman, S. Ribonuclease P: An Enzyme with an Essential RNA Component. *Proc. Natl. Acad. Sci. U. S. A.* **1978**, *75* (8), 3717–3721.

(10) Gardiner, K.; Pace, N. R. RNase P of Bacillus Subtilis Has a RNA Component. *J. Biol. Chem.* **1980**, *255* (16), 7507–7509.

(11) Guerrier-Takada, C.; Gardiner, K.; Marsh, T.; Pace, N.; Altman, S. The RNA Moiety of Ribonuclease P Is the Catalytic Subunit of the Enzyme. *Cell* **1983**, *35* (3), 849–857.

(12) Canny, M. D.; Jucker, F. M.; Kellogg, E.; Khvorova, A.; Jayasena, S. D.; Pardi, A. Fast Cleavage Kinetics of a Natural Hammerhead Ribozyme. *J. Am. Chem. Soc.* **2004**, *126* (24), 10848–10849.

(13) Buzayan, J. M.; Gerlach, W. L.; Bruening, G. Non-Enzymatic Cleavage and Ligation of RNAs Complementary to a Plant Virus Satellite RNA. *Nature* **1986**, *323* (6086), 349–353.

(14) Wu, H. N.; Lin, Y. J.; Lin, F. P.; Makino, S.; Chang, M. F.; Lai, M. M. Human Hepatitis Delta Virus RNA Subfragments Contain an Autocleavage Activity. *Proc. Natl. Acad. Sci. U. S. A.* **1989**, *86* (6), 1831–1835.

(15) Kennell, J. C.; Saville, B. J.; Mohr, S.; Kuiper, M. T.; Sabourin, J. R.; Collins, R. A.; Lambowitz, A. M. The VS Catalytic RNA Replicates by Reverse Transcription as a Satellite of a Retroplasmid. *Genes & Development* **1995**, *9* (3), 294–303.

(16) Roth, A.; Weinberg, Z.; Chen, A. G. Y.; Kim, P. B.; Ames, T. D.; Breaker, R. R. A Widespread Self-Cleaving Ribozyme Class Is Revealed by Bioinformatics. *Nat. Chem. Biol.* **2014**, *10* (1), 56–60.
(17) Doudna, J. A.; Cech, T. R. The Chemical Repertoire of Natural Ribozymes. *Nature* **2002**, *418* (6894), 222–228.
(18) Joyce, G. F. The Antiquity of RNA-Based Evolution. *Nature* **2002**, *418* (6894), 214–221.
(19) Saad, N. Y. A Ribonucleopeptide World at the Origin of Life. *Journal of Systematics and Evolution* **2018**, *56* (1), 1–13.
(20) Johnston, W. K.; Unrau, P. J.; Lawrence, M. S.; Glasner, M. E.; Bartel, D. P. RNA-Catalyzed RNA Polymerization: Accurate and General RNA-Templated Primer Extension. *Science* **2001**, *292*, 1319–1325.
(21) Sczepanski, J. T.; Joyce, G. F. A Cross-Chiral RNA Polymerase Ribozyme. *Nature* **2014**, *515* (7527), 440–442.
(22) Bartel, D. P.; Szostak, J. W. Isolation of New Ribozymes from a Large Pool of Random Sequences. *Science* **1993**, *261* (5127), 1411–1418.
(23) Voytek, S. B.; Joyce, G. F. Emergence of a Fast-Reacting Ribozyme That Is Capable of Undergoing Continuous Evolution. *Proc. Natl. Acad. Sci. U. S. A.* **2007**, *104* (39), 15288–15293.
(24) Lorsch, J. R.; Szostak, J. W. In Vitro Evolution of New Ribozymes with Polynucleotide Kinase Activity. *Nature* **1994**, *371* (6492), 31–36.
(25) Jenne, A.; Famulok, M. A Novel Ribozyme with Ester Transferase Activity. *Chem. Biol.* **1998**, *5* (1), 23–34.
(26) Fusz, S.; Eisenführ, A.; Srivatsan, S. G.; Heckel, A.; Famulok, M. A Ribozyme for the Aldol Reaction. *Chem. Biol.* **2005**, *12* (8), 941–950.
(27) Sengle, G.; Eisenführ, A.; Arora, P. S.; Nowick, J. S.; Famulok, M. Novel RNA Catalysts for the Michael Reaction. *Chem. Biol.* **2001**, *8* (5), 459–473.
(28) Bernhardt, H. S. The RNA World Hypothesis: The Worst Theory of the Early Evolution of Life (except for All the Others). *Biol. Direct* **2012**, *7* (1), 23.
(29) Francis, B. R. An Alternative to the RNA World Hypothesis. *Trends Evol. Biol.* **2011**, *3* (2), 2–11.
(30) Caetano-Anollés, G.; Kim, K. M.; Caetano-Anollés, D. The Phylogenomic Roots of Modern Biochemistry: Origins of Proteins, Cofactors and Protein Biosynthesis. *J. Mol. Evol.* **2012**, *74* (1–2), 1–34.
(31) Patel, D. Structural Analysis of Nucleic Acid Aptamers. *Curr. Opin. Chem. Biol.* **1997**, *1* (1), 32–46.
(32) Breaker, R. R.; Joyce, G. F. A DNA Enzyme That Cleaves RNA. *Chem. Biol.* **1994**, *1* (4), 223–229.
(33) Breaker, R. R.; Joyce, G. F. A DNA Enzyme with Mg(2+)-Dependent RNA Phosphoesterase Activity. *Chem. Biol.* **1995**, *2* (10), 655–660.
(34) Santoro, S. W.; Joyce, G. F. A General Purpose RNA-Cleaving DNA Enzyme. *Proc. Natl. Acad. Sci. U. S. A.* **1997**, *94* (9), 4262–4266.
(35) Carmi, N.; Shultz, L. A.; Breaker, R. R. In Vitro Selection of Self-Cleaving DNAs. *Chem. Biol.* **1996**, *3* (12), 1039–1046.

(36) Carmi, N.; Balkhi, S. R.; Breaker, R. R. Cleaving DNA with DNA. *Proc. Natl. Acad. Sci. U. S. A.* **1998**, *95* (5), 2233–2237.
(37) Carmi, N.; Breaker, R. R. Characterization of a DNA-Cleaving Deoxyribozyme. *Bioorg. Med. Chem.* **2001**, *9* (10), 2589–2600.
(38) Chandra, M.; Sachdeva, A.; Silverman, S. K. DNA-Catalyzed Sequence-Specific Hydrolysis of DNA. *Nat. Chem. Biol.* **2009**, *5* (10), 718–720.
(39) Brandsen, B. M.; Hesser, A. R.; Castner, M. A.; Chandra, M.; Silverman, S. K. DNA-Catalyzed Hydrolysis of Esters and Aromatic Amides. *J. Am. Chem. Soc.* **2013**, *135* (43), 16014–16017.
(40) Zhou, C.; Avins, J. L.; Klauser, P. C.; Brandsen, B. M.; Lee, Y.; Silverman, S. K. DNA-Catalyzed Amide Hydrolysis. *J. Am. Chem. Soc.* **2016**, *138* (7), 2106–2109.
(41) Chandrasekar, J.; Silverman, S. K. Catalytic DNA with Phosphatase Activity. *Proc. Natl. Acad. Sci. U. S. A.* **2013**, *110* (14), 5315–5320.
(42) Chandrasekar, J.; Wylder, A. C.; Silverman, S. K. Phosphoserine Lyase Deoxyribozymes: DNA-Catalyzed Formation of Dehydroalanine Residues in Peptides. *J. Am. Chem. Soc.* **2015**, *137* (30), 9575–9578.
(43) Cuenoud, B.; Szostak, J. W. A DNA Metalloenzyme with DNA Ligase Activity. *Nature* **1995**, *375* (6532), 611–614.
(44) Sreedhara, A.; Li, Y.; Breaker, R. R. Ligating DNA with DNA. *J. Am. Chem. Soc.* **2004**, *126* (11), 3454–3460.
(45) Purtha, W. E.; Coppins, R. L.; Smalley, M. K.; Silverman, S. K. General Deoxyribozyme-Catalyzed Synthesis of Native 3'−5' RNA Linkages. *J. Am. Chem. Soc.* **2005**, *127* (38), 13124–13125.
(46) Flynn-Charlebois, A.; Wang, Y.; Prior, T. K.; Rashid, I.; Hoadley, K. A.; Coppins, R. L.; Wolf, A. C.; Silverman, S. K. Deoxyribozymes with 2'−5' RNA Ligase Activity. *J. Am. Chem. Soc.* **2003**, *125* (9), 2444–2454.
(47) Pradeepkumar, P. I.; Höbartner, C.; Baum, D. A.; Silverman, S. K. DNA-Catalyzed Formation of Nucleopeptide Linkages. *Angew. Chem., Int. Ed.* **2008**, *47* (9), 1753–1757.
(48) Chu, C.-C.; Wong, O. Y.; Silverman, S. K. A Generalizable DNA-Catalyzed Approach to Peptide-Nucleic Acid Conjugation. *ChemBioChem* **2014**, *15* (13), 1905–1910.
(49) Sachdeva, A.; Silverman, S. K. DNA-Catalyzed Serine Side Chain Reactivity and Selectivity. *Chem. Commun.* **2010**, *46* (13), 2215.
(50) Walsh, S. M.; Sachdeva, A.; Silverman, S. K. DNA Catalysts with Tyrosine Kinase Activity. *J. Am. Chem. Soc.* **2013**, *135* (40), 14928–14931.
(51) Wang, P.; Silverman, S. K. DNA-Catalyzed Introduction of Azide at Tyrosine for Peptide Modification. *Angew. Chem., Int. Ed.* **2016**, *55* (34), 10052–10056.
(52) Brandsen, B. M.; Velez, T. E.; Sachdeva, A.; Ibrahim, N. A.; Silverman, S. K. DNA-Catalyzed Lysine Side Chain Modification. *Angew. Chem., Int. Ed.* **2014**, *53* (34), 9045–9050.
(53) Breaker, R. R.; Emilsson, G. M.; Lazarev, D.; Nakamura, S.; Puskarz, I. J.; Roth, A.; Sudarsan, N. A Common Speed Limit for RNA-Cleaving Ribozymes and Deoxyribozymes. *RNA* **2003**, *9* (8), 949–957.

(54) Yu, H.; Zhang, S.; Chaput, J. C. Darwinian Evolution of an Alternative Genetic System Provides Support for TNA as an RNA Progenitor. *Nat. Chem.* **2012**, *4* (3), 183–187.
(55) Taylor, A. I.; Pinheiro, V. B.; Smola, M. J.; Morgunov, A. S.; Peak-Chew, S.; Cozens, C.; Weeks, K. M.; Herdewijn, P.; Holliger, P. Catalysts from Synthetic Genetic Polymers. *Nature* **2015**, *518* (7539), 427–430.
(56) Wang, Y.; Ngor, A. K.; Nikoomanzar, A.; Chaput, J. C. Evolution of a General RNA-Cleaving FANA Enzyme. *Nat. Commun.* **2018**, *9* (1), 5067.
(57) Taylor, A. I.; Wan, C. J. K.; Donde, M. J.; Peak-Chew, S.-Y.; Holliger, P. A Modular XNAzyme Cleaves Long, Structured RNAs under Physiological Conditions and Enables Allele-Specific Gene Silencing. *Nat. Chem.* **2022**, *14* (11), 1295–1305.
(58) Wang, Y.; Wang, Y.; Song, D.; Sun, X.; Zhang, Z.; Li, X.; Li, Z.; Yu, H. A Threose Nucleic Acid Enzyme with RNA Ligase Activity. *J. Am. Chem. Soc.* **2021**, *143* (21), 8154–8163.
(59) Wang, Y.; Vorperian, A.; Shehabat, M.; Chaput, J. C. Evaluating the Catalytic Potential of a General RNA-Cleaving FANA Enzyme. *ChemBioChem* **2020**, *21* (7), 1001–1006.
(60) Malik, T. N.; Chaput, J. C. XNA Enzymes by Evolution and Design. *Curr. Res. Chem. Biol.* **2021**, *1*, 100012.
(61) Santiago, F. S.; Lowe, H. C.; Kavurma, M. M.; Chesterman, C. N.; Baker, A.; Atkins, D. G.; Khachigian, L. M. New DNA Enzyme Targeting Egr-1 mRNA Inhibits Vascular Smooth Muscle Proliferation and Regrowth after Injury. *Nat. Med.* **1999**, *5* (11), 1264–1269.
(62) Liu, G.-N.; Teng, Y.-X.; Yan, W. Transfected Synthetic DNA Enzyme Gene Specifically Inhibits Egr-1 Gene Expression and Reduces Neointimal Hyperplasia Following Balloon Injury in Rats. *Int. J. Cardiol.* **2008**, *129* (1), 118–124.
(63) Zhang, G.; Dass, C. R.; Sumithran, E.; Di Girolamo, N.; Sun, L.-Q.; Khachigian, L. M. Effect of Deoxyribozymes Targeting C-Jun on Solid Tumor Growth and Angiogenesis in Rodents. *JNCI, J. Natl. Cancer Inst.* **2004**, *96* (9), 683–696.
(64) Grassi, G.; Grassi, M. First-in-Human Trial of Dz13 for Nodular Basal-Cell Carcinoma. *Lancet* **2013**, *381* (9880), 1797–1798.
(65) Krug, N.; Hohlfeld, J. M.; Kirsten, A.-M.; Kornmann, O.; Beeh, K. M.; Kappeler, D.; Korn, S.; Ignatenko, S.; Timmer, W.; Rogon, C.; Zeitvogel, J.; Zhang, N.; Bille, J.; Homburg, U.; Turowska, A.; Bachert, C.; Werfel, T.; Buhl, R.; Renz, J.; Garn, H.; Renz, H. Allergen-Induced Asthmatic Responses Modified by a GATA3-Specific DNAzyme. *N. Engl. J. Med.* **2015**, *372* (21), 1987–1995.
(66) Zhou, J.; Yang, X. Q.; Xie, Y. Y.; Zhao, X. D.; Jiang, L. P.; Wang, L. J.; Cui, Y. X. Inhibition of Respiratory Syncytial Virus of Subgroups A and B Using Deoxyribozyme DZ1133 in Mice. *Virus Res.* **2007**, *130* (1–2), 241–248.
(67) Unwalla, H.; Chakraborti, S.; Sood, V.; Gupta, N.; Banerjea, A. C. Potent Inhibition of HIV-1 Gene Expression and TAT-Mediated Apoptosis in Human T Cells by Novel Mono- and Multitarget Anti-TAT/Rev/Env Ribozymes and a

General Purpose RNA-Cleaving DNA-Enzyme. *Antiviral Res.* **2006**, *72* (2), 134–144.
(68) Hou, Z.; Meng, J.; Zhao, J.; Hu, B.; Liu, J.; Yan, X.; Jia, M.; Luo, X. Inhibition of β-Lactamase-Mediated Oxacillin Resistance in Staphylococcus Aureus by a Deoxyribozyme. *Acta Pharmacol. Sin.* **2007**, *28* (11), 1775–1782.
(69) Huang, P. J. J.; Liu, J. Sensing Parts-per-Trillion Cd 2+ , Hg 2+ , and Pb 2+ Collectively and Individually Using Phosphorothioate DNAzymes. *Anal. Chem.* **2014**, *86* (12), 5999–6005.
(70) Liu, J.; Brown, A. K.; Meng, X.; Cropek, D. M.; Istok, J. D.; Watson, D. B.; Lu, Y. A Catalytic Beacon Sensor for Uranium with Parts-per-Trillion Sensitivity and Millionfold Selectivity. *Proc. Natl. Acad. Sci. U. S. A.* **2007**, *104* (7), 2056–2061.
(71) Liu, J.; Lu, Y. Improving Fluorescent DNAzyme Biosensors by Combining Inter- and Intramolecular Quenchers. *Anal. Chem.* **2003**, *75* (23), 6666–6672.
(72) Liu, J.; Lu, Y. Rational Design of "Turn-On" Allosteric DNAzyme Catalytic Beacons for Aqueous Mercury Ions with Ultrahigh Sensitivity and Selectivity. *Angew. Chem., Int. Ed.* **2007**, *46* (40), 7587–7590.
(73) Ali, M. M.; Aguirre, S. D.; Lazim, H.; Li, Y. Fluorogenic DNAzyme Probes as Bacterial Indicators. *Angew. Chem., Int. Ed.* **2011**, *50* (16), 3751–3754.
(74) Shen, Z.; Wu, Z.; Chang, D.; Zhang, W.; Tram, K.; Lee, C.; Kim, P.; Salena, B. J.; Li, Y. A Catalytic DNA Activated by a Specific Strain of Bacterial Pathogen. *Angew. Chem., Int. Ed.* **2016**, *55* (7), 2431–2434.
(75) Chandra, M.; Silverman, S. K. DNA and RNA Can Be Equally Efficient Catalysts for Carbon - Carbon Bond Formation. *J. Am. Chem. Soc.* **2008**, *130* (10), 2936–2937.
(76) Mohan, U.; Burai, R.; McNaughton, B. R. In Vitro Evolution of a Friedel-Crafts Deoxyribozyme. *Org. Biomol. Chem.* **2013**, *11* (14), 2241–2244.
(77) Bar-Even, A.; Noor, E.; Savir, Y.; Liebermeister, W.; Davidi, D.; Tawfik, D. S.; Milo, R. The Moderately Efficient Enzyme: Evolutionary and Physicochemical Trends Shaping Enzyme Parameters. *Biochemistry* **2011**, *50* (21), 4402–4410.
(78) Bonaccio, M.; Credali, A.; Peracchi, A. Kinetic and Thermodynamic Characterization of the RNA-Cleaving 8-17 Deoxyribozyme. *Nucleic Acids Res.* **2004**, *32* (3), 916–925.
(79) Li, Y.; Breaker, R. R. Kinetics of RNA Degradation by Specific Base Catalysis of Transesterification Involving the 2'-Hydroxyl Group. *J. Am. Chem. Soc.* **1999**, *121* (23), 5364–5372.
(80) Soukup, G. A.; Breaker, R. R. Relationship between Internucleotide Linkage Geometry and the Stability of RNA. *RNA* **1999**, *5* (10), 1308–1325.
(81) Emilsson, G. M.; Nakamura, S.; Roth, A.; Breaker, R. R. Ribozyme Speed Limits. *RNA* **2003**, *9* (8), 907–918.
(82) Theberge, A. B.; Courtois, F.; Schaerli, Y.; Fischlechner, M.; Abell, C.; Hollfelder, F.; Huck, W. T. S. Microdroplets in Microfluidics: An Evolving Platform for Discoveries in Chemistry and Biology. *Angew. Chem., Int. Ed.* **2010**, *49* (34), 5846–5868.

(83) Basova, E. Y.; Foret, F. Droplet Microfluidics in (Bio)Chemical Analysis. *Analyst* **2015**, *140* (1), 22–38.
(84) Lederberg, J. A Simple Method for Isolating Individual Microbes. *J. Bacteriol.* **1954**, *68* (2), 258–259.
(85) Nossal, G. J. V. Antibody Production by Single Cells. *Br. J. Exp. Pathol.* **1958**, *39* (5), 544–551.
(86) Rotman, B. Measurement of Activity of Single Molecules of Beta-D-Galactosidase. *Proc. Natl. Acad. Sci. U. S. A.* **1961**, *47* (12), 1981–1991.
(87) Song, H.; Ismagilov, R. F. Millisecond Kinetics on a Microfluidic Chip Using Nanoliters of Reagents. *J. Am. Chem. Soc.* **2003**, *125* (47), 14613–14619.
(88) Song, H.; Tice, J. D.; Ismagilov, R. F. A Microfluidic System for Controlling Reaction Networks in Time. *Angew. Chem., Int. Ed.* **2003**, *42* (7), 768–772.
(89) Tice, J. D.; Song, H.; Lyon, A. D.; Ismagilov, R. F. Formation of Droplets and Mixing in Multiphase Microfluidics at Low Values of the Reynolds and the Capillary Numbers. *Langmuir* **2003**, *19* (22), 9127–9133.
(90) Stanley, C. E.; Wootton, R. C. R.; DeMello, A. J. Continuous and Segmented Flow Microfluidics: Applications in Highthroughput Chemistry and Biology. *Chimia* **2012**, *66* (3), 88–98.
(91) Thorsen, T.; Roberts, R. W.; Arnold, F. H.; Quake, S. R. Dynamic Pattern Formation in a Vesicle-Generating Microfluidic Device. *Phys. Rev. Lett.* **2001**, *86* (18), 4163–4166.
(92) Anna, S. L.; Bontoux, N.; Stone, H. A. Formation of Dispersions Using "Flow Focusing" in Microchannels. *Appl. Phys. Lett.* **2003**, *82* (3), 364–366.
(93) Cramer, C.; Fischer, P.; Windhab, E. J. Drop Formation in a Co-Flowing Ambient Fluid. *Chem. Eng. Sci.* **2004**, *59* (15), 3045–3058.
(94) Collins, D. J.; Neild, A.; deMello, A.; Liu, A. Q.; Ai, Y. The Poisson Distribution and beyond: Methods for Microfluidic Droplet Production and Single Cell Encapsulation. *Lab Chip* **2015**, *15* (17), 3439–3459.
(95) Gruner, P.; Riechers, B.; Chacon Orellana, L. A.; Brosseau, Q.; Maes, F.; Beneyton, T.; Pekin, D.; Baret, J.-C. Stabilisers for Water-in-Fluorinated-Oil Dispersions: Key Properties for Microfluidic Applications. *Curr. Opin. Colloid Interface Sci.* **2015**, *20* (3), 183–191.
(96) Bai, Y.; He, X.; Liu, D.; Patil, S. N.; Bratton, D.; Huebner, A.; Hollfelder, F.; Abell, C.; Huck, W. T. S. A Double Droplet Trap System for Studying Mass Transport across a Droplet-Droplet Interface. *Lab Chip* **2010**, *10* (10), 1281.
(97) Holt, D. J.; Payne, R. J.; Chow, W. Y.; Abell, C. Fluorosurfactants for Microdroplets: Interfacial Tension Analysis. *J. Colloid Interface Sci.* **2010**, *350* (1), 205–211.
(98) Chowdhury, M. S.; Zheng, W.; Kumari, S.; Heyman, J.; Zhang, X.; Dey, P.; Weitz, D. A.; Haag, R. Dendronized Fluorosurfactant for Highly Stable Water-in-Fluorinated Oil Emulsions with Minimal Inter-Droplet Transfer of Small Molecules. *Nat. Commun.* **2019**, *10* (1), 4546.
(99) Pan, M.; Rosenfeld, L.; Kim, M.; Xu, M.; Lin, E.; Derda, R.; Tang, S. K. Y. Fluorinated Pickering Emulsions Impede Interfacial Transport and Form Rigid

Interface for the Growth of Anchorage-Dependent Cells. *ACS Appl. Mater. Interfaces* **2014**, *6* (23), 21446–21453.
(100) Hindson, B. J.; Ness, K. D.; Masquelier, D. A.; Belgrader, P.; Heredia, N. J.; Makarewicz, A. J.; Bright, I. J.; Lucero, M. Y.; Hiddessen, A. L.; Legler, T. C.; Kitano, T. K.; Hodel, M. R.; Petersen, J. F.; Wyatt, P. W.; Steenblock, E. R.; Shah, P. H.; Bousse, L. J.; Troup, C. B.; Mellen, C.; Wittmann, D. K.; Erndt, N. G.; Cauley, T. H.; Koehler, R. T.; So, A. P.; Dube, S.; Rose, K. A.; Montesclaros, L.; Wang, S.; Stumbo, D. P.; Hodges, S. P.; Romine, S.; Milanovich, F. P.; White, H. E.; Regan, J. F.; Karlin-neumann, G. A.; Hindson, C. M.; Saxonov, S.; Colston, B. W. High-Throughput Droplet Digital PCR System for Absolute Quantitation of DNA Copy Number. *Anal. Chem.* **2011**, *83* (8), 8604–8610.
(101) Huang, C.; Jiang, Y.; Li, Y.; Zhang, H. Droplet Detection and Sorting System in Microfluidics: A Review. *Micromachines* **2022**, *14* (1), 103.
(102) Shang, L.; Cheng, Y.; Zhao, Y. Emerging Droplet Microfluidics. *Chem. Rev.* **2017**, *117* (12), 7964–8040.
(103) Murray, B. E.; Penabad, L. I.; Kennedy, R. T. Advances in Coupling Droplet Microfluidics to Mass Spectrometry. *Curr. Opin. Biotechnol.* **2023**, *82*, 102962.
(104) Baret, J.-C.; Miller, O. J.; Taly, V.; Ryckelynck, M.; El-Harrak, A.; Frenz, L.; Rick, C.; Samuels, M. L.; Hutchison, J. B.; Agresti, J. J.; Link, D. R.; Weitz, D. A.; Griffiths, A. D. Fluorescence-Activated Droplet Sorting (FADS): Efficient Microfluidic Cell Sorting Based on Enzymatic Activity. *Lab Chip* **2009**, *9* (13), 1850.
(105) Obexer, R.; Pott, M.; Zeymer, C.; Griffiths, A. D.; Hilvert, D. Efficient Laboratory Evolution of Computationally Designed Enzymes with Low Starting Activities Using Fluorescence-Activated Droplet Sorting. *Protein Engineering, Design & Selection* **2016**, *29* (9), 355–366.
(106) Vallejo, D.; Nikoomanzar, A.; Paegel, B. M.; Chaput, J. C. Fluorescence-Activated Droplet Sorting for Single-Cell Directed Evolution. *ACS Synth. Biol.* **2019**, *8* (6), 1430–1440.
(107) Best, R. J.; Lyczakowski, J. J.; Abalde-Cela, S.; Yu, Z.; Abell, C.; Smith, A. G. Label-Free Analysis and Sorting of Microalgae and Cyanobacteria in Microdroplets by Intrinsic Chlorophyll Fluorescence for the Identification of Fast Growing Strains. *Anal. Chem.* **2016**, *88* (21), 10445–10451.
(108) Wu, L.; Chen, P.; Dong, Y.; Feng, X.; Liu, B.-F. Encapsulation of Single Cells on a Microfluidic Device Integrating Droplet Generation with Fluorescence-Activated Droplet Sorting. *Biomed. Microdevices* **2013**, *15* (3), 553–560.
(109) Qiao, Y.; Zhao, X.; Zhu, J.; Tu, R.; Dong, L.; Wang, L.; Dong, Z.; Wang, Q.; Du, W. Fluorescence-Activated Droplet Sorting of Lipolytic Microorganisms Using a Compact Optical System. *Lab Chip* **2018**, *18* (1), 190–196.
(110) Shembekar, N.; Hu, H.; Eustace, D.; Merten, C. A. Single-Cell Droplet Microfluidic Screening for Antibodies Specifically Binding to Target Cells. *Cell Rep.* **2018**, *22* (8), 2206–2215.

(111) Debs, B. E.; Utharala, R.; Balyasnikova, I. V.; Griffiths, A. D.; Merten, C. A. Functional Single-Cell Hybridoma Screening Using Droplet-Based Microfluidics. *Proc. Natl. Acad. Sci. U. S. A.* **2012**, *109* (29), 11570.
(112) Liu, D.; Sun, M.; Zhang, J.; Hu, R.; Fu, W.; Xuanyuan, T.; Liu, W. Single-Cell Droplet Microfluidics for Biomedical Applications. *Analyst* **2022**, *147* (11), 2294–2316.
(113) Matuła, K.; Rivello, F.; Huck, W. T. S. Single-Cell Analysis Using Droplet Microfluidics. *Adv. Biosys.* **2020**, *4* (1), 1900188.
(114) Kaushik, A. M.; Hsieh, K.; Wang, T.-H. Droplet Microfluidics for High-Sensitivity, High-Throughput Detection and Screening of Disease Biomarkers. *Wiley Interdiscip. Rev.: Nanomed. Nanobiotechnol.* **2019**, *10* (6), e1522.
(115) Perkins, G.; Lu, H.; Garlan, F.; Taly, V. Droplet-Based Digital PCR. In *Advances in Clinical Chemistry*; Elsevier, 2017; Vol. 79, pp 43–91.
(116) Taylor, S. C.; Laperriere, G.; Germain, H. Droplet Digital PCR versus qPCR for Gene Expression Analysis with Low Abundant Targets: From Variable Nonsense to Publication Quality Data. *Sci. Rep.* **2017**, *7* (1), 2409.
(117) Kuypers, J.; Jerome, K. R. Applications of Digital PCR for Clinical Microbiology. *J. Clin. Microbiol.* **2017**, *55* (6), 1621–1628.
(118) Salomon, R.; Kaczorowski, D.; Valdes-Mora, F.; Nordon, R. E.; Neild, A.; Farbehi, N.; Bartonicek, N.; Gallego-Ortega, D. Droplet-Based Single Cell RNAseq Tools: A Practical Guide. *Lab Chip* **2019**, *19* (10), 1706–1727.
(119) Walt, D. R. Optical Methods for Single Molecule Detection and Analysis. *Anal. Chem.* **2013**, *85* (3), 1258–1263.
(120) Payne, E. M.; Holland-Moritz, D. A.; Sun, S.; Kennedy, R. T. High-Throughput Screening by Droplet Microfluidics: Perspective into Key Challenges and Future Prospects. *Lab Chip* **2020**, *20* (13), 2247–2262.
(121) Aharoni, A.; Amitai, G.; Bernath, K.; Magdassi, S.; Tawfik, D. S. High-Throughput Screening of Enzyme Libraries: Thiolactonases Evolved by Fluorescence-Activated Sorting of Single Cells in Emulsion Compartments. *Chem. Biol.* **2005**, *12* (12), 1281–1289.
(122) Ryckelynck, M.; Baudrey, S.; Rick, C.; Marin, A.; Coldren, F.; Westhof, E.; Griffiths, A. D. Using Droplet-Based Microfluidics to Improve the Catalytic Properties of RNA under Multiple-Turnover Conditions. *RNA* **2015**, *21* (3), 458–469.
(123) Kang, D.-K.; Ali, M. M.; Zhang, K.; Huang, S. S.; Peterson, E.; Digman, M. A.; Gratton, E.; Zhao, W. Rapid Detection of Single Bacteria in Unprocessed Blood Using Integrated Comprehensive Droplet Digital Detection. *Nat. Commun.* **2014**, *5* (1), 5427.
(124) Chi, Y.; Shi, M.; Wu, Y.; Wu, Y.; Chang, Y.; Liu, M. Single Bacteria Detection by Droplet DNAzyme-Coupled Rolling Circle Amplification. *Anal. Methods* **2022**, *14* (23), 2244–2248.
(125) Yang, K.; Chaput, J. C. Amplification-Free COVID-19 Detection by Digital Droplet REVEALR. *ACS Synth. Biol.* **2023**, *12* (4), 1331–1338.

(126) Xue, Q.; Yeung, E. S. Differences in the Chemical Reactivity of Individual Molecules of an Enzyme. *Nature* **1995**, *373* (6516), 681–683.
(127) Claessen, V. I.; Engelkamp, H.; Christianen, P. C. M.; Maan, J. C.; Nolte, R. J. M.; Blank, K.; Rowan, A. E. Single-Biomolecule Kinetics: The Art of Studying a Single Enzyme. *Annu. Rev. Anal. Chem.* **2010**, *3* (1), 319–340.
(128) Craig, D.; Arriaga, E. A.; Banks, P.; Zhang, Y.; Renborg, A.; Palcic, M. M.; Dovichi, N. J. Fluorescence-Based Enzymatic Assay by Capillary Electrophoresis Laser-Induced Fluorescence Detection for the Determination of a Few β-Galactosidase Molecules. *Anal. Biochem.* **1995**, *226* (1), 147–153.
(129) Craig, D. B.; Arriaga, E. A.; Wong, J. C. Y.; Lu, H.; Dovichi, N. J. Studies on Single Alkaline Phosphatase Molecules: Reaction Rate and Activation Energy of a Reaction Catalyzed by a Single Molecule and the Effect of Thermal Denaturation - The Death of an Enzyme. *J. Am. Chem. Soc.* **1996**, *118* (22), 5245–5253.
(130) Tan, W.; Yeung, E. S. Monitoring the Reactions of Single Enzyme Molecules and Single Metal Ions. *Anal. Chem.* **1997**, *69* (20), 4242–4248.
(131) Rissin, D. M.; Gorris, H. H.; Walt, D. R. Distinct and Long-Lived Activity States of Single Enzyme Molecules. *J. Am. Chem. Soc.* **2008**, *130* (15), 5349–5353.
(132) Zhang, H.; Nie, S.; Etson, C. M.; Wang, R. M.; Walt, D. R. Oil-Sealed Femtoliter Fiber-Optic Arrays for Single Molecule Analysis. *Lab Chip* **2012**, *12* (12), 2229.
(133) Kan, C. W.; Rivnak, A. J.; Campbell, T. G.; Piech, T.; Rissin, D. M.; Mösl, M.; Peterça, A.; Niederberger, H.-P.; Minnehan, K. A.; Patel, P. P.; Ferrell, E. P.; Meyer, R. E.; Chang, L.; Wilson, D. H.; Fournier, D. R.; Duffy, D. C. Isolation and Detection of Single Molecules on Paramagnetic Beads Using Sequential Fluid Flows in Microfabricated Polymer Array Assemblies. *Lab Chip* **2012**, *12* (5), 977–985.
(134) Rondelez, Y.; Tresset, G.; Tabata, K. V.; Arata, H.; Fujita, H.; Takeuchi, S.; Noji, H. Microfabricated Arrays of Femtoliter Chambers Allow Single Molecule Enzymology. *Nat. Biotechnol.* **2005**, *23* (3), 361–365.
(135) Turunen, P.; Rowan, A. E.; Blank, K. Single-Enzyme Kinetics with Fluorogenic Substrates: Lessons Learnt and Future Directions. *FEBS Lett.* **2014**, *588* (19), 3553–3563.
(136) Funatsu, T.; Harada, Y.; Tokunaga, M.; Saito, K.; Yanagida, T. Imaging of Single Fluorescent Molecules and Individual ATP Turnovers by Single Myosin Molecules in Aqueous Solution. *Nature* **1995**, *374* (6522), 555–559.
(137) Lu, H. P.; Xun, L.; Xie, X. S. Single-Molecule Enzymatic Dynamics. **1998**, *282*.
(138) Ha, T.; Ting, A. Y.; Liang, J.; Caldwell, W. B.; Deniz, A. A.; Chemla, D. S.; Schultz, P. G.; Weiss, S. Single-Molecule Fluorescence Spectroscopy of Enzyme Conformational Dynamics and Cleavage Mechanism. *Proc. Natl. Acad. Sci. U. S. A.* **1999**, *96* (3), 893–898.
(139) Huynh, M.; Sengupta, B. Analysis of Enzyme Conformation Dynamics Using Single-Molecule Förster Resonance Energy Transfer (smFRET). *Biophysica* **2022**, *2* (2), 123–134.

(140) Bui, M. P. N.; Li, C. A.; Han, K. N.; Choo, J.; Lee, E. K.; Seong, G. H. Enzyme Kinetic Measurements Using a Droplet-Based Microfluidic System with a Concentration Gradient. *Anal. Chem.* **2011**, *83* (5), 1603–1608.
(141) Guan, Z.; Zou, Y.; Zhang, M.; Lv, J.; Shen, H.; Yang, P.; Zhang, H.; Zhu, Z.; Yang, C. J. A Highly Parallel Microfluidic Droplet Method Enabling Single-Molecule Counting for Digital Enzyme Detection. *Biomicrofluidics* **2014**, *8* (1).
(142) Arayanarakool, R.; Shui, L.; Kengen, S. W. M.; Van Den Berg, A.; Eijkel, J. C. T. Single-Enzyme Analysis in a Droplet-Based Micro- and Nanofluidic System. *Lab Chip* **2013**, *13* (10), 1955–1962.
(143) Jung, J.; Han, K. Y.; Koh, H. R.; Lee, J.; Choi, Y. M.; Kim, C.; Kim, S. K. Effect of Single-Base Mutation on Activity and Folding of 10-23 Deoxyribozyme Studied by Three-Color Single-Molecule ALEX FRET. *J. Phys. Chem. B* **2012**, *116* (9), 3007–3012.
(144) Quispe-Tintaya, WilberKim, H.-K.; Rasnik, I.; Liu, J.; Ha, T.; Lu, Y. Dissecting Metal Ion-Dependent Folding and Catalysis of a Single DNAzyme. *Nat. Chem. Biol.* **2017**, *12* (3), 763–768.
(145) Zhang, Y.; Ji, Z.; Wang, X.; Cao, Y.; Pan, H. Single–Molecule Study of DNAzyme Reveals Its Intrinsic Conformational Dynamics. *Int. J. Mol. Sci.* **2023**, *24* (2), 1212.
(146) Endo, M.; Takeuchi, Y.; Suzuki, Y.; Emura, T.; Hidaka, K.; Wang, F.; Willner, I.; Sugiyama, H. Single-Molecule Visualization of the Activity of a Zn2+-Dependent DNAzyme. *Angew. Chem., Int. Ed.* **2015**, *54* (36), 10550–10554.
(147) Zhu, L.; Xu, Y.; Ali, I.; Liu, L.; Wu, H.; Lu, Z.; Liu, Q. Solid-State Nanopore Single-Molecule Sensing of DNAzyme Cleavage Reaction Assisted with Nucleic Acid Nanostructure. *ACS Appl. Mater. Interfaces* **2018**, *10* (31), 26555–26565.
(148) Hage, D. S. Immunoassays. *Anal. Chem.* **1999**, *71* (12), 294–304.
(149) Groff, K.; Brown, J.; Clippinger, A. J. Modern Affinity Reagents: Recombinant Antibodies and Aptamers. *Biotechnol. Adv.* **2015**, *33* (8), 1787–1798.
(150) Peng, P.; Liu, C.; Li, Z.; Xue, Z.; Mao, P.; Hu, J.; Xu, F.; Yao, C.; You, M. Emerging ELISA Derived Technologies for in Vitro Diagnostics. *TrAC, Trends Anal. Chem.* **2022**, *152*, 116605.
(151) Roper, M. G.; Guillo, C. New Technologies in Affinity Assays to Explore Biological Communication. *Anal. Bioanal. Chem.* **2009**, *393* (2), 459–465.
(152) Engvall, E.; Perlmann, P. Enzyme-Linked Immunosorbent Assay (ELISA). Quantitative Assay of Immunoglobulin G. *Immunochemistry* **1971**, *8* (9), 871–874.
(153) Alhajj, M.; Zubair, M.; Farhana, A. Enzyme Linked Immunosorbent Assay. In *StatPearls [Internet]*; StatPearls Publishing: Treasure Island, FL, 2023.
(154) *ELISA: Methods and Protocols*; Matson, R. S., Ed.; Methods in Molecular Biology; Springer US: New York, NY, 2023; Vol. 2612.
(155) Zhang, S.; Garcia-D'Angeli, A.; Brennan, J. P.; Huo, Q. Predicting Detection Limits of Enzyme-Linked Immunosorbent Assay (ELISA) and Bioanalytical Techniques in General. *Analyst* **2013**, *139* (2), 439–445.
(156) Ambrosi, A.; Airò, F.; Merkoçi, A. Enhanced Gold Nanoparticle Based ELISA for a Breast Cancer Biomarker. *Anal. Chem.* **2010**, *82* (3), 1151–1156.

(157) Liu, M.; Jia, C.; Huang, Y.; Lou, X.; Yao, S.; Jin, Q.; Zhao, J.; Xiang, J. Highly Sensitive Protein Detection Using Enzyme-Labeled Gold Nanoparticleprobes. *Analyst* **2010**, *135* (2), 327–331.
(158) Jia, C.-P.; Zhong, X.-Q.; Hua, B.; Liu, M.-Y.; Jing, F.-X.; Lou, X.-H.; Yao, S.-H.; Xiang, J.-Q.; Jin, Q.-H.; Zhao, J.-L. Nano-ELISA for Highly Sensitive Protein Detection. *Biosens. Bioelectron.* **2009**, *24* (9), 2836–2841.
(159) Coarsey, C.; Coleman, B.; Kabir, M. A.; Sher, M.; Asghar, W. Development of a Flow-Free Magnetic Actuation Platform for an Automated Microfluidic ELISA. *RSC Adv.* **2019**, *9* (15), 8159–8168.
(160) Cohen, L.; Cui, N.; Cai, Y.; Garden, P. M.; Li, X.; Weitz, D. A.; Walt, D. R. Single Molecule Protein Detection with Attomolar Sensitivity Using Droplet Digital Enzyme-Linked Immunosorbent Assay. *ACS Nano* **2020**, *14* (8), 9491–9501.
(161) Tuerk, C.; Gold, L. Systematic Evolution of Ligands by Exponential Enrichment: RNA Ligands to Bacteriophage T4 DNA Polymerase. *Science* **1990**, *249* (4968), 505–510.
(162) Ellington, A. D.; Szostak, J. W. In Vitro Selection of RNA Molecules That Bind Specific Ligands. *Nature* **1990**, *346* (6287), 818–822.
(163) Aquino-Jarquin, G.; Toscano-Garibay, J. D. RNA Aptamer Evolution: Two Decades of SELEction. *Int. J. Mol. Sci.* **2011**, *12* (12), 9155–9171.
(164) Lakhin, A. V.; Tarantul, V. Z.; Gening, L. V. Aptamers: Problems, Solutions and Prospects. *Acta Naturae* **2013**, *5* (4), 34–43.
(165) Bruno, J. G. In VitroSelection of DNA to Chloroaromatics Using Magnetic Microbead-Based Affinity Separation and Fluorescence Detection. *Biochem. Biophys. Res. Commun.* **1997**, *234* (1), 117–120.
(166) Darmostuk, M.; Rimpelova, S.; Gbelcova, H.; Ruml, T. Current Approaches in SELEX: An Update to Aptamer Selection Technology. *Biotechnol. Adv.* **2015**, *33* (6), 1141–1161.
(167) Wang, J.; Yu, J.; Yang, Q.; McDermott, J.; Scott, A.; Vukovich, M.; Lagrois, R.; Gong, Q.; Greenleaf, W.; Eisenstein, M.; Ferguson, B. S.; Soh, H. T. Multiparameter Particle Display (MPPD): A Quantitative Screening Method for the Discovery of Highly Specific Aptamers. *Angew. Chem., Int. Ed.* **2017**, *56* (3), 744–747.
(168) Nagano, M.; Oguro, T.; Sawada, R.; Yoshitomi, T.; Yoshimoto, K. Accelerated Discovery of Potent Bioactive Anti-TNFα Aptamers by Microbead-Assisted Capillary Electrophoresis (MACE)-SELEX. *ChemBioChem* **2021**, *22* (23), 3341–3347.
(169) Mendonsa, S. D.; Bowser, M. T. In Vitro Evolution of Functional DNA Using Capillary Electrophoresis. *J. Am. Chem. Soc.* **2004**, *126* (1), 20–21.
(170) Mendonsa, S. D.; Bowser, M. T. In Vitro Selection of Aptamers with Affinity for Neuropeptide Y Using Capillary Electrophoresis. *J. Am. Chem. Soc.* **2005**, *127* (26), 9382–9383.
(171) Liu, J.; Mazumdar, D.; Lu, Y. A Simple and Sensitive "Dipstick" Test in Serum Based on Lateral Flow Separation of Aptamer-Linked Nanostructures. *Angew. Chem., Int. Ed.* **2006**, *45* (47), 7955–7959.

(172) Chen, A.; Yang, S. Replacing Antibodies with Aptamers in Lateral Flow Immunoassay. *Biosens. Bioelectron.* **2015**, *71*, 230–242.
(173) Bruno, J. G.; Carrillo, M. P.; Richarte, A. M.; Phillips, T.; Andrews, C.; Lee, J. S. Development, Screening, and Analysis of DNA Aptamer Libraries Potentially Useful for Diagnosis and Passive Immunity of Arboviruses. *BMC Res. Notes* **2012**, *5* (1), 633.
(174) Toh, S. Y.; Citartan, M.; Gopinath, S. C. B.; Tang, T.-H. Aptamers as a Replacement for Antibodies in Enzyme-Linked Immunosorbent Assay. *Biosens. Bioelectron.* **2015**, *64*, 392–403.
(175) Tombelli, S.; Minunni, M.; Mascini, M. Analytical Applications of Aptamers. *Biosens. Bioelectron.* **2005**, *20* (12), 2424–2434.
(176) Zhang, H.; Li, X. F.; Le, X. C. Tunable Aptamer Capillary Electrophoresis and Its Application to Protein Analysis. *J. Am. Chem. Soc.* **2008**, *130* (1), 34–35.
(177) Hamaguchi, N.; Ellington, A.; Stanton, M. Aptamer Beacons for the Direct Detection of Proteins. *Anal. Biochem.* **2001**, *294* (2), 126–131.
(178) Goulko, A. A.; Li, F.; Chris Le, X. Bioanalytical Applications of Aptamer and Molecular-Beacon Probes in Fluorescence-Affinity Assays. *TrAC, Trends Anal. Chem.* **2009**, *28* (7), 878–892.
(179) Deng, B.; Lin, Y.; Wang, C.; Li, F.; Wang, Z.; Zhang, H.; Li, X.-F.; Le, X. C. Aptamer Binding Assays for Proteins: The Thrombin Example—A Review. *Anal. Chim. Acta* **2014**, *837*, 1–15.
(180) Zon, G. Recent Advances in Aptamer Applications for Analytical Biochemistry. *Anal. Biochem.* **2020**, No. June, 113894.
(181) Barrollier, J.; Watzke, E.; Gibian, H. Simple apparatus for support-free preparative filter electrophoresis. *Z. Naturforsch. B.* **1958**, *13B* (11), 754–755.
(182) Hannig, K. Die trägerfreie kontinuierliche Elektrophorese und ihre Anwendung. *Z. Anal. Chem.* **1961**, *181* (1), 244–254.
(183) Raymond, D. E.; Manz, Andreas.; Widmer, H. Michael. Continuous Sample Pretreatment Using a Free-Flow Electrophoresis Device Integrated onto a Silicon Chip. *Anal. Chem.* **1994**, *66* (18), 2858–2865.
(184) Raymond, D. E.; Manz, A.; Widmer, H. M. Continuous Separation of High Molecular Weight Compounds Using a Microliter Volume Free-Flow Electrophoresis Microstructure. *Anal. Chem.* **1996**, *68* (15), 2515–2522.
(185) Turgeon, R. T.; Bowser, M. T. Micro Free-Flow Electrophoresis: Theory and Applications. *Anal. Bioanal. Chem.* **2009**, *394* (1), 187–198.
(186) Johnson, A. C.; Bowser, M. T. Micro Free Flow Electrophoresis. *Lab Chip* **2018**, *18* (1), 27–40.
(187) Fonslow, B. R.; Bowser, M. T. Optimizing Band Width and Resolution in Micro-Free Flow Electrophoresis. *Anal. Chem.* **2006**, *78* (24), 8236–8244.
(188) Geiger, M.; Harstad, R. K.; Bowser, M. T. Effect of Surface Adsorption on Temporal and Spatial Broadening in Micro Free Flow Electrophoresis. *Anal. Chem.* **2015**, *87* (23), 11682–11690.

(189) Anciaux, S. K.; Bowser, M. T. Reduced Surface Adsorption in 3D Printed Acrylonitrile Butadiene Styrene Micro Free-Flow Electrophoresis Devices. *Electrophoresis* **2020**, *41* (3–4), 225–234.
(190) Fonslow, B. R.; Barocas, V. H.; Bowser, M. T. Using Channel Depth to Isolate and Control Flow in a Micro Free-Flow Electrophoresis Device. *Anal. Chem.* **2006**, *78* (15), 5369–5374.
(191) Turgeon, R. T.; Bowser, M. T. Improving Sensitivity in Micro-Free Flow Electrophoresis Using Signal Averaging. *Electrophoresis* **2009**, *30* (8), 1342–1348.
(192) Kohlheyer, D.; Eijkel, J. C. T.; Schlautmann, S.; van den Berg, A.; Schasfoort, R. B. M. Bubble-Free Operation of a Microfluidic Free-Flow Electrophoresis Chip with Integrated Pt Electrodes. *Anal. Chem.* **2008**, *80* (11), 4111–4118.
(193) Zhang, A.; Xu, J.; Li, X.; Lin, Z.; Song, Y.; Li, X.; Wang, Z.; Cheng, Y. High-Throughput Continuous-Flow Separation in a Micro Free-Flow Electrophoresis Glass Chip Based on Laser Microfabrication. *Sensors* **2022**, *22* (3), 1124.
(194) Geiger, M.; Bowser, M. T. Effect of Fluorescent Labels on Peptide and Amino Acid Sample Dimensionality in Two Dimensional nLC × μFFE Separations. *Anal. Chem.* **2016**, *88* (4), 2177–2187.
(195) Johnson, A. C.; Bowser, M. T. High-Speed, Comprehensive, Two Dimensional Separations of Peptides and Small Molecule Biological Amines Using Capillary Electrophoresis Coupled with Micro Free Flow Electrophoresis. *Anal. Chem.* **2017**, *89* (3), 1665–1673.
(196) Novo, P.; Jender, M.; Dell'Aica, M.; Zahedi, R. P.; Janasek, D. Free Flow Electrophoresis Separation of Proteins and DNA Using Microfluidics and Polycarbonate Membranes. *Procedia Eng.* **2016**, *168*, 1382–1385.
(197) Walowski, B.; Hüttner, W.; Wackerbarth, H. Generation of a Miniaturized Free-Flow Electrophoresis Chip Based on a Multi-Lamination Technique—Isoelectric Focusing of Proteins and a Single-Stranded DNA Fragment. *Anal. Bioanal. Chem.* **2011**, *401* (8), 2465–2471.
(198) Shen, Q.-Y.; Guo, C.-G.; Yan, J.; Zhang, Q.; Xie, H.-Y.; Jahan, S.; Fan, L.-Y.; Xiao, H.; Cao, C.-X. Target Protein Separation and Preparation by Free-Flow Electrophoresis Coupled with Charge-to-Mass Ratio Analysis. *J. Chromatogr. A* **2015**, *1397*, 73–80.
(199) Song, Y.-A.; Chan, M.; Celio, C.; Tannenbaum, S. R.; Wishnok, J. S.; Han, J. Free-Flow Zone Electrophoresis of Peptides and Proteins in PDMS Microchip for Narrow pI Range Sample Prefractionation Coupled with Mass Spectrometry. *Anal. Chem.* **2010**, *82* (6), 2317–2325.
(200) Saar, K. L.; Zhang, Y.; Müller, T.; Kumar, C. P.; Devenish, S.; Lynn, A.; Łapińska, U.; Yang, X.; Linse, S.; Knowles, T. P. J. On-Chip Label-Free Protein Analysis with Downstream Electrodes for Direct Removal of Electrolysis Products. *Lab Chip* **2018**, *18* (1), 162–170.
(201) Turgeon, R. T.; Fonslow, B. R.; Jing, M.; Bowser, M. T. Measuring Aptamer Equilibria Using Gradient Micro Free Flow Electrophoresis. *Anal. Chem.* **2010**, *82* (1), 3636–3641.

(202) Jing, M.; Bowser, M. T. Isolation of DNA Aptamers Using Micro Free Flow Electrophoresis. *Lab Chip* **2011**, *11* (21), 3703.
(203) Arter, W. E.; Saar, K. L.; Herling, T. W.; Knowles, T. P. J. Microchip Free-Flow Electrophoresis for Bioanalysis, Sensing, and Purification. In *Biomedical Engineering Technologies: Volume 2*; Rasooly, A., Baker, H., Ossandon, M. R., Eds.; Springer US: New York, NY, 2022; pp 249–266.
(204) Krainer, G.; Saar, K. L.; Arter, W. E.; Welsh, T. J.; Czekalska, M. A.; Jacquat, R. P. B.; Peter, Q.; Traberg, W. C.; Pujari, A.; Jayaram, A. K.; Challa, P.; Taylor, C. G.; Van Der Linden, L.-M.; Franzmann, T.; Owens, R. M.; Alberti, S.; Klenerman, D.; Knowles, T. P. J. Direct Digital Sensing of Protein Biomarkers in Solution. *Nat. Commun.* **2023**, *14* (1), 653.
(205) Lu, H.; Gaudet, S.; Schmidt, M. A.; Jensen, K. F. A Microfabricated Device for Subcellular Organelle Sorting. *Anal. Chem.* **2004**, *76* (19), 5705–5712.
(206) Kostal, V.; Fonslow, B. R.; Arriaga, E. A.; Bowser, M. T. Fast Determination of Mitochondria Electrophoretic Mobility Using Micro Free-Flow Electrophoresis. *Anal. Chem.* **2009**, *81* (22), 9267–9273.
(207) Podszun, S.; Vulto, P.; Heinz, H.; Hakenberg, S.; Hermann, C.; Hankemeier, T.; Urban, G. A. Enrichment of Viable Bacteria in a Micro-Volume by Free-Flow Electrophoresis. *Lab Chip* **2012**, *12* (3), 451–457.
(208) Kohlheyer, D.; Eijkel, J. C. T.; Van Den Berg, A.; Schasfoort, R. B. M. Miniaturizing Free-Flow Electrophoresis – a Critical Review. *Electrophoresis* **2008**, *29* (5), 977–993.
(209) Janasek, D.; Schilling, M.; Manz, A.; Franzke, J. Electrostatic Induction of the Electric Field into Free-Flow Electrophoresis Devices. *Lab Chip* **2006**, *6* (6), 710.
(210) Kohlheyer, D.; Besselink, G. A. J.; Schlautmann, S.; Schasfoort, R. B. M. Free-Flow Zone Electrophoresis and Isoelectric Focusing Using a Microfabricated Glass Device with Ion Permeable Membranes. *Lab Chip* **2006**, *6* (3), 374.
(211) Song, Y.-A.; Hsu, S.; Stevens, A. L.; Han, J. Continuous-Flow pI-Based Sorting of Proteins and Peptides in a Microfluidic Chip Using Diffusion Potential. *Anal. Chem.* **2006**, *78* (11), 3528–3536.
(212) Albrecht, J. W.; El-Ali, J.; Jensen, K. F. Cascaded Free-Flow Isoelectric Focusing for Improved Focusing Speed and Resolution. *Anal. Chem.* **2007**, *79* (24), 9364–9371.
(213) Jezierski, S.; Tehsmer, V.; Nagl, S.; Belder, D. Integrating Continuous Microflow Reactions with Subsequent Micropreparative Separations on a Single Microfluidic Chip. *Chem. Commun.* **2013**, *49* (99), 11644.
(214) Pfeiffer, S. A.; Rudisch, B. M.; Glaeser, P.; Spanka, M.; Nitschke, F.; Robitzki, A. A.; Schneider, C.; Nagl, S.; Belder, D. Continuous Purification of Reaction Products by Micro Free-Flow Electrophoresis Enabled by Large Area Deep-UV Fluorescence Imaging. *Anal. Bioanal. Chem.* **2018**, *410* (3), 853–862.
(215) Rudisch, B. M.; Pfeiffer, S. A.; Geissler, D.; Speckmeier, E.; Robitzki, A. A.; Zeitler, K.; Belder, D. Nonaqueous Micro Free-Flow Electrophoresis for Continuous Separation of Reaction Mixtures in Organic Media. *Anal. Chem.* **2019**, *91* (10), 6689–6694.

(216) Benz, C.; Boomhoff, M.; Appun, J.; Schneider, C.; Belder, D. Chip-Based Free-Flow Electrophoresis with Integrated Nanospray Mass-Spectrometry. *Angew. Chem., Int. Ed.* **2015**, *54* (9), 2766–2770.
(217) Jender, M.; Novo, P.; Maehler, D.; Münchberg, U.; Janasek, D.; Freier, E. Multiplexed Online Monitoring of Microfluidic Free-Flow Electrophoresis via Mass Spectrometry. *Anal. Chem.* **2020**, *92* (9), 6764–6769.
(218) Fonslow, B. R.; Bowser, M. T. Fast Electrophoretic Separation Optimization Using Gradient Micro Free-Flow Electrophoresis. *Anal. Chem.* **2008**, *80* (9), 3182–3189.
(219) Geiger, M.; Frost, N. W.; Bowser, M. T. Comprehensive Multidimensional Separations of Peptides Using Nano-Liquid Chromatography Coupled with Micro Free Flow Electrophoresis. *Anal. Chem.* **2014**, *86* (10), 5136–5142.
(220) Arter, W. E.; Charmet, J.; Kong, J.; Saar, K. L.; Herling, T. W.; Müller, T.; Keyser, U. F.; Knowles, T. P. J. Combining Affinity Selection and Specific Ion Mobility for Microchip Protein Sensing. *Anal. Chem.* **2018**, *90* (17), 10302–10310.
(221) Arter, W. E.; Xu, C. K.; Castellana-Cruz, M.; Herling, T. W.; Krainer, G.; Saar, K. L.; Kumita, J. R.; Dobson, C. M.; Knowles, T. P. J. Rapid Structural, Kinetic, and Immunochemical Analysis of Alpha-Synuclein Oligomers in Solution. *Nano Lett.* **2020**, *20* (11), 8163–8169.
(222) Jezierski, S.; Gitlin, L.; Nagl, S.; Belder, D. Multistep Liquid-Phase Lithography for Fast Prototyping of Microfluidic Free-Flow-Electrophoresis Chips. *Anal. Bioanal. Chem.* **2011**, *401* (8), 2651–2656.
(223) Becker, M.; Marggraf, U.; Janasek, D. Separation of Proteins Using a Novel Two-Depth Miniaturized Free-Flow Electrophoresis Device with Multiple Outlet Fractionation Channels. *J. Chromatogr. A* **2009**, *1216* (47), 8265–8269.
(224) Kohlheyer, D.; Eijkel, J. C. T.; Schlautmann, S.; van den Berg, A.; Schasfoort, R. B. M. Microfluidic High-Resolution Free-Flow Isoelectric Focusing. *Anal. Chem.* **2007**, *79* (21), 8190–8198.
(225) Fonslow, B. R.; Bowser, M. T. Free-Flow Electrophoresis on an Anodic Bonded Glass Microchip. *Anal. Chem.* **2005**, *77* (17), 5706–5710.
(226) Jezierski, S.; Belder, D.; Nagl, S. Microfluidic Free-Flow Electrophoresis Chips with an Integrated Fluorescent Sensor Layer for Real Time pH Imaging in Isoelectric Focusing. *Chem. Commun.* **2013**, *49* (9), 904–906.
(227) Zhang, C.-X.; Manz, A. High-Speed Free-Flow Electrophoresis on Chip. *Anal. Chem.* **2003**, *75* (21), 5759–5766.
(228) Köhler, S.; Weilbeer, C.; Howitz, S.; Becker, H.; Beushausen, V.; Belder, D. PDMS Free-Flow Electrophoresis Chips with Integrated Partitioning Bars for Bubble Segregation. *Lab Chip* **2011**, *11* (2), 309–314.
(229) Saar, K. L.; Müller, T.; Charmet, J.; Challa, P. K.; Knowles, T. P. J. Enhancing the Resolution of Micro Free Flow Electrophoresis through Spatially Controlled Sample Injection. *Anal. Chem.* **2018**, *90* (15), 8998–9005.
(230) Raj M, K.; Chakraborty, S. PDMS Microfluidics: A Mini Review. *J. Appl. Polym. Sci.* **2020**, *137* (27), 48958.
(231) Anciaux, S. K.; Geiger, M.; Bowser, M. T. 3D Printed Micro Free-Flow Electrophoresis Device. *Anal. Chem.* **2016**, *88* (15), 7675–7682.

(232) Preuss, J.; Nguyen, G. N.; Berk, V.; Bahnemann, J. Miniaturized Free-flow Electrophoresis: Production, Optimization, and Application Using 3D Printing Technology. *Electrophoresis* **2021**, *42* (3), 305–314.
(233) Barbaresco, F.; Cocuzza, M.; Pirri, C. F.; Marasso, S. L. Application of a Micro Free-Flow Electrophoresis 3D Printed Lab-on-a-Chip for Micro-Nanoparticles Analysis. *Nanomaterials* **2020**, *10* (7), 1277.
(234) Stone, V. N.; Baldock, S. J.; Croasdell, L. A.; Dillon, L. A.; Fielden, P. R.; Goddard, N. J.; Thomas, C. L. P.; Treves Brown, B. J. Free Flow Isotachophoresis in an Injection Moulded Miniaturised Separation Chamber with Integrated Electrodes. *J. Chromatogr. A* **2007**, *1155* (2), 199–205.
(235) Köhler, S.; Benz, C.; Becker, H.; Beckert, E.; Beushausen, V.; Belder, D. Micro Free-Flow Electrophoresis with Injection Molded Chips. *RSC Adv.* **2012**, *2* (2), 520–525.
(236) Zhou, W.; Xia, L.; Xiao, X.; Li, G.; Pu, Q. A Microchip Device to Enhance Free Flow Electrophoresis Using Controllable Pinched Sample Injections. *Electrophoresis* **2019**, *40* (16–17), 2165–2171.
(237) Mazutis, L.; Gilbert, J.; Ung, W. L.; Weitz, D. A.; Griffiths, A. D.; Heyman, J. A. Single-Cell Analysis and Sorting Using Droplet-Based Microfluidics. *Nat. Protoc.* **2013**, *8* (5), 870–891.
(238) Trypsteen, W.; Vynck, M.; de Neve, J.; Bonczkowski, P.; Kiselinova, M.; Malatinkova, E.; Vervisch, K.; Thas, O.; Vandekerckhove, L.; de Spiegelaere, W. Ddpcrquant: Threshold Determination for Single Channel Droplet Digital PCR Experiments. *Anal. Bioanal. Chem.* **2015**, *407* (19), 5827–5834.
(239) Markham, N. R.; Zuker, M. DINAMelt Web Server for Nucleic Acid Melting Prediction. *Nucleic Acids Res.* **2005**, *33* (Web Server issue), W577-581.
(240) Owczarzy, R.; Tataurov, A. V.; Wu, Y.; Manthey, J. A.; McQuisten, K. A.; Almabrazi, H. G.; Pedersen, K. F.; Lin, Y.; Garretson, J.; McEntaggart, N. O.; Sailor, C. A.; Dawson, R. B.; Peek, A. S. IDT SciTools: A Suite for Analysis and Design of Nucleic Acid Oligomers. *Nucleic Acids Res.* **2008**, *36*, 163–169.
(241) Ven, K.; Safdar, S.; Dillen, A.; Lammertyn, J.; Spasic, D. Re-Engineering 10–23 Core DNA- and MNAzymes for Applications at Standard Room Temperature. *Anal. Bioanal. Chem.* **2019**, *411* (1), 205–215.
(242) Baum, D. A.; Silverman, S. K. Deoxyribozymes: Useful DNA Catalysts in Vitro and in Vivo. *Cell. Mol. Life Sci.* **2008**, *65* (14), 2156–2174.
(243) Khan, S.; Burciu, B.; Filipe, C. D. M.; Li, Y.; Dellinger, K.; Didar, T. F. DNAzyme-Based Biosensors: Immobilization Strategies, Applications, and Future Prospective. *ACS Nano* **2021**, *15* (9), 13943–13969.
(244) Joensson, H. N.; Samuels, M. L.; Bronzes, E. R.; Medkova, M.; Uhlén, M.; Link, D. R.; Andersson-Svahn, H. Detection and Analysis of Low-Abundance Cell-Surface Biomarkers Using Enzymatic Amplification in Microfluidic Droplets. *Angew. Chem., Int. Ed.* **2009**, *48* (14), 2518–2521.
(245) Huebner, A.; Olguin, L. F.; Bratton, D.; Whyte, G.; Huck, W. T. S.; De Mello, A. J.; Edel, J. B.; Abell, C.; Hollfelder, F. Development of Quantitative Cell-Based Enzyme Assays in Microdroplets. *Anal. Chem.* **2008**, *80* (10), 3890–3896.

(246) Hindson, B. J.; Ness, K. D.; Masquelier, D. A.; Belgrader, P.; Heredia, N. J.; Makarewicz, A. J.; Bright, I. J.; Lucero, M. Y.; Hiddessen, A. L.; Legler, T. C.; Kitano, T. K.; Hodel, M. R.; Petersen, J. F.; Wyatt, P. W.; Steenblock, E. R.; Shah, P. H.; Bousse, L. J.; Troup, C. B.; Mellen, J. C.; Wittmann, D. K.; Erndt, N. G.; Cauley, T. H.; Koehler, R. T.; So, A. P.; Dube, S.; Rose, K. A.; Montesclaros, L.; Wang, S.; Stumbo, D. P.; Hodges, S. P.; Romine, S.; Milanovich, F. P.; White, H. E.; Regan, J. F.; Karlin-Neumann, G. A.; Hindson, C. M.; Saxonov, S.; Colston, B. W. High-Throughput Droplet Digital PCR System for Absolute Quantitation of DNA Copy Number. *Anal. Chem.* **2011**, *83* (22), 8604–8610.
(247) Liu, J.; Lu, Y. FRET Study of a Trifluorophore-Labeled DNAzyme. *J. Am. Chem. Soc.* **2002**, *124* (51), 15208–15216.
(248) Suenaga, H.; Liu, R.; Shiramasa, Y.; Kanagawa, T. Novel Approach to Quantitative Detection of Specific rRNA in a Microbial Community, Using Catalytic DNA. *Appl. Environ. Microbiol.* **2005**, *71* (8), 4879–4884.
(249) Todd, A. V.; Fuery, C. J.; Impey, H. L.; Applegate, T. L.; Haughton, M. A. DzyNA-PCR: Use of DNAzymes to Detect and Quantify Nucleic Acid Sequences in a Real-Time Fluorescent Format. *Clin. Chem.* **2000**, *46* (5), 625–630.
(250) Cairns, M. J. Nucleic Acid Mutation Analysis Using Catalytic DNA. *Nucleic Acids Res.* **2000**, *28* (3), 9e–99.
(251) Basu, S.; Sriram, B.; Goila, R.; Banerjea, A. C. Targeted Cleavage of HIV-1 Coreceptor-CXCR-4 by RNA-Cleaving DNA-Enzyme: Inhibition of Coreceptor Function. *Antiviral Res.* **2000**, *46* (2), 125–134.
(252) Santoro, S. W.; Joyce, G. F. Mechanism and Utility of an RNA-Cleaving DNA Enzyme. *Biochemistry* **1998**, *37* (38), 13330–13342.
(253) Rosenbach, H.; Victor, J.; Etzkorn, M.; Steger, G.; Riesner, D.; Span, I. Molecular Features and Metal Ions That Influence 10-23 DNAzyme Activity. *Molecules* **2020**, *25* (13), 3100.
(254) Victor, J.; Steger, G.; Riesner, D. Inability of DNAzymes to Cleave RNA in Vivo Is Due to Limited Mg2+ Concentration in Cells. *Eur. Biophys. J.* **2018**, *47* (4), 333–343.
(255) Kim, D.; Park, H. K.; Choi, H.; Noh, J.; Kim, K.; Jeong, S. Continuous Flow Purification of Nanocrystal Quantum Dots. *Nanoscale* **2014**, *6* (23), 14467–14472.
(256) Zitzmann, F. D.; Jahnke, H.-G.; Pfeiffer, S. A.; Frank, R.; Nitschke, F.; Mauritz, L.; Abel, B.; Belder, D.; Robitzki, A. A. Microfluidic Free-Flow Electrophoresis Based Solvent Exchanger for Continuously Operating Lab-on-Chip Applications. *Anal. Chem.* **2017**, *89* (24), 13550–13558.
(257) Van Midwoud, P. M.; Janse, A.; Merema, M. T.; Groothuis, G. M. M.; Verpoorte, E. Comparison of Biocompatibility and Adsorption Properties of Different Plastics for Advanced Microfluidic Cell and Tissue Culture Models. *Anal. Chem.* **2012**, *84* (9), 3938–3944.
(258) Toepke, M. W.; Beebe, D. J. PDMS Absorption of Small Molecules and Consequences in Microfluidic Applications. *Lab Chip* **2006**, *6* (12), 1484.

(259) LeMon, M. B.; Douma, C. C.; Burke, G. S.; Bowser, M. T. Fabrication of μFFE Devices in COC via Hot Embossing with a 3D-Printed Master Mold. *Micromachines* **2023**, *14* (9), 1728.
(260) Nikolova, D.; Dayss, E.; Leps, G.; Wutzler, A. Surface Modification of Cycloolefinic Copolymers for Optimization of the Adhesion to Metals. *Surf. Interface Anal.* **2004**, *36* (8), 689–693.
(261) Nunes, P. S.; Ohlsson, P. D.; Ordeig, O.; Kutter, J. P. Cyclic Olefin Polymers: Emerging Materials for Lab-on-a-Chip Applications. *Microfluid. Nanofluid.* **2010**, *9* (2–3), 145–161.
(262) Hwang, S.-J.; Tseng, M.-C.; Shu, J.-R.; Her Yu, H. Surface Modification of Cyclic Olefin Copolymer Substrate by Oxygen Plasma Treatment. *Surf. Coat. Technol.* **2008**, *202* (15), 3669–3674.
(263) Roy, S.; Yue, C. Y. Surface Modification of COC Microfluidic Devices: A Comparative Study of Nitrogen Plasma Treatment and Its Advantages over Argon and Oxygen Plasma Treatments. *Plasma Processes Polym.* **2011**, *8* (5), 432–443.
(264) Bhattacharyya, A.; Klapperich, C. M. Mechanical and Chemical Analysis of Plasma and Ultraviolet–Ozone Surface Treatments for Thermal Bonding of Polymeric Microfluidic Devices. *Lab Chip* **2007**, *7* (7), 876–882.
(265) Tsao, C. W.; Hromada, L.; Liu, J.; Kumar, P.; DeVoe, D. L. Low Temperature Bonding of PMMA and COC Microfluidic Substrates Using UV/Ozone Surface Treatment. *Lab Chip* **2007**, *7* (4), 499.
(266) Lin, T.-Y.; Pfeiffer, T. T.; Lillehoj, P. B. Stability of UV/Ozone-Treated Thermoplastics under Different Storage Conditions for Microfluidic Analytical Devices. *RSC Adv.* **2017**, *7* (59), 37374–37379.
(267) Stachowiak, T. B.; Mair, D. A.; Holden, T. G.; Lee, L. J.; Svec, F.; Fréchet, J. M. J. Hydrophilic Surface Modification of Cyclic Olefin Copolymer Microfluidic Chips Using Sequential Photografting. *J. Sep. Sci.* **2007**, *30* (7), 1088–1093.
(268) Roy, S.; Das, T.; Yue, C. Y. High Performance of Cyclic Olefin Copolymer-Based Capillary Electrophoretic Chips. *ACS Appl. Mater. Interfaces* **2013**, *5* (12), 5683–5689.
(269) Jena, R. K.; Yue, C. Y. Cyclic Olefin Copolymer Based Microfluidic Devices for Biochip Applications: Ultraviolet Surface Grafting Using 2-Methacryloyloxyethyl Phosphorylcholine. *Biomicrofluidics* **2012**, *6* (1), 012822.
(270) Klatt, J.-N.; Hutzenlaub, T.; Subkowski, T.; Müller, T.; Hennig, S.; Zengerle, R.; Paust, N. Blocking Protein Adsorption in Microfluidic Chips by a Hydrophobin Coating. *ACS Appl. Polym. Mater.* **2021**, *3* (7), 3278–3286.
(271) Zhang, J.; Das, C.; Fan, H. Z. Dynamic Coating for Protein Separation in Cyclic Olefin Copolymer Microfluidic Devices. *Microfluid. Nanofluid.* **2008**, *5* (3), 327–335.
(272) Edelstein, A. D.; Tsuchida, M. A.; Amodaj, N.; Pinkard, H.; Vale, R. D.; Stuurman, N. Advanced Methods of Microscope Control Using μManager Software. *J. Biol. Methods* **2014**, *1* (2), e10.
(273) Schneider, C. A.; Rasband, W. S.; Eliceiri, K. W. NIH Image to ImageJ: 25 Years of Image Analysis. *Nat. Methods* **2012**, *9* (7), 671–675.

(274) Frost, N. W.; Bowser, M. T. Using Buffer Additives to Improve Analyte Stream Stability in Micro Free Flow Electrophoresis. *Lab Chip* **2010**, *10* (10), 1231–1236.
(275) Iki, N.; Yeung, E. S. Non-Bonded Poly(Ethylene Oxide) Polymer-Coated Column for Protein Separation by Capillary Electrophoresis. *J. Chromatogr. A* **1996**, *731* (1–2), 273–282.
(276) Darwish, I. A. Immunoassay Methods and Their Applications in Pharmaceutical Analysis: Basic Methodology and Recent Advances. *Int. J. Biomed. Sci.* **2006**, *2* (3), 217–235.
(277) *Handbook of Immunoassay Technologies: Approaches, Performances, and Applications*; Vashist, S. K., Luong, J., Eds.; Elsevier/AP, Academic Press, an imprint of Elsevier: London, 2018.
(278) Aydin, S. A Short History, Principles, and Types of ELISA, and Our Laboratory Experience with Peptide/Protein Analyses Using ELISA. *Peptides* **2015**, *72*, 4–15.
(279) Koczula, K. M.; Gallotta, A. Lateral Flow Assays. *Essays Biochem.* **2016**, *60* (1), 111–120.
(280) Landry, J. P.; Ke, Y.; Yu, G.-L.; Zhu, X. D. Measuring Affinity Constants of 1450 Monoclonal Antibodies to Peptide Targets with a Microarray-Based Label-Free Assay Platform. *J. Immunol. Methods* **2015**, *417*, 86–96.
(281) Smith, R. A.; Baglioni, C. The Active Form of Tumor Necrosis Factor Is a Trimer. *J. Biol. Chem.* **1987**, *262* (15), 6951–6954.
(282) Eck, M. J.; Sprang, S. R. The Structure of Tumor Necrosis Factor-α at 2.6 Å Resolution. *J. Biol. Chem.* **1989**, *264* (29), 17595–17605.
(283) Jang, D.; Lee, A.-H.; Shin, H.-Y.; Song, H.-R.; Park, J.-H.; Kang, T.-B.; Lee, S.-R.; Yang, S.-H. The Role of Tumor Necrosis Factor Alpha (TNF-α) in Autoimmune Disease and Current TNF-α Inhibitors in Therapeutics. *Int. J. Mol. Sci.* **2021**, *22* (5), 2719.
(284) Elliott, M. J.; Maini, R. N.; Feldmann, M.; Kalden, J. R.; Antoni, C.; Smolen, J. S.; Leeb, B.; Breedveld, F. C.; Macfarlane, J. D.; Bijl, J. A.; Woody, J. N. Randomised Double-Blind Comparison of Chimeric Monoclonal Antibody to Tumour Necrosis Factor α (cA2) versus Placebo in Rheumatoid Arthritis. *Lancet* **1994**, *344* (8930), 1105–1110.
(285) Weinblatt, M. E.; Keystone, E. C.; Furst, D. E.; Moreland, L. W.; Weisman, M. H.; Birbara, C. A.; Teoh, L. A.; Fischkoff, S. A.; Chartash, E. K. Adalimumab, a Fully Human Anti–Tumor Necrosis Factor α Monoclonal Antibody, for the Treatment of Rheumatoid Arthritis in Patients Taking Concomitant Methotrexate: The ARMADA Trial. *Arthritis Rheum.* **2003**, *48* (1), 35–45.
(286) Hanauer, S. B.; Sandborn, W. J.; Rutgeerts, P.; Fedorak, R. N.; Lukas, M.; MacIntosh, D.; Panaccione, R.; Wolf, D.; Pollack, P. Human Anti–Tumor Necrosis Factor Monoclonal Antibody (Adalimumab) in Crohn's Disease: The CLASSIC-I Trial. *Gastroenterology* **2006**, *130* (2), 323–333.
(287) van Schie, K. A.; Ooijevaar-de Heer, P.; Dijk, L.; Kruithof, S.; Wolbink, G.; Rispens, T. Therapeutic TNF Inhibitors Can Differentially Stabilize Trimeric TNF by Inhibiting Monomer Exchange. *Sci. Rep.* **2016**, *6* (1), 32747.

(288) Daub, H.; Traxler, L.; Ismajli, F.; Groitl, B.; Itzen, A.; Rant, U. The Trimer to Monomer Transition of Tumor Necrosis Factor-Alpha Is a Dynamic Process That Is Significantly Altered by Therapeutic Antibodies. *Sci. Rep.* **2020**, *10* (1), 1–10.
(289) Orava, E. W.; Jarvik, N.; Shek, Y. L.; Sidhu, S. S.; Gariépy, J. A Short DNA Aptamer That Recognizes TNFα and Blocks Its Activity in Vitro. *ACS Chem. Biol.* **2013**, *8* (1), 170–178.
(290) Lai, W. Y.; Wang, J. W.; Huang, B. T.; Lin, E. P. Y.; Yang, P. C. A Novel TNF-α-Targeting Aptamer for TNF-α-Mediated Acute Lung Injury and Acute Liver Failure. *Theranostics* **2019**, *9* (6), 1741–1751.
(291) Kim, J.; Noh, S.; Park, J. A.; Park, S. C.; Park, S. J.; Lee, J. H.; Ahn, J. H.; Lee, T. Recent Advances in Aptasensor for Cytokine Detection: A Review. *Sensors* **2021**, *21* (24).
(292) Parameswaran, N.; Patial, S. Tumor Necrosis Factor-α Signaling in Macrophages. *Crit. Rev. Eukaryotic Gene Expression* **2010**, *20* (2), 87–103.
(293) De Waal Malefyt, R.; Abrams, J.; Bennett, B.; Figdor, C. G.; De Vries, J. E. Interleukin 10(IL-10) Inhibits Cytokine Synthesis by Human Monocytes: An Autoregulatory Role of IL-10 Produced by Monocytes. *J. Exp. Med.* **1991**, *174* (5), 1209–1220.
(294) Shi, L.; Kishore, R.; McMullen, M. R.; Nagy, L. E. Lipopolysaccharide Stimulation of ERK1/2 Increases TNF-α Production via Egr-1. *Am. J. Physiol.* **2002**, *282* (6), C1205–C1211.
(295) Reis, J.; Guan, X. Q.; Kisselev, A. F.; Papasian, C. J.; Qureshi, A. A.; Morrison, D. C.; Van Way, C. W.; Vogel, S. N.; Qureshi, N. LPS-Induced Formation of Immunoproteasomes: TNF-α and Nitric Oxide Production Are Regulated by Altered Composition of Proteasome-Active Sites. *Cell Biochem. Biophys.* **2011**, *60* (1–2), 77–88.
(296) Shurety, W.; Pagan, J. K.; Prins, J. B.; Stow, J. L. Endocytosis of Uncleaved Tumor Necrosis Factor-α in Macrophages. *Lab. Invest.* **2001**, *81* (1), 107–117.
(297) Bochman, M. L.; Paeschke, K.; Zakian, V. A. DNA Secondary Structures: Stability and Function of G-Quadruplex Structures. *Nat. Rev. Genet.* **2012**, *13* (11), 770–780.
(298) Seidel, C. A. M.; Schulz, A.; Sauer, M. H. M. Nucleobase-Specific Quenching of Fluorescent Dyes. 1. Nucleobase One-Electron Redox Potentials and Their Correlation with Static and Dynamic Quenching Efficiencies. *J. Phys. Chem.* **1996**, *100* (13), 5541–5553.
(299) Torimura, M.; Kurata, S.; Yamada, K.; Yokomaku, T.; Kamagata, Y.; Kanagawa, T.; Kurane, R. Fluorescence-Quenching Phenomenon by Photoinduced Electron Transfer between a Fluorescent Dye and a Nucleotide Base. *Anal. Sci.* **2001**, *17* (1), 155–160.
(300) Beckers, J. L.; Boček, P. Sample Stacking in Capillary Zone Electrophoresis: Principles, Advantages and Limitations. *Electrophoresis* **2000**, *21* (14), 2747–2767.
(301) Gebauer, P.; Boček, P. Electrophoretic Sample Stacking. *Electrophoresis* **2009**, *30* (S1), S27–S33.

(302) Liu, J.; Tian, L.; Qiao, Y.; Zhou, S.; Patil, A. J.; Wang, K.; Li, M.; Mann, S. Hydrogel-Immobilized Coacervate Droplets as Modular Microreactor Assemblies. *Angew. Chem., Int. Ed.* **2020**, *59* (17), 6853–6859.
(303) Bhattacharyya, D.; Arachchilage, G. M.; Basu, S. Metal Cations in G-Quadruplex Folding and Stability. *Front. Chem.* **2016**, *4* (SEP), 1–14.